Department of Physics and Astronomy

Heidelberg University

Master thesis

in Physics

submitted by

Maja Rüth

born in Mainz

2023

Constructing a Miniaturized Chemiluminescence Ozone Monitor for Drone-Based Measurements in Volcanic Plumes: A Way to Resolve the Volcanic Ozone Enigma

This Master thesis has been carried out by Maja Rüth

at the

Institute for Environmental Physics

under the supervision of

Prof. Ulrich Platt

Konstruktion eines miniaturisierten Chemilumineszenz-Ozonmessgeräts für drohnenbasierte Messungen in Vulkanfahnen: Ein Weg zur Lösung des vulkanischen Ozon-Rätsels

Vulkanfahnen enthalten reaktive Halogenspezies, insbesondere Brommonoxid (BrO), das den Abbau von Ozon (O_3) katalysiert. Daher wird eine lokale O_3-Abnahme in Vulkanfahnen häufig angenommen und wurde auch in unterschiedlichem Ausmaß an verschiedenen Vulkanen gemessen. Eine Berechnung, die die atmosphärische Durchmischung mit der Geschwindigkeit des O_3-Abbaus in der Fahne vergleicht, deutet jedoch darauf hin, dass es keine signifikante O_3-Abnahme ($\sim$1%) durch reaktives Brom in der Fahne gibt. Bisher wurde O_3 in Vulkanfahnen nur unzureichend bestimmt, da üblicherweise verwendete Ultraviolett (UV) Absorptions-O_3-Messgeräte Interferenzen mit Schwefeldioxid (SO_2), einem häufigen vorhandenem vulkanischen Gas, zeigen. Dieses Problem kann durch die Verwendung eines Chemilumineszenz (CL) O_3-Messgeräts, das keine bekannten Interferenzen mit Spurengasen aus Vulkanfahnen aufweist, überwunden werden. Allerdings sind Feldmessungen mit früheren CL O_3-Messgeräten herausfordernd, da sie schwer und sperrig sind. Hier berichten wir über eine leichte Version eines solchen Instruments (1,5 kg, Schuhkartongröße), die auf eine handelsübliche Drohne montiert werden kann. Insbesondere werden Design, Konstruktion und Charakterisierung des CL O_3-Messgeräts in dieser Arbeit vorgestellt. Messungen im Feld wurden durchgeführt, einschließlich Umgebungsmessungen in Heidelberg und Drohnenmessungen, bei denen ein vertikales O_3-Profil gemessen wurde. Hauptfokus der Feldstudien sind die drohnenbasierten O_3-Messungen in der Vulkanfahne des Ätna. Mit den gleichzeitigen SO_2 Messungen ist eine Antikorrelation sichtbar. Es wurde eine O_3-Abnahme von bis zu $\sim$60% in der Vulkanfahne des Ätna bestimmt. Dies wirft die Frage auf, welcher Prozess zu dieser nun eindeutig beobachteten O_3-Abnahme führt.

Constructing a Miniaturized Chemiluminescence Ozone Monitor for Drone-Based Measurements in Volcanic Plumes: A Way to Resolve the Volcanic Ozone Enigma

Volcanic plumes contain reactive halogen species, especially bromine monoxide (BrO), which catalyses ozone (O_3) destruction. Therefore, local O_3 depletion is commonly assumed inside volcanic plumes and has also been measured to varying degrees at different volcanoes. However, a calculation comparing atmospheric mixing with the rate of O_3 destruction inside the plume suggests no significant reactive halogen catalysed O_3-loss (1% or less) in the plume. So far, O_3 and its distribution in volcanic plumes have only been insufficiently determined since commonly used ultraviolet (UV) absorption O_3 monitors show interference with sulphur dioxide (SO_2), an abundant volcanic gas. This issue can be overcome by using a chemiluminescence (CL) O_3 monitor, which has no known interference from trace gases abundant in volcanic plumes. However, field measurements with former CL O_3 monitors are challenging, as they are heavy and bulky. Here we report on a lightweight version of the instrument (1.5 kg, shoebox size), which can be mounted onto a drone. In particular, the design, construction and characterisation are presented in this thesis. Measurements in the field were performed, including ambient measurements in Heidelberg and drone measurements during which a vertical O_3 profile was measured. Main focus of the measurements are the drone based O_3 measurements in the plume of Etna. With the simultaneous SO_2 measurement, an anti-correlation in the data can be observed, suggesting an O_3 depletion of up to $\sim$60% in the volcanic plume of Etna. This raises the question which process leads to this observed O_3 depletion.

Contents

1. Introduction

1.1. Volcanic gases and ozone

Volcanoes play a crucial role in our Earth system. Large explosive eruptions are known to have a significant impact on their immediate surroundings and can cause natural catastrophes through gas emission, pyroclastic flows, and lava flows (Schmincke, 2013). But also earthquake activity, landslides or mud flows are often related to volcanic activity and in particular to large scale eruptions (e.g. eruption of Mount St. Helens in 1980).

Additionally to these impacts, large eruptions can also cause significant climatic and chemical perturbations within the atmosphere. These effects are not limited to the troposphere but can also extend to the stratosphere. For instance, large amounts of ash and sulphur compounds are emitted into the stratosphere by strong eruptions and can influence the global aerosol layer at about 20 km altitude, called the Junge layer (von Glasow et al., 2009; Jourdain et al., 2016). There the sulphur compounds are converted into aerosols with residence times of 1-2 years and influence climate both, directly through perturbations of Earth energy balance and indirectly via coupling between radiation, microphysics and atmospheric chemistry (Jourdain et al., 2016; Kleinschmitt et al., 2018). This can cause significant climatic changes like surface temperature anomalies (Robock, 2000).

However, also quiescently degassing volcanoes and smaller eruptions are now known to have a significant impact on the atmosphere (von Glasow et al., 2009; von Glasow, 2010; Platt and Bobrowski, 2015). Carn et al. (2017) found that globally about an order of magnitude more gases are emitted by quiescent degassing from volcanoes than by emission during large volcanic eruptions. The primary volcanic emissions, mainly consisting of water vapour, carbon dioxide (CO_2), sulphur species (in particular sulfur dioxide (SO_2) and hydrogen sulfide (H_2S)) as well as hydrogen halides (in particular HCl, HF, HBr and probably also HI), are mixed with the surrounding atmosphere directly after their emission, and form a very unusual atmospheric composition (Kuhn et al., 2022). This particular mixture leads to still not fully understood chemical mechanisms.

For instance, solid and liquid particles are abundant, providing a large surface area for heterogeneous chemical reactions (reactions of gas molecules with reactants in the solid or liquid phase (Roedel and Wagner, 2017)). Also, large amounts of acids form inside the condensing atmospheric vapour from the emitted species HCl, HF and SO_2, leading to acidic rain and fog, this process is often referred to as wet deposition (Delmelle, 2003). This accounts for the high acidity measured in close proximity to volcanoes (Bobrowski et al., 2007), at Etna pH values of rainwater as low as 2 have been found (Calabrese et al., 2011).

Additionally, reactive halogen species (atomic halogens and their oxidants, such as Cl/Br, ClO/BrO, OClO etc.), in particular bromine monoxide (BrO), have been measured in tropospheric volcanic plumes (Bobrowski et al., 2003, 2007; Kern et al., 2009; von Glasow, 2010; Glіß et al., 2015; General et al., 2015). These are, however, not believed to be primary emissions but assumed to be formed from the hydrogen halide HBr through chemical processes of magmatic gases with atmospheric components when light is present. The transformation from HBr into reactive BrO is commonly explained via the so called autocatalytic bromine explosion (Bobrowski et al., 2007; Kern et al., 2009; Jourdain et al., 2016), a reaction mechanism leading to exponential growth of the BrO concentration.

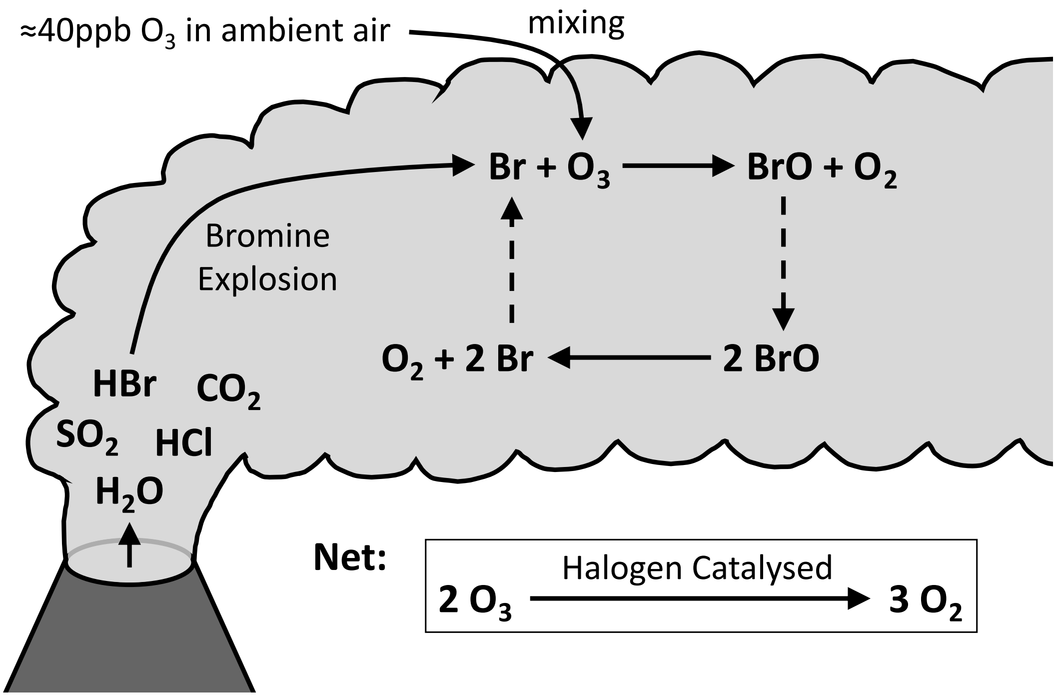

Figure 1: Schematic of the bromine reaction cycle in volcanic plume. From the emitted hydrogen halide HBr atomic bromine Br is produced, which can then react with O_3 to form BrO. BrO is the recycled to Br via its self-reaction. A more detail description can be found in Sec. 2. Figure taken from Bräutigam (2022).

During this reaction mechanism ozone (O_3) is destroyed (see Fig. 1 and Sec. 2 for more details). As a consequence there should be bromine catalysed O_3 destruction leading to a local O_3 depletion within the plume. This reaction cycle is only possible when O_3 is available, showing that O_3 is a key component in the chemical processes within volcanic plumes.

In order to verify this process, several field studies have been conducted to measure O_3 levels within volcanic plumes. A comprehensive list of the reported O_3 depletions measured at a variety of different volcanoes can be found in Surl et al. (2015), Rüth (2021) and Bräutigam (2022). While some studies show no O_3 depletion (see e.g. Roberts, 2018, at Kīlauea), other studies found O_3 depletions of up to 90% loss compared to ambient values (see e.g. Hobbs et al., 1982, at Mount St. Helens).
This already shows that the reported O_3 depletion varies greatly between different volcanoes and field studies. However, different measurement techniques have been used, with not all of them being suitable for measurements in volcanic plumes (more details in Sec. 3.1). Commonly used O_3 monitors, such as short-path ultraviolet (UV) absorption O_3 monitors, do not produce reliable results within volcanic plumes. Either special precautions must be taken when using this type of instrument or completely different measurement techniques must be used to reliably determine O_3 levels.
Additionally, the available data on O_3 depletion is too limited to draw meaningful conclusions or attribute a characteristic O_3 depletion to a specific volcano. This lack of measurements is again an expression of the fact that reliable measurements of O_3 in volcanic plumes are difficult. For most volcanoes only a single field study to measure O_3 in the plume has been conducted, even though O_3 plays a crucial role in volcanic plume chemistry. O_3 measurements can contribute significantly to a better understanding of

plume chemistry. Measuring volcanic O_3 might provide further insights into the formation of BrO from HBr, for instance it is still an unanswered question to which extend its formation might be limited by the availability of O_3. This shows that more, and most importantly, reliable measurements of O_3 in volcanic plumes are needed.

A good way to overcome the interference problem that UV O_3 monitors exhibit without introducing further potential uncertainties is to use an O_3 monitor relying on chemiluminescence (CL). This method was the standard technique in the 1970s and 1980s and recent laboratory experiments as well as field measurements have not found any inferences from trace gases abundant in volcanic plumes (Bobrowski et al., 2020; Rüth, 2021). CL O_3 monitors are therefore a promising alternative to the conventional UV absorption instruments for studies of O_3 in volcanic plumes. However, only few studies in volcanic plumes using CL monitors have been conducted (Hobbs et al., 1982; Vance et al., 2010; Carn et al., 2011), as CL monitors are usually heavy and bulky and therefore make field measurements even more difficult as their use generally entails high infrastructural effort such as airborne measurements.
The purpose of this thesis is therefore to build a lightweight CL O_3 monitor to be used for the measurement in volcanic plumes.

1.2. Preliminary work

Preceding this thesis other studies on CL O_3 monitors were carried out.
In a smog chamber simulating volcanic plumes a CL O_3 monitor was first tested and did not show any interference with the gases present (Bobrowski et al., 2020). This finding gave rise to the idea to further improve existing CL O_3 monitors to enable reliable O_3 in volcanic plumes while keeping infrastructural effort within limits. Rüth (2021) characterised a custom-build CL O_3 monitor provided by MLW Messtechnik für Luft- und Wassereinhaltung which was based on some components of a Bendix CL O_3 monitor model 8002. An in depth description of the adapted monitor can be found in Rüth (2021) and the operation manual "Bedienungsanleitung in Kurzform; Immissions Ozonmonitor für Messungen in Vulkan Rauchfahnen (Prototyp 1)" (Aletter, 2020).
With this prototype, modifications to reduce weight and a digital data logger were realized. The monitor was successfully tested during a first ground based measurement close to a fumarole at Mt. Etna in 2020, where also no cross sensitivities to SO_2 and other volcanic gases were identified. Due to the monitors weight only ground based measurements were possible, limiting the measurement opportunities significantly.

Bräutigam (2022) then started the construction of a new lightweight CL monitor, relying on the same principle, but using updated electronics and a modern photomultiplier tube (PMT). The main components of the new monitor were assembled (reaction chamber and PMT, ethylene supply with pump, electronics and data logging), enabling first laboratory test measurements.

This thesis is a continuation of the work by Bräutigam (2022), in particular completing the construction of the monitor - VOLCANO$_3$ (**V**olcanic **O**zone **L**ogging **C**hemiluminescence **A**nalyser with **N**ew **O**ptimised Technology, **3**rd generation) - (see Sec. 4) and its characterisation (see Sec. 5). Due to its lightweight design, the monitor can be mounted onto a drone enabling flexible airborne O_3 measurements. The monitor is tested in the field, by measuring a vertical O_3 profile (see Sec. 7) and O_3 profiles in the plume of Etna (see Sec. 8).

2. Ozone and volcanic plume chemistry

In this section the reaction mechanism which is believed to be responsible for a local O_3 depletion inside the plume, the so called ‘bromine explosion’, is presented.

Both from a volcanological and from an atmospheric standpoint the amount of volcanic emissions as well as the composition of the emitted gases are of interest, as volcanic emissions on the one hand enable insights into the magmatic system and on the other hand strongly influence atmospheric chemistry.
Here, mainly the impact on the atmosphere and in particular plume chemistry involving O_3 depletion is described, a more extensive description of plume chemistry can be found in the literature, for a comprehensive overview see e.g. von Glasow et al. (2009); von Glasow (2010); Platt and Bobrowski (2015).

Primary volcanic emissions comprise mainly the following species (in the order of descending abundance): water vapour, CO_2, SO_2, H_2S, HCl, HF, H_2, CO and HBr (Schmincke, 2013; Textor et al., 2004; von Glasow et al., 2009). However, when volcanic plume gases are sampled also other gas compounds can be measured, such as reactive halogen species, mainly BrO (Bobrowski et al., 2003), as well as ClO, OClO and IO, though these three species less reliably (Bobrowski and Platt, 2007; Glifß et al., 2015; Schönhardt et al., 2017). It is assumed that these are not primary products and therefore not abundant in the initial plume. They are rather the product of chemical processes of magmatic gases with atmospheric components occurring when ambient air is mixed into the plume (Bobrowski et al., 2007; Kern et al., 2009; Jourdain et al., 2016; Kuhn et al., 2022). The mixing of volcanic gases with ambient air leads to rapidly changing conditions from reducing to oxidising conditions and leads to the very unusual chemistry inside the volcanic plume, and in particular the mentioned reactive halogen chemistry. These reaction mechanisms are important to look at, as halogens can change the budget of O_3 and other oxidants in the atmosphere, and thus might lead to depleted O_3 levels inside the plume. In particular the conversion of HBr into the reactive bromine species BrO, Br and Br_2 is of interest, even when HBr emissions are usually weaker compared to those of HCl. However, the chemistry involving chlorine is less relevant when considering O_3 depletion in volcanic plumes (von Glasow et al., 2009; Surl et al., 2015). The reaction mechanism which is commonly believed to convert HBr into reactive bromine species is shown in the following, (Bobrowski et al., 2007; von Glasow et al., 2009; von Glasow, 2010; Kern et al., 2009, and references therein),

$$
\begin{aligned}
\mathrm{HBr_{(gas)}} &\longrightarrow \mathrm{Br-_{(aq)} + H_{(aq)}}^{+} && (1)\\
\mathrm{HOBr_{(gas)}} &\longrightarrow \mathrm{HOBr_{(aq)}} && (2)\\
\mathrm{HOBr_{(gas)} + Br^{-}_{(aq)} + H_{(aq)}}^{+} &\longrightarrow \mathrm{Br_{2(gas)} + H_2O_{(gas)}} && (3)\\
\mathrm{Br_2} + h\,\nu &\longrightarrow 2\,\mathrm{Br} && (4)\\
\mathrm{Br + O_3} &\longrightarrow \mathrm{BrO + O_2} && (5)\\
\mathrm{BrO + BrO} &\longrightarrow 2\,\mathrm{Br + O_2} && (6)\\
\mathrm{BrO + BrO} &\longrightarrow \mathrm{Br_2 + O_2} && (7)\\
\mathrm{BrO + HO_2} &\longrightarrow \mathrm{HOBr + O_2} && (8)\\
\mathrm{BrO} + h\,\nu &\longrightarrow \mathrm{Br + O} && (9)\\
\textbf{net reaction:} & &&\\
\mathrm{BrO_{(gas)} + O_3 + Br^{-}_{(aq)} + H_{(aq)}}^{+} &\longrightarrow 2\,\mathrm{BrO_{(gas)}} + \text{products} && (10)
\end{aligned}
$$

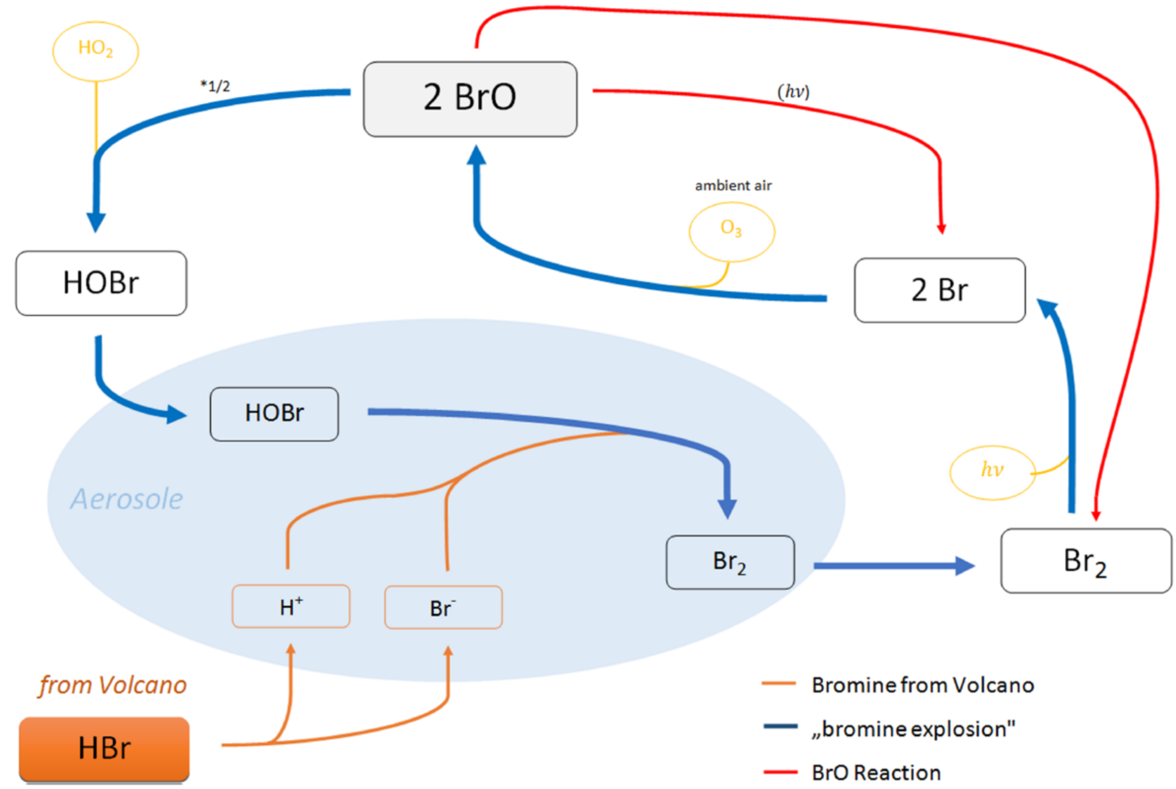

Figure 2: Schematic of the ‘bromine explosion’ inside the volcanic plume. Figure taken from Warnach (2022).

Immediately after the gas release, high temperature oxidative dissociation occurs trough which atomic halogen species (Cl, Br) are produced (Bobrowski et al., 2007; Jourdain et al., 2016; Kuhn et al., 2022). These then react with O_3, available from further entrainment of ambient air into the plume (Reac. 5). BrO can react with HO_2 to form HOBr (Reac. 8). This is a critical step since HOBr can then react with Br^- and H^+ in a heterogeneous reaction within volcanic (sulfate) aerosols to form Br_2 which is quickly released from the condensed into the gas phase. Br^- and H^+ are available from dissolved volcanic HBr. The produced gaseous Br_2 is rapidly photolysed to produce two Br atoms, which can then again react with O_3 to form BrO. With this step the reaction cycle is closed and can start again leading to an exponential growth of BrO since with every reaction cycle the available BrO is doubled. The reaction cycle is therefore commonly called ‘bromine explosion’ (Barrie and Platt, 1997). From the net reaction, Reac. 10, it can also be seen that with each reaction cycle O_3 is destroyed, leading to the assumption that O_3 should be depleted within volcanic plumes.
Crucial for the ‘bromine explosion’ to occur is that solar radiation is available so that Br_2 can be photolysed to give Br (see Reac. 4). This is underlined by the finding of Kern et al. (2009) who did not detect BrO in a volcanic plume during night time. As mentioned above, also the entrainment of ambient air, in particular the availability of O_3 and HO_2 is required. Only then the formation of Br from HBr via reactions Reac. 1, Reac. 3, Reac. 4 is possible. Additionally, acidic particles support Reac. 3, which are usually available in abundance in volcanic plumes.

This autocatalytic reaction mechanism was first observed during spring in the polar boundary layer (Barrie and Platt, 1997; Wennberg, 1999). When BrO was first measured in volcanic plumes (Bobrowski et al., 2003) this reaction mechanism was believed to be responsible for elevated BrO levels and O_3 depletion within volcanic plumes (due to Reaction 5).

The key steps in the O_3 destruction are the reactions Reac. 5 - 7 (see e.g. von Glasow, 2010). In model studies von Glasow (2010) found the self reactions of BrO to be mainly responsible for the destruction of O_3. About 84% of the observed O_3 destruction in the first hour and 90% in the first six hours could be attributed to the BrO self reaction.

When looking at the lifetime of Br and BrO in those reactions it can be seen that for O_3 mixing ratios exceeding 1 ppb the lifetime of Br is shorter than the lifetime of BrO (for details see Rüth (2021)). Therefore, the self reaction of BrO is the rate-determining step and the O_3 depletion is limited by the recycling of Br atoms via the BrO self reaction. This allows the destruction of O_3 to be approximated by the BrO self reaction and thereby by the measured BrO concentrations,

$$\frac{d[\mathrm{O_3}]}{dt} = k_{\mathrm{O_3+Br}} \cdot [\mathrm{O_3}] \cdot [\mathrm{Br}] \approx 2 \cdot k_{\mathrm{BrO+BrO}} \cdot [\mathrm{BrO}]^2, \tag{11}$$

where $k_{\mathrm{O_3+Br}}$ is the reaction constant of Reac. 5, $k_{\mathrm{BrO+BrO}} \approx 2.7 \times 10^{-12}\,\mathrm{cm^3 molec^{-1} s^{-1}}$ the reaction constant of Reac. 6. The factor two is needed since the self reaction of BrO produces two Br atoms, which in turn can react with two O_3 molecules.

As previously shown in Rüth (2021) and Bräutigam (2022), a rough calculation suggests that an O_3 depletion of 1% or less compared to ambient levels should be expected in volcanic plumes. This raises the question whether there actually is an O_3 depletion in volcanic plumes. If there is an O_3 depletion, the calculation suggests that the commonly made assumptions have to be modified or other chemical reactions might be responsible for the O_3 depletion.
A revised version of the calculation trying to explain the observed O_3 depletion during the field measurements at Etna (Sec. 8.3), can be found in Sec. 9. There we look into the needed alterations in the assumptions to explain an O_3 depletion. In this calculation additional chemical reaction cycles, mainly including further halogens, are explored.

3. Ozone measurement techniques

3.1. Overview and problems in volcanic plumes

Numerous measurement methods exist for O_3, including CL, ultraviolet (UV) absorption, and electrochemical monitors. In this section, in particular UV absorption O_3 monitors, their operation principle and their problems in volcanic plumes are showcased.

UV absorption monitors are presumably the most commonly used O_3 monitors today. The majority of the referenced articles monitoring the O_3 mixing ratios at volcanoes (see Sec. 1.1) report the use of an UV absorption instruments.
UV absorption instruments have proven to be a good choice, mainly in air quality monitoring networks. This can be attributed to their easy usage and to their low maintenance as no reagent gases or solutions are needed for their operation (Williams et al., 2006). Usually, they can be manufactured as lightweight, handheld devices, facilitating their application also in non stationary measurements.

UV absorption monitors make use of the characteristic properties of the O_3 molecule to strongly absorb light in the UV range. This absorption can be attributed to the so called Hartley band, which extends from 200 nm to 310 nm, with an absorption maximum at around 254 nm. Light of an active light source, with an emitting wavelength within the Hartley band, passes trough an absorption cell trough which a steady flow of sample air is generated via a pump (see schematic in Fig. 3). The attenuation of the light is measured with a detector at the other side of the absorption cell. As an active light source, mainly mercury (Hg) lamps are used as the principle emission wavelength is at 254 nm coinciding with the absorption maximum of O_3. By measuring the light attenuation, the O_3 concentration of the air inside the measurement cell can be determined using Beer-Lambert law,

$$\frac{I}{I_0} = exp\big(-\sigma \cdot L \cdot [O_3]\big), \tag{12}$$

where I is the intensity of the light measured, I_0 the intensity when no O_3 is present, σ is the O_3 absorption cross section ($\sigma \approx 1 \times 10^{17}$ at 254 nm), L is the optical path length and $[O_3]$ the concentration of O_3 (Williams et al., 2006).
The reference intensity I_0 is determined by letting the air pass through an O_3 scrubber before entering the absorption cell. With a valve, air is alternately send directly into the measurement cell (to measure I) or first passed trough the O_3 scrubber (to measure I_0). Additionally, the temperature and pressure inside the cell are measured. This enables to convert the determined concentration into a mixing ratio using the ideal gas law.

These UV monitors can, however, show significant positive interference when other compounds are present which absorb in the same spectral range and react as well with the O_3 scrubber. This is the case with some volatile organic carbon species, mercury vapour, aromatic photooxidation products, fine aerosols and SO_2 (Kleindienst et al., 1993; Leston et al., 2005; Williams et al., 2006). The sensitivity of UV monitors to these compounds is usually smaller than that to O_3. From the cross-sections of O_3 and SO_2, shown in Fig. 4, we see that the the sensitivity to SO_2 is reduced by a factor of 100 compared to that of O_3. Under ‘normal’ atmospheric conditions these interferences (especially with SO_2) do not play a major role (Kleindienst et al., 1993; Williams et al., 2006) and UV monitors can therefore reliably measure O_3 levels for most urban and industrial locations.

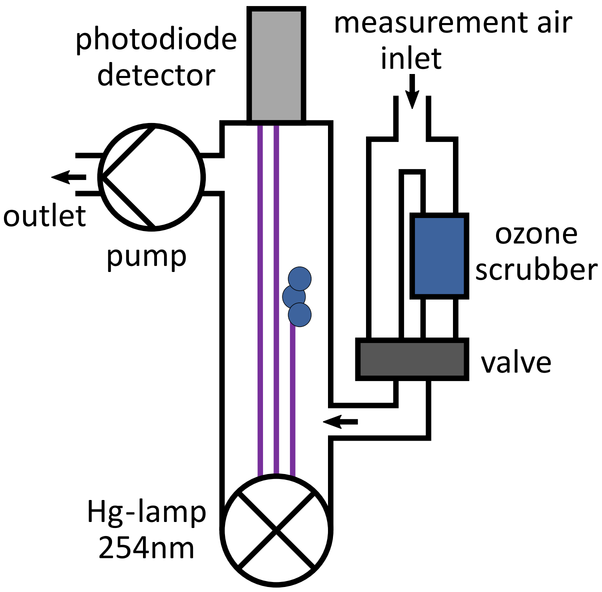

Figure 3: Schematic drawing of a UV absorption monitor. Ambient air is pumped into the absorption chamber, either directly or through an O_3 scrubber. A Hg lamp is positioned on one side of the measurement chamber, while a photodiode detector sits on the opposite side. The detector measures the intensity of light for both the unaltered air and the air passed trough the scrubber. By comparing these two intensity values, the absorption attributed to O_3 and the O_3 concentration can be determined. The absorption is visualised by the O_3 molecule (three blue dots) in the reaction chamber. Figure taken from Bräutigam (2022).

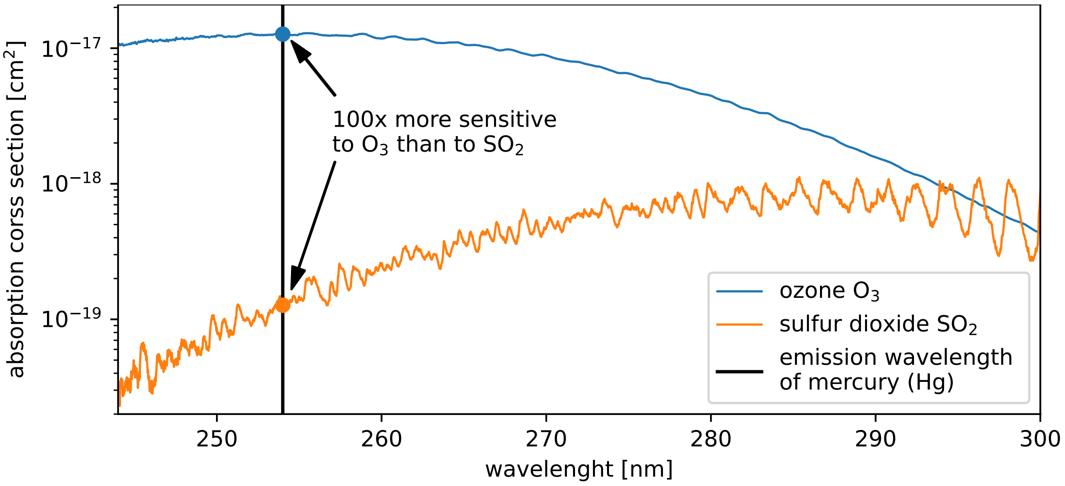

Figure 4: Comparison of cross sections of O_3 (blue) and SO_2 (orange). Additionally, the main emission wavelength of mercury (Hg) at 254 nm is marked (black). The cross sections of the two species deviate by a factor of roughly 100 at 254 nm, causing a 100 times higher sensitivity to O_3 than to SO_2. Figure taken from Bräutigam (2022).

However, when measuring volcanic emissions, SO_2 mixing ratios may reach values in the ppm regime and therefore exceed O_3 mixing ratios by factors of 1000 or more (usual O_3 mixing ratios $\approx$ 40 ppb). Even with the reduced sensitivity for SO_2, this still leads to apparent O_3 mixing ratios of several tens or hundreds of ppb. As a result, techniques to counteract this positive interference have to be employed (e.g. post processing while measuring SO_2 simultaneously: Kelly et al. (2013), or selective SO_2 scrubbers: Surl et al.

(2015), Vance et al. (2010)), which introduce additional error sources.

There are also other measurement techniques to monitor O_3 levels. These include for instance semiconductor metal oxide (SMO) gas sensors and electrochemical monitors. Usually these sensors are less expensive and readily usable but they are also, in most cases, less sensitive and also exhibit cross sensitivities with other atmospheric gases.

To address the issue of interference without adding new uncertainties, using an O_3 monitor based on CL is a viable option.

3.2. Theory of CL monitor operation

In the following, we will present the theory underlying CL O_3 monitors. First, the operation principle is explained, then the theoretical description of the signal and its dependencies are shown. In particular, also the conversion of the measured signal to obtain the O_3 mixing ratio is derived.

3.2.1. Principle and mechanism

The chemiluminescence (CL) phenomenon is characterized by the emission of photons resulting from a chemical reaction. In the context of CL O_3 monitors, the principle of operation relies on the generation of chemiluminescent species through reactions involving O_3. By measuring the emitted photons, it is possible to infer the concentration of O_3.

There are various CL reactions involving O_3 that are employed in CL O_3 monitors. For example, one approach utilizes the chemiluminescence produced by the reaction of O_3 with NO in the gas phase. Additionally, both dry and wet CL instruments can be used, wherein the reaction of O_3 with organic dyes in the condensed phase is exploited (Zahn et al., 2012).

In particular, gas-phase reactions of O_3 with olefins, such as ethylene (C_2H_4), trimethylethylene, and tetramethylethylene, are well-known chemiluminescent reactions (Pitts Jr et al., 1971). Among these reactants, C_2H_4 is arguably the most commonly employed option in CL O_3 monitors, including the one used in this thesis. Nederbragt et al. (1965) were the first to make use of this chemiluminescent reaction to determine O_3 near an accelerator and Warren and Babcock (1970) then described the construction and calibration of such a monitor. However, it should be noted that the luminescence observed in the C_2H_4-O_3 reaction is relatively low compared to the luminescence observed in reactions involving trimethylethylene and tetramethylethylene. An equal or even stronger luminescence was found with several sulfides, such as hydrogen sulfide, dimethyl sulfide and methanethiol.

A great diversity of products can be observed from the reaction of O_3 with C_2H_4, among them excited species leading to the emission of photons on their de-excitation. The emitted photons are measured with the PMT directly connected to the measurement cell (for a full device description see Sec. 4.1).

The emission of photons following the reaction of C_2H_4 and ozone can mainly be attributed to formaldehyde fluorescence (electronically excited formaldehyde ($HCHO^*$)) as well as to $OH^\dagger$ Meinel band emissions (Finlayson et al., 1974). Here, electronically excited species are denoted with $*$, vibrationally excited species with $\dagger$. The emission spectrum of the reaction and the spectrum of formaldehyde fluorescence are shown in Fig. 5 (Finlayson et al., 1974).

In kinetic studies of the reaction, the emission intensities have been found to be first order in the O_3 concentration for pseudo first-order conditions as both emitting species ($HCHO^*$, $OH^\dagger$) show a reaction order of approx. 1 (Finlayson et al., 1974). Pseudo first-order conditions apply also in the configuration of the CL O_3 monitor as C_2H_4 is available in excess during the reaction and thus eliminates the dependence of the reaction rate on the C_2H_4 concentration (C_2H_4 concentration stays relatively constant during the reaction).

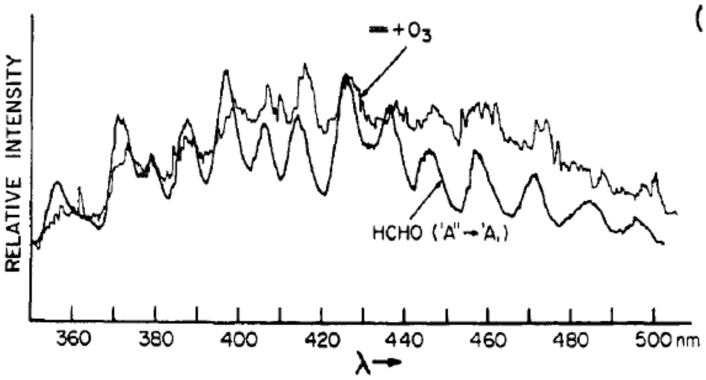

Figure 5: Chemiluminescent emission spectra from the reaction of O_3 with C_2H_4 at 4.5 Torr. Additionally the emission spectrum of electronically excited formaldehyde is plotted for comparison. Even though the two spectra are not identical, similar emission characteristics are visible. Figure taken from Finlayson et al. (1974).

As the light intensity and therefore the number of emitted photons is proportional to the mixing ratio of O_3 the electronic signal of the PMT is also proportional to the mixing ratio of O_3. This is the basis of the CL measurement technique and is explained in more detail in the next section 3.2.2.

Usually, in order to explain the reactions the O'Neal-Blumenstein hydrogen abstraction modification (O'Neal and Blumstein, 1973) in conjunction with the Criegee mechanism is used (Barnes and McGrath, 1986). The general mechanism is shown in the scheme in Fig. 6 (adapted from O'Neal and Blumstein (1973); Barnes and McGrath (1986); Finlayson et al. (1974); Olzmann et al. (1997), picture from Kleindienst et al. (1993)). In this scheme the two reaction pathways for the reaction of O_3 and C_2H_4 are shown.

In the initial reaction (1) Fig. 6 the primary ozonide is formed which can react in several ways:
Reaction (2) Fig. 6 shows the Criegee split, where HCHO and the excited Criegee intermediate (CH_2OO^*) are formed. Further reaction pathways of the Criegee intermediate might explain the $OH^\dagger$ Meinel band emissions via the production of atomic hydrogen (H). The H atoms then react in the following way

$$H + O_3 \longrightarrow OH + O_2 \cdot \tag{13}$$

Reactions (3) Fig. 6 and (4) Fig. 6 show the α hydrogen abstraction (as proposed by O'Neal and Blumstein, 1973) which is thought to explain $HCHO^*$. Additionally, formic acid (HCOOH) is formed.

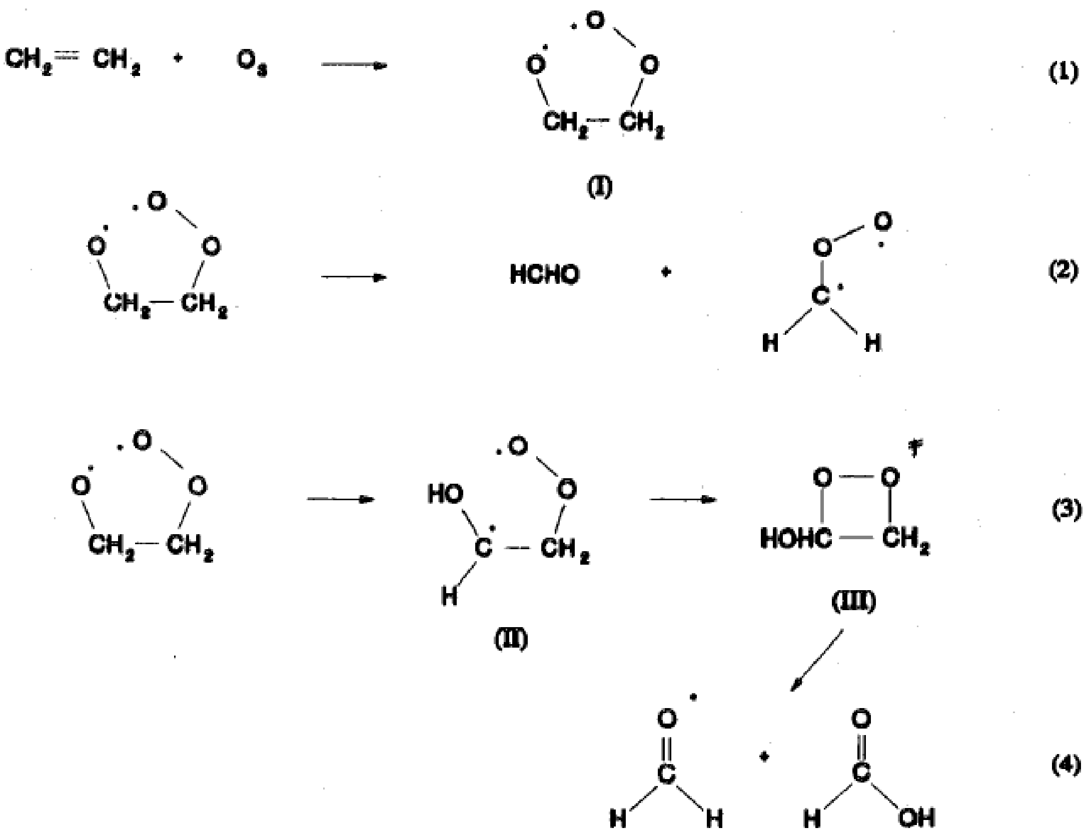

Figure 6: Schematic of the reaction of O_3 with C_2H_4. The first mechanism (reaction 2), called the Criegee split, results in the excited Criegee intermediate. The second mechanism (reactions 3 and 4) show the α hydrogen abstraction modification, which results in the production of electronically excited formaldehyde HCHO* (and formic acid). Figure taken from Kleindienst et al. (1993).

Reaction (2) Fig. 6 shows the Criegee split, where HCHO and the excited Criegee intermediate (CH_2OO^*) are formed. Further reaction pathways of the Criegee intermediate might explain the $OH^\dagger$ Meinel band emissions via the production of atomic hydrogen (H). The H atoms then react in the following way

$$H + O_3 \longrightarrow OH + O_2 \cdot \tag{14}$$

Reactions (3) Fig. 6 and (4) Fig. 6 show the α hydrogen abstraction (as proposed by O'Neal and Blumstein, 1973) which is thought to explain HCHO*. Additionally, formic acid (HCOOH) is formed.

3.2.2. Theoretical signal strength and conversion of measured signal

The reaction kinetics of the reaction of O_3 with C_2H_4 are given by (Atkinson et al., 2006),

$$O_3 + C_2H_4 \longrightarrow \text{products}, \tag{15}$$

$$\frac{d[O_3]}{dt} = -k(T) \cdot [O_3](t) \cdot [C_2H_4](t) \; \left[\tfrac{1}{\mathrm{cm}^3\,\mathrm{s}}\right], \tag{16}$$

$$\text{with} \qquad k(T) = 9.1 \cdot 10^{-15} \exp\left(-\frac{2580}{T}\right) \; \left[\tfrac{\mathrm{cm}}{\mathrm{s}^3}\right], \tag{17}$$

where $k(T)$ is the reaction constant. As C_2H_4 is available in excess, the C_2H_4 concentration can be treated as constant ($[C_2H_4](t) \sim [C_2H_4]_0 = \text{constant}$). The reaction can therefore be approximated as a pseudo first order reaction.
With this assumption, the time-dependent O_3 concentration is obtained by solving the differential equation, Eqn. 16, (separation of variables):

$$[O_3](t) = [O_3]_0 \cdot \exp\left(-k(T) \cdot [C_2H_4]_0 \cdot t\right) \; \left[\tfrac{1}{\mathrm{cm}^3}\right], \tag{18}$$

where $[O_3]_0$ and $[C_2H_4]_0$ are the starting concentrations of O_3 and C_2H_4 respectively.

In order to draw conclusions about the signal strength the number of emitted photons per second γ has to be considered, which is proportional to the reacted O_3 molecules,

$$\text{signal strength} \propto \gamma \propto \text{reacted } [O_3], \tag{19}$$

This is the case since the emitting species ($HCHO^*$, $OH^\dagger$) show a reaction order of approximately 1 for pseudo-first order reactions (see Sec. 3.2).

The reacted O_3 after the flushing time t_{flush} (time needed for the volume of the reaction chamber to be fully exchanged) is given by,

$$\begin{aligned}
\text{reacted } O_3 =& [O_3]_0 - [O_3](t_{\mathrm{flush}}) && (20)\\
=& [O_3]_0 - [O_3]_0 \cdot \exp\left(-k(T) \cdot [C_2H_4]_0 \cdot t_{\mathrm{flush}}\right) \qquad \text{(see Eq. 18)} && (21)\\
=& [O_3]_0 \cdot \Big(1 - \exp\left(-k(T) \cdot [C_2H_4]_0 \cdot t_{\mathrm{flush}}\right)\Big) && (22)\\
=& [O_3]_0 \cdot R(t_{\mathrm{flush}}) \qquad \left[\tfrac{1}{\mathrm{cm}^3}\right], && (23)
\end{aligned}$$

where $R(t_{\mathrm{flush}})$ is the fraction of reacted O_3 (the term in big brackets in Eqn. 22). The flushing time is determined by the measurement cell volume V_{cell} and the flow generated by the pump f_{tot},

$$t_{\mathrm{flush}} = \frac{V_{\mathrm{cell}}}{f_{\mathrm{tot}}}. \tag{24}$$

Following this calculation an expression for the photons generated per second γ can be established,

$$\begin{aligned}
\gamma =& QE \cdot f_{O_3} \cdot \text{reacted } O_3 && (25)\\
=& QE \cdot (f_{\mathrm{tot}} - f_{C_2H_4})[O_3]_0 \cdot R(t_{\mathrm{flush}}) \; \left[\tfrac{1}{\mathrm{s}}\right],
\end{aligned}$$

with QE being the quantum yield of the reaction, f_{O_3} and $f_{C_2H_4}$ the O_3 and C_2H_4 flow respectively. The quantum yield is given by the number of photons per molecule of reacted O_3 and was estimated by Kleindienst et al. (1993) to be $QE = 10^{-7}$. The reaction is believed to be this ineffective since the excited formaldehyde is much more likely to lose its energy through collisions with other molecules than by emitting a photon. The quantum yield also exhibits a temperature and a pressure dependence, however, this is neglected here since no detailed information is found in the literature.

Inserting,

$$c_i = \frac{n_i}{V_{air}} = \frac{V_i}{V_{\mathrm{air}}} \cdot \frac{p}{k_b T} = x_{V,i} \cdot \frac{p}{k_b T} \cdot 10^{-6} \ \left[\frac{1}{\mathrm{cm}^3}\right], \tag{26}$$

with n_i the number of molecules of the respective gas in a given volume of air V_{air} and $x_{V,i}$ the volume mixing ratio of the respective gas (derived from the ideal gas law $pV = nk_bT$), as well as,

$$\begin{aligned} x_{\mathrm{C_2H_4}} &= \frac{f_{\mathrm{C_2H_4}}}{f_{\mathrm{tot}}}, && \qquad (27) \\ f_{\mathrm{C_2H_4}} &= f_{\mathrm{C_2H_4}}(p_{\mathrm{C_2H_4}}), && \text{see Sec. 4.3 for more information,} \qquad (28) \end{aligned}$$

and the temperature dependence of the reaction constant, Eqn. 17, allows to estimate the dependence of the signal from the mixing ratio of O_3 but also from other parameters such as the ambient temperature T, the ambient pressure p and the C_2H_4 pressure after the pressure regulator $p_{\mathrm{C_2H_4}}$:

$$\begin{aligned} \gamma = QE \cdot (f_{tot} - f_{\mathrm{C_2H_4}}(p_{\mathrm{C_2H_4}})) \cdot x_{V,\mathrm{O_3}} \frac{p}{k_b T} \cdot \\ \left[1 - \exp\left(- 9.1 \cdot 10^{-15} \cdot \exp\left(- \frac{2580}{T}\right) \cdot \frac{f_{\mathrm{C_2H_4}}(p_{\mathrm{C_2H_4}})}{f_{\mathrm{tot}}} \cdot \frac{p}{k_b T} \cdot \frac{V_{\mathrm{cell}}}{f_{\mathrm{tot}}}\right)\right]. \end{aligned} \tag{29}$$

This equation does not claim to accurately describe the total number of photons generated per second. This is primarily due to the uncertainty of the quantum yield, as it is essentially an estimation, and since its dependence on ambient temperature and pressure is neglected. However, assuming that Eqn. 29 provides a reasonable approximation of the signal's dependencies, it can be observed that the signal is indeed proportional to the O_3 mixing ratio. Nevertheless, changing ambient conditions also has an influence on the signal.

Since our focus is on determining the O_3 mixing ratio, Eqn. 29 can be rearranged to express the mixing ratio as a function of the generated photons and the other influencing parameters,

$$\begin{aligned} x_{V,\mathrm{O_3}} =& \gamma \cdot \frac{k_b}{QE} && (30) \\ & \cdot \frac{T}{p \cdot (f_{tot} - f_{\mathrm{C_2H_4}}(p_{\mathrm{C_2H_4}})) \cdot \left[1 - \exp\left(-9.1 \cdot 10^{-15} \cdot \exp\left(-\frac{2580}{T}\right) \cdot \frac{f_{\mathrm{C_2H_4}}(p_{\mathrm{C_2H_4}}) p V_{\mathrm{cell}}}{f_{\mathrm{tot}} k_b T f_{\mathrm{tot}}}\right)\right]} \\ =& \gamma \cdot \frac{k_b}{QE} \cdot c(p_{\mathrm{C_2H_4}}, p, T), && (31) \end{aligned}$$

where $c(p_{\mathrm{C_2H_4}}, p, T)$ is the 'conversion factor' given in $\frac{\mathrm{K\,s}}{\mathrm{Pa\,mL}}$. For standard conditions, $p_{\mathrm{C_2H_4},0} = 1300\,\mathrm{mbar}$, $p_0 = 1013\,\mathrm{hPa}$, $T_0 = 20\,°\mathrm{C}$, the conversion factor is given by $c(p_{\mathrm{C_2H_4},0}, p_0, T_0) = 4.18 \times 10^{-4}\,\frac{\mathrm{K\,s}}{\mathrm{Pa\,mL}}$.
From Eqn. 31 it becomes apparent that additionally to the signal itself also $p_{\mathrm{C_2H_4}}$, p and T have to be recorded in order to draw conclusions about the O_3 mixing ratio.

It is important to acknowledge that the absolute values obtained from the theoretically calculated signal γ cannot be directly compared to the actual measured signal, the output voltage of the PMT, denoted as S. This limitation arises because, firstly, the theoretical description does not provide precise values for the total number of generated photons (due to the uncertainty of the quantum yield) and secondly because, the measured signal is proportional to the number of generated photons, but the conversion factor is not fully known. Several factors contribute to this uncertainty.
One being that, the exact number of photons that effectively reach the photosensitive area of the PMT cannot be accurately determined. Additionally, other characteristics of the PMT, such as the gain and the dark current, impact the measured signal. The dark current, in particular, acts as a temperature-dependent offset and must be considered during the calibration process.
These considerations show the necessity of calibration (see Sec. 5.2).

3.2.3. Signal strength dependencies

In order to understand the impact of changes in the ambient parameters on the signal, it is useful to vary one parameter while maintaining the rest at a constant value. This approach allows for a partial separation of effects from the different parameters and offers an insight into the nature and magnitude of their respective impacts on the measured signal. This approach is interesting because these conditions can be replicated in experiments, facilitating comparisons between theoretical predictions and experimental observations. The relative signal is especially useful in this context. It enables an evaluation of the dependencies without being concerned about absolute values, eliminating the previously mentioned problem that theoretical and experimental signal cannot readily be compared.

It is crucial to note that the signal shows several dependencies, while it is linear in the O_3 mixing ratio, its dependence from the other parameters, ambient pressure p, ambient temperature T, and C_2H_4 flow $f_{C_2H_4}(p_{C_2H_4})$, is not linear. In the following, the C_2H_4 pressure $p_{C_2H_4}$ instead of the C_2H_4 flow $f_{C_2H_4}$ is used as the influencing parameter. This is done as the flow $f_{C_2H_4}$ is directly dependent on $p_{C_2H_4}$. In Sec. 4.3 this dependence is discussed in detail.

To investigate the signal's dependence on these three parameters (p, T and $p_{C_2H_4}$), the considered parameter is varied while the other two are kept constant at a specific value. For the C_2H_4 pressure a range of $550 - 2300$ mbar with a standard value of 1300 mbar is used. The ambient pressure is assumed to be in a range of $700 - 1100$ hPa, with a reference value of 1013 hPa. For the temperature the range is set between $5 - 40$ °C, for the standard value a temperature of 20 °C is chosen. Since the dependence of the relative signal from one parameter changes as the other parameters are varied three curves are plotted each, shown in Fig. 7. Here, once the 'standard' parameters for the other parameters (blue curves) as well as the the minimum (orange) and maximum (green) values are used, as these provide the largest deviations to the 'standard' dependence, determined using the most common parameter values. It can be seen that the signal shows the largest variations with changing C_2H_4 pressure. However, also variations in the ambient pressure and temperature lead to notable changes in the signal. This emphasizes the importance of monitoring these three parameters and later correct for their influence in order to draw meaningful conclusions about the O_3 mixing ratio.

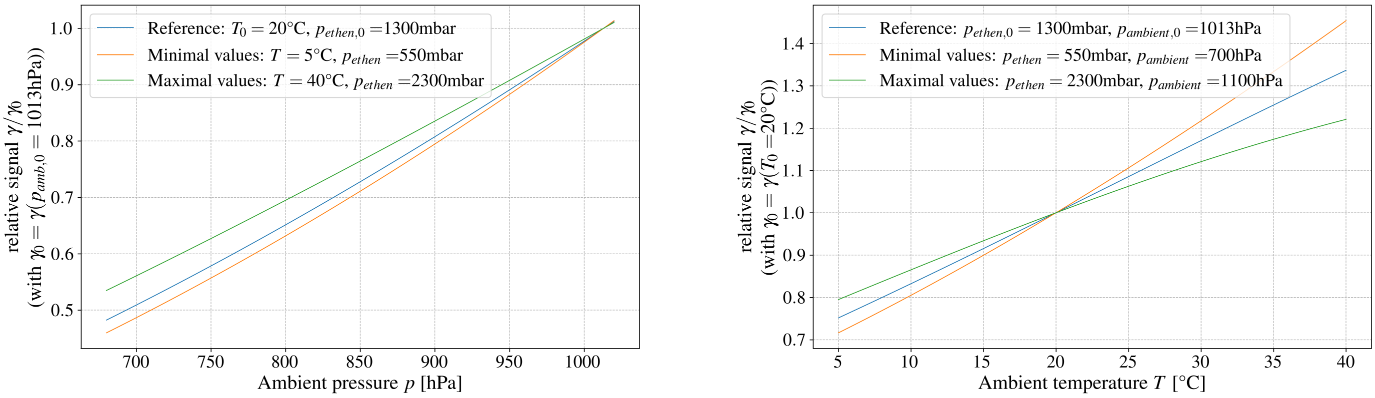

(a) Relative signal dependence of ambient pressure.

(b) Relative signal dependence of ambient temperature.

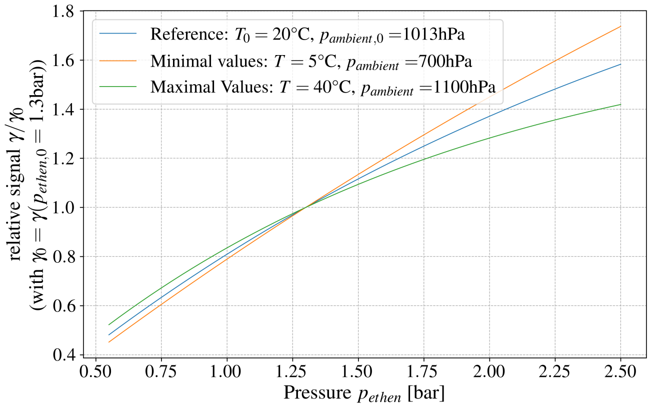

(c) Relative signal dependence of C_2H_4 pressure.

Figure 7: Theoretical relative signal dependencies for three parameters ambient pressure, ambient temperature and C_2H_4 pressure. These curves are obtained by varying only one parameter and keeping the other two at a constant value. It is important to note that the relative signal's dependence on one parameter changes as the other parameters are altered. To account for this, once the minimum, the standard and the maximum values of the parameters which are held constant are used.

4. Construction of the monitor

4.1. Configuration/Description

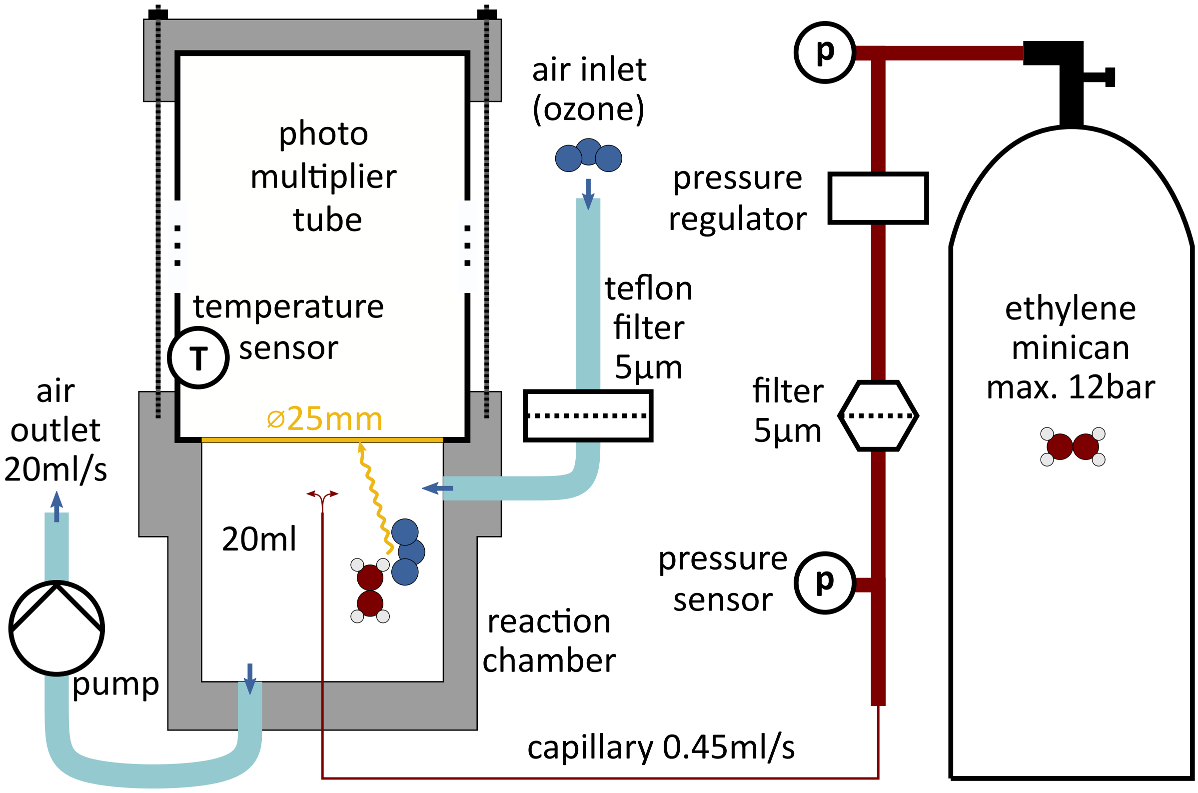

Figure 8: Schematic drawing of the CL O_3 monitor setup (without the electronics); compare to the photo of the setup in Fig. 9. Figure taken from Bräutigam (2022).

In this chapter we present the construction of VOLCANO$_3$. The design is based on the working principle explained in Sec. 3.2. In Fig. 8 a schematic drawing of the monitor is shown (Bräutigam, 2022). A photograph of the monitor is depicted in Fig. 9. In the following the configuration of the monitor is described, referencing the numbered components in Fig. 9. The data sheets of the referenced components are available in Appendix C.2, an in-depth description can also be found in Bräutigam (2022).

The monitor is powered by a Li-ion Battery (K) which is connected to a PowerBoost circuit (L) to supply the Raspberry Pi microprocessor board (N) with a constant voltage of 5 V. The 5 V pins of the Raspberry Pi are used to power the PMT, and the rest of the electronic components of the monitor. The monitor has a power consumption of ~ 3 W. Ambient air enters the instrument through an aerosol filter (A), made from PTFE (Teflon) with glass fibre supporting fabric and a pore size of 5 µm. Since O_3 is a very reactive gas, all components that come into contact with the measurement air before the reaction chamber have to be made from an inert material, as for example Teflon. The measurement air is then directed trough a black teflon hose (two windings to suppress photons entering the measurement cell trough the hose) into the measurement cell/reaction chamber (B), where it is mixed with C_2H_4. The measurement cell is made from aluminium with a volume of $V = 20$ mL. It is fixed to the PMT photo cathode using a clamp (D).

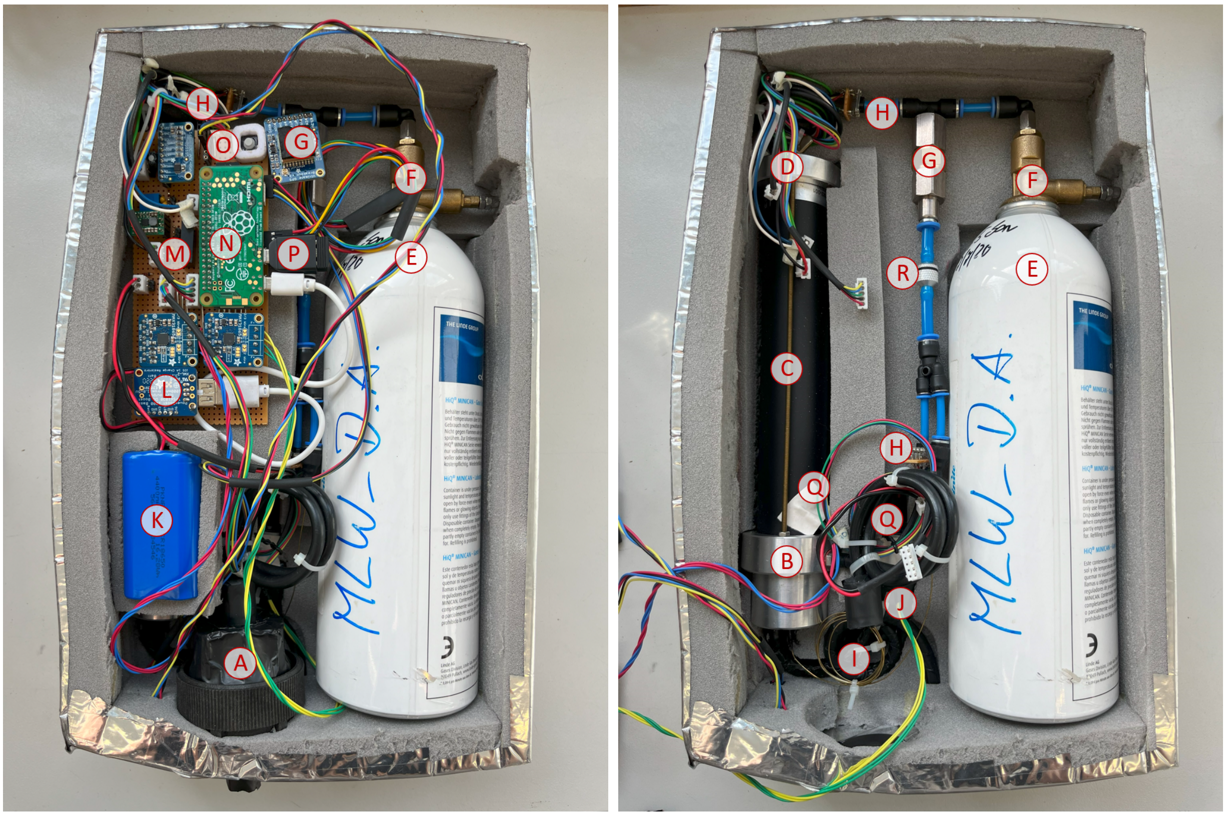

(a) Fully assembled monitor with lid open, view on the electronics.

(b) Electronics are removed to allow the view on the PMT.

(c) Front view of the monitor with inlet, outlet, display and ambient sensor.

(d) Side-view on the monitor fully closed.

A	Inlet filter	**L**	Booster for power supply
B	Reaction chamber	**M**	Circuit board
C	Photomultiplier module	**N**	Raspberry Pi Zero computer
D	Fixing clamp	**O**	Power-off button
E	Ethylene C_2H_4 Minican	**P**	USB drive
F	Manual valve	**Q**	PT1000 temperature sensor (PMT, pump)
G	Mini pressure regulator	**R**	Filter
H	Pressure sensor (Minican, capillary)	**S**	Display
I	Capillary	**T**	Ambient sensor (temperature, pressure)
J	Pump	**U**	Exhaust
K	Lithium-polymer battery		

Figure 9: Assembly of the monitor.

Ethylene is supplied from a Minican (E, $V_{\mathrm{bottle}} = 1\,\mathrm{L}$, maximum overpressure $p_{\mathrm{bottle}} = 12\,\mathrm{bar}$), which can be opened with the manual valve (F). With a Pressure sensor (H) the fill level of the Minican is monitored. The Mini pressure regulator (G), reduces the overpressure of the C_2H_4 Minican to around 1.5 bar. Since this is a lightweight pressure regulator the back pressure $p_{C_2H_4}$ (pressure after the pressure regulator, before the capillary) changes with time. In order to monitor the changes in the back pressure a Pressure sensor (H) is installed after the pressure regulator. The C_2H_4 flow into the measurement cell is regulated through the capillary (I). To prevent the capillary from becoming clogged a filter (R) is inserted upstream.

The emitted photons in the measurement cell reach the photosensitive area of the PMT (Photosensor Module H10493-001 from Hamamatsu Photonics GmbH). The module features a bialkali cathode, that has the required spectral response from 300 nm to 600 nm with a peak sensitivity wavelength of 420 nm. It incorporates a high voltage power supply and only requires an input voltage of ±11.5 V to ±15.5 V. With a DC/DC-converter the 5 V supplied from the Raspberry Pi's 5 V pin are converted to the needed voltage range. A control voltage between +0.5 V and +1.4 V has to be supplied to adjust the gain (i.e. the high voltage) of the PMT (white cable). This is done with a 10 kΩ potentiometer dividing the provided reference voltage of 2.5 V (blue cable). The module also incorporates a low noise amplifier for the output voltage. The output voltage, consisting of a series of voltage spikes proportional to the O_3 mixing ratio, is first smoothed using an RC integrator circuit and then read out by an Analog-to-digital-converter (ADC). More details on the PMT read out process can be found in the next section, Sec. 4.2.

The gas mixture is transported out of the instrument through the airflow generated by the Rotary vane pump (J, model G 6/01-K-LC), which is connected to the gas outlet of the measurement cell through a hose. The exhaust hose of the instrument (U) is also wrapped in black tape to prevent photons entering the measurement cell. The flow rate of the pump can be controlled with the supply voltage of the pump. The Step-down converter enables to change the supply voltage seamlessly between $0.5 - 4.8\,\mathrm{V}$ (for an input voltage of 5 V), changing the flow rate from around $5 - 34\,\frac{\mathrm{mL}}{\mathrm{s}}$.
Ambient temperature and pressure are monitored with a Bosch BMP280 breakout board (T). For temperature measurements at the PMT and the pump resistance temperature detectors PT1000 (Q) are used.

With the Raspberry Pi the following parameters are read out roughly 3 times per second and the current value is written into a .txt-file on the USB drive (P) (see Fig. 10).

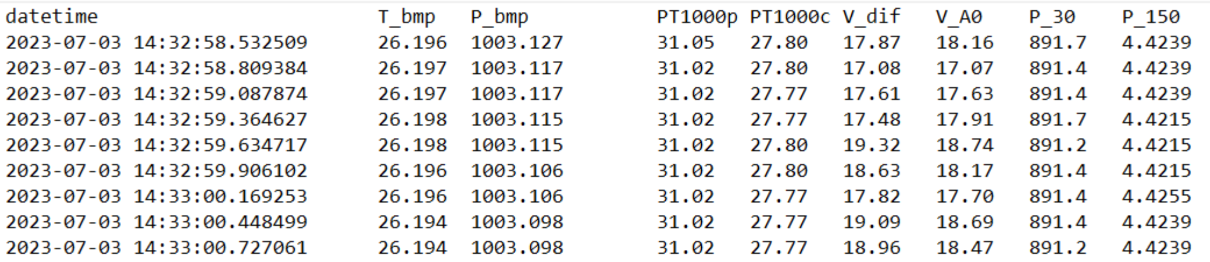

```
datetime                      T_bmp   P_bmp           PT1000p PT1000c V_dif   V_A0    P_30    P_150
2023-07-03 14:32:58.532509    26.196  1003.127        31.05   27.80   17.87   18.16   891.7   4.4239
2023-07-03 14:32:58.809384    26.197  1003.117        31.02   27.80   17.08   17.07   891.4   4.4239
2023-07-03 14:32:59.087874    26.197  1003.117        31.02   27.77   17.61   17.63   891.4   4.4239
2023-07-03 14:32:59.364627    26.198  1003.115        31.02   27.77   17.48   17.91   891.7   4.4215
2023-07-03 14:32:59.634717    26.198  1003.115        31.02   27.80   19.32   18.74   891.2   4.4215
2023-07-03 14:32:59.906102    26.196  1003.106        31.02   27.80   18.63   18.17   891.4   4.4215
2023-07-03 14:33:00.169253    26.196  1003.106        31.02   27.77   17.82   17.70   891.4   4.4255
2023-07-03 14:33:00.448499    26.194  1003.098        31.02   27.77   19.09   18.69   891.4   4.4239
2023-07-03 14:33:00.727061    26.194  1003.098        31.02   27.77   18.96   18.47   891.2   4.4239
```

Figure 10: Example text file as it is produced from the monitor. The current internal time of the Raspberry Pi, the ambient temperature (T_bmp) and pressure (P_bmp), the temperature at the pump and the cell (PT1000p and PT1000c, respectively), the differential output and the output to external ground from the ADC (V_dif and V_A0), as well as the pressure of the Minican P_150 and the pressure before the capillary P_30 are logged.

Key parameters, such as the current value of the output voltage of the PMT, the pressure of the C_2H_4 Minican, the C_2H_4 pressure as well as the temperature at the measurement cell and at the pump, are displayed on a small, black-and-white Adafruit PiOLED display (S). The values are updated roughly every 3 s.
The monitor also features the Ultimate GPS module (G). It is used to set the internal clock of the Raspberry Pi upon boot if no connection to the server can be established. This is needed during field measurements when no internet connection is available. To enhance efficiency, the system does not log GPS data. This decision is due to the considerable amount of time required to read from the GPS module, which significantly increases the interval between log entries. Instead, when GPS information is necessary, the system utilises the recorded data from other instruments (this is done during the field measurements, see Sec. 8).

The instrument, as shown in Fig. 9, has the dimensions 38 x 20 x 11cm and weighs around 1500 g. The housing of the instrument mainly consists of a closed cell, cross linked polyethylene PE-Foam. It was chosen since it is a light weight and flexible material, with low water absorption and water vapour transmission rates as well as resistance to chemical weathering. To construct the housing, single layers of foam with contours of the components cut into them are glued on top of each other. With this the components are embedded in the foam, providing impact protection as well as shielding the PMT against unwanted photons. To give additional stability polyvinyl chloride PVC hardfoam plates are attached at the bottom as a base plate and on top to support lid. These plates can be taken of when needed to save weight (mainly for the drone based measurements). The monitor in this configuration weights then around 1200 g. The lid can be lifted up and is fixed with two Velcro fasteners. The sides of the lid are made of rubber sponge to prevent light from entering the instrument.
The entire housing is wrapped in plastic aluminium tape to further stabilize the foam, increase the durability of the housing against corrosive gases, and make sure that the housing is lightproof.

4.2. PMT readout

Here, we describe how the PMT is read out. The PMT output signal consist of a series of voltage spikes with varying height and durations below 20 µs. In the current setup of the monitor, however, we use a passive RC integrator circuit to smooth the signal before reading it out using the ADC and Raspberry Pi. This is a simple yet effective method which shows similar accuracy compared to counting the number of spikes, which is shown in the following.

Using a resistor, $R = 1\,k\Omega$, and a capacitance, $C = 100\,\mu F$, the integrator circuit has a time constant of $\tau = R \cdot C = 10^3\,\Omega \cdot 10^{-4}\,F = 10^{-1}\,s$. This is a reasonable choice since the flushing time of the reaction chamber, which limits the time resolution of the O_3 measurement, is 1 s (for more details on the response time of the monitor see Sec. 5.5). Also, 0.1 s is long compared to the duration of a spike (20 µs). The integrator circuit's characterization can be found in Appendix C.5.

In order to compare the output signal of the PMT with the output signal of the RC integrator, we simultaneously record the output of the PMT and the integrator using an oscilloscope. Several measurements with varying O_3 mixing ratios (0 ppb corresponding to the dark current, 150 ppb) and distinct controlled light conditions are performed. Fig. 11

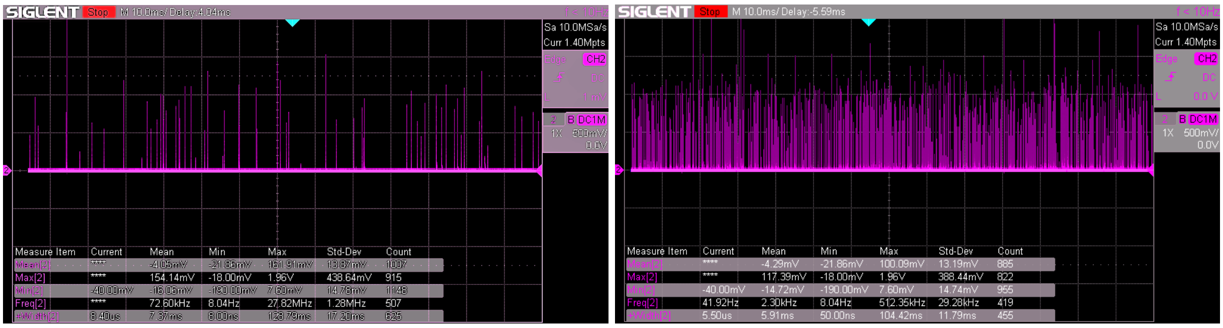

Measure Item	Current	Mean	Min	Max	Std-Dev	Count
Mean[2]	****	-4.05mV	-21.86mV	161.91mV	13.87mV	1007
Max[2]	****	154.14mV	-18.00mV	1.96V	438.64mV	915
Min[2]	-40.00mV	-16.06mV	-190.00mV	7.60mV	14.78mV	1148
Freq[2]	****	72.60kHz	8.04Hz	27.82MHz	1.28MHz	507
+Width[2]	8.40us	7.37ms	8.00ns	128.79ms	17.20ms	625

Measure Item	Current	Mean	Min	Max	Std-Dev	Count
Mean[2]	****	-4.29mV	-21.86mV	100.09mV	13.19mV	885
Max[2]	****	117.39mV	-18.00mV	1.96V	388.44mV	822
Min[2]	-40.00mV	-14.72mV	-190.00mV	7.60mV	14.74mV	955
Freq[2]	41.92Hz	2.30kHz	8.04Hz	512.35kHz	29.28kHz	419
+Width[2]	5.50us	5.91ms	50.00ns	104.42ms	11.79ms	455

(a) Signal for 0 ppb. Each grid cell corresponds to 10 ms on the x-axis and 500 mV on the y-axis.

(b) Signal for 150 ppb. Each grid cell corresponds to 10 ms on the x-axis and 500 mV on the y-axis.

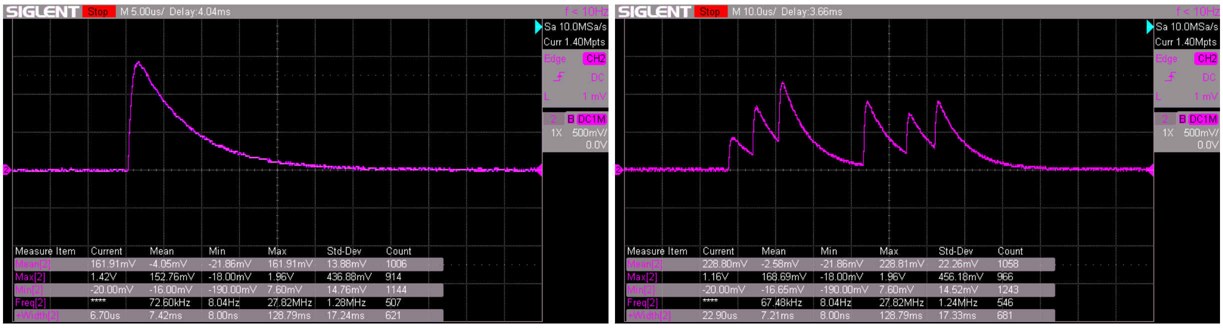

Measure Item	Current	Mean	Min	Max	Std-Dev	Count
Mean[2]	161.91mV	-4.05mV	-21.86mV	161.91mV	13.88mV	1006
Max[2]	1.42V	152.76mV	-18.00mV	1.96V	436.88mV	914
Min[2]	-20.00mV	-16.00mV	-190.00mV	7.60mV	14.76mV	1144
Freq[2]	****	72.60kHz	8.04Hz	27.82MHz	1.28MHz	507
+Width[2]	6.70us	7.42ms	8.00ns	128.79ms	17.24ms	621

Measure Item	Current	Mean	Min	Max	Std-Dev	Count
Mean[2]	228.80mV	-2.58mV	-21.86mV	228.81mV	22.26mV	1058
Max[2]	1.16V	168.69mV	-18.00mV	1.96V	456.18mV	966
Min[2]	-20.00mV	-16.65mV	-190.00mV	7.60mV	14.52mV	1243
Freq[2]	****	67.48kHz	8.04Hz	27.82MHz	1.24MHz	546
+Width[2]	22.90us	7.21ms	8.00ns	128.79ms	17.33ms	681

(c) Zoom into single spikes for 0 ppb. Each grid cell corresponds to 5 µs on the x-axis and 500 mV on the y-axis on the y-axis.

(d) Zoom into single spikes for 150 ppb. Each grid cell corresponds to 10 µs on the x-axis and 500 mV on the y-axis.

Figure 11: Output voltage of PMT measured using an oscilloscope.

shows the PMT output signal for 0 ppb and 150 ppb of O_3 for one of those measurements. The signal for 0 ppb of O_3 displays notably fewer spikes compared to that of 150 ppb, indicating that the number of spikes is proportional to the number of photons. In the measurement we can also see that the spike heights vary. This variation in spike heights is caused by the statistical distribution in the number of secondary electrons generated at the dynodes of the PMT for a single photon hitting the photo cathode (Hergert, 1997; Kissick et al., 2010). Additionally, when several photons hit the photo cathode simultaneously, the height of the voltage spike is given by the sum of the spike heights of the single photons (Kissick et al., 2010). Therefore, when only counting the spikes conclusions about the generated number of photons are not fully reliable, especially for larger signals.

An algorithm is employed to count the spikes of the PMT output in every $\frac{1}{3}$s period and find the spike heights. During this $\frac{1}{3}$s period also one value (mid point value) of the RC integrator output is sampled. This most closely mimics how the signal of the RC integrator is sampled in the normal setup using the ADC. More details can be found in Appendix C.4. The rolling mean and the rolling standard deviation over one second are calculated for both output signals in order to compare the two techniques.

We plotted the rolling mean of the spike numbers against that of the RC integrators output voltage, depicted in Fig. 12a. While most measurements have a total measurement duration of 7 s, there are additional measurements with a time span of only 0.7 s (see legend in Fig. 12a). The data points stemming from this measurement show an increased spike count compared to those from the 7 s measurements. This might be related to the resolution in that sense that the oscilloscope cannot resolve all spikes and some are 'lost' for longer measurement durations. A similar explanation might relate to the

spike-counting algorithm. For longer measurement durations the spikes are spaced more closely together, possibly leading to the algorithm being unable to detect all spikes.
For the relevant RC integrator output regime, up until an output voltage of 100 mV (100 mV≈200 ppb), the results show an almost linear relation between the measured average RC output voltage and spike count. To this range a linear function is fitted, shown in Fig. 12a. However, at higher RC output voltages, around 150 mV, the relation clearly deviates from the linear dependence and the curve flattens. This might be due to a stronger increase in high amplitude spikes (compared to smaller spikes) since more photons might hit the photo cathode at the same time (Appendix C.4). If this is the case, using the RC integrator to smooth the signal should provide more reliable results.
However, another potential factor for the deviation from the linear relationship could be again the spike-counting algorithm, which might not detect all spikes consistently, especially when numerous spikes are detected in a brief time span. A closer examination of the detected spikes by zooming into the measurements shows that most spikes are detected reliably (see Appendix C.4 Fig. 48), a general conclusion on the reliability of the algorithm is however still difficult. The deviation from the linear relationship might therefore also be an artefact of the evaluation, though this is not likely.
Nonetheless, during ambient measurements usually less than ∼75 mV RC integrator output voltage (corresponding to 150 ppb) are measured. During normal measurements the flattening of the curve therefore does not affect the results.

By dividing the rolling standard deviation with the rolling mean, the relative noise of the two techniques can be compared. A two dimensional histogram is used to compare the relative noise of the spike count against the relative noise of the RC integrator, shown in Fig. 12b. To the data a linear function is fitted. This fit and the line of unit slope for reference are shown in the histogram. The fit parameter of 0.87 suggests that the relative noise from spike counting is approximately 87% that of the RC integrator.

Despite the slight loss in precision with the RC integrator, its overall impact might even be beneficial, making it a viable option for use.

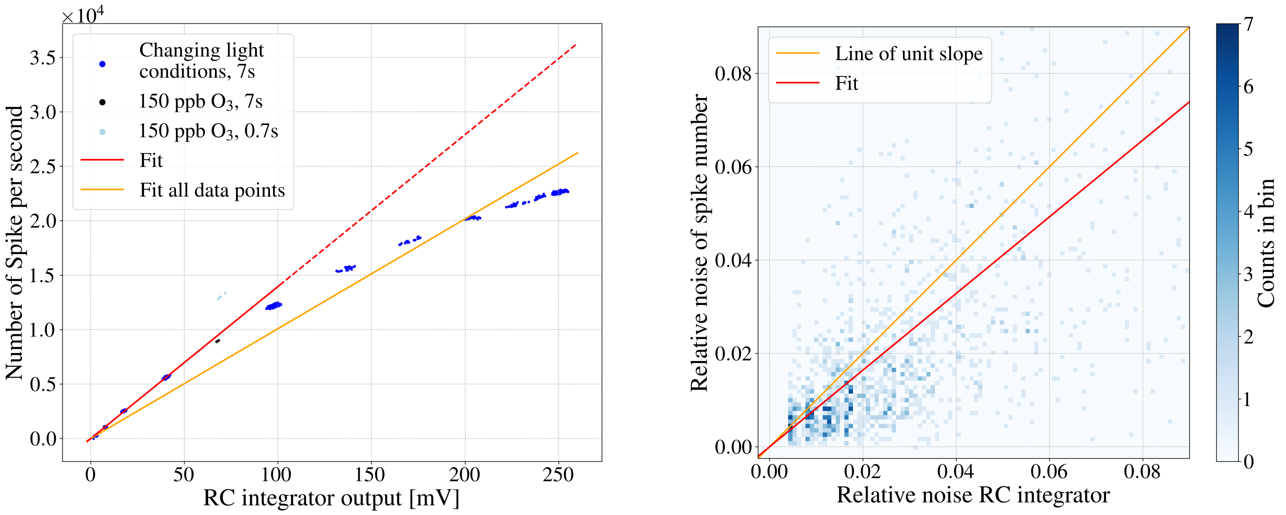

(a) Number of spikes per second plotted against the output voltage of the integrator circuit.

(b) Relative noise of spikes per second plotted against the relative noise of the output voltage of the integrator circuit.

Figure 12: Comparison of the PMT output with the output of the RC integrator.

4.3. Ethylene supply and flow

In Sec. 3.2.3 it was demonstrated that the signal strength is highly dependent on the C_2H_4 flow. Consequently, the flow rate of C_2H_4 is a crucial parameter in calculating the O_3 mixing ratio from the measured signal and an important consideration during the construction of the monitor to optimize signal strength. Here, the regulation of the C_2H_4 flow into the measurement cell using a pressure regulator and a capillary is described and characterised.

A capillary to regulate the C_2H_4 flow can be used since the flow f trough a capillary is determined by the pressure difference Δp between its ends. Here, a Minican is used to supply C_2H_4. The C_2H_4 pressure is first lowered to an appropriate value by a pressure regulator. However, due to the desire for a lightweight monitor, a small and light pressure regulator is selected, which does not provide a stable pressure. As a result, the C_2H_4 flow changes during and between measurements. Time series of the C_2H_4 pressure, the pressure before the capillary, for several measurements are shown in Fig. 13. In characteristic time series, upon opening the valve of the C_2H_4 Minican, the pressure initially rises to approximately 2300 mbar, then rapidly drops to about 1500 mbar, followed by further decrease with a gradient of $\sim 3.5\,\frac{\text{mbar}}{\text{min}}$. Tapping the pressure regulator leads to a sudden increase in back pressure. Closing and opening the valve at the C_2H_4 Minican exhibits the same pressure characteristics as when the valve is opened initially.

Although the overall pressure decrease after opening the valve follows a similar pattern, the specific course and values vary each time, as can be seen in Fig. 13. This highlights the importance to constantly monitor the C_2H_4 flow to account for changes during a measurement as well as to facilitate comparability of different measurements.

When considering the Reynolds number of the flow (more details can be found in Appendix C.6), we see that the flow is considered to be laminar.

The relation between a laminar flow f and the pressure difference Δp is known as the Hagen-Poiseuille equation, which assumes an incompressible medium (Roedel and Wagner, 2017). Here we are dealing with a compressible medium. Therefore, in order to describe the laminar flow of C_2H_4 through a capillary a modified version of the commonly known Hagen-Poiseuille equation has to be considered. This version can be derived from the incompressible version (Wißdorf et al., 2016),

$$\text{incompressible:} \qquad f = \frac{dV}{dt} = \frac{\pi\, r^4\, \Delta p}{8\,\eta\, l} = \frac{\pi\, r^4\, p_{C_2H_4}}{8\,\eta\, l} = a \cdot p_{C_2H_4} \tag{32}$$

$$\text{with } a = \frac{\pi\, r^4}{8\,\eta\, l} = 1 \times 10^{-6}\,\frac{\text{mL}}{\text{Pa s}} \tag{33}$$

$$\text{compressible:} \qquad f = \frac{dV}{dt} = \frac{\pi\, r^4}{8\,\eta\, l} \cdot \frac{p_1^2 - p_2^2}{2 p_1}. \tag{34}$$

Here r denotes the inner radius, l the length of the capillary, η the viscosity of the medium, p_1 is the pressure before the capillary and $p_2 \approx 1013$ hPa is the pressure after the capillary. Since the pressure measurement before the capillary is an overpressure (pressure measured relative to ambient pressure) the equality $\Delta p = p_{C_2H_4}$ holds true, simplifying the incompressible version (see Eqn. 32). The equation for the compressible case has to be slightly

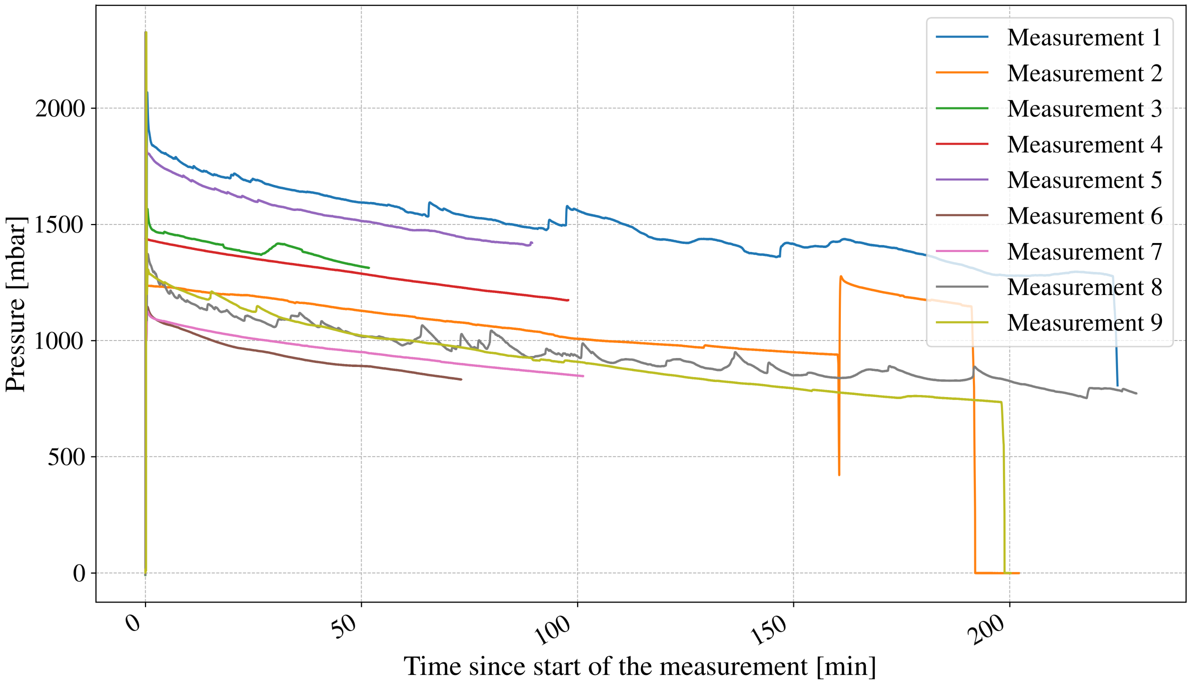

Figure 13: Time series of the back pressure from several different measurements. The time series show a similar course in time, but deviations are clearly visible. After opening the valve at the Minican at time $t = 0$ and a strong initial rise, the pressure drops significantly, before flattening. The following decrease in C_2H_4 pressure over time varies greatly in between measurements. The reason for these variation is not known. Tapping the pressure regulator leads to steep jumps in the pressure.

rearranged in order to compare it to the measurement,

$$f = \frac{\pi\, r^4}{8\,\eta\, l} \cdot \frac{(p_{C_2H_4} + p_2)^2 - p_2^2}{2 \cdot (p_{C_2H_4} + p_2)} = \frac{\pi\, r^4}{16\,\eta\, l} \cdot \frac{p_{C_2H_4}^2 + 2p_2 p_{C_2H_4}}{p_{C_2H_4} + p_2}, \tag{35}$$

$$= a \cdot \frac{p_{C_2H_4}^2 + 2b \cdot p_{C_2H_4}}{p_{C_2H_4} + b}, \tag{36}$$

$$\text{with } a = \frac{\pi\, r^4}{16\,\eta\, l} = 1 \times 10^{-6}\,\frac{\mathrm{mL}}{\mathrm{Pa\,s}}, \tag{37}$$

$$\text{and } b = p_2 \approx 1 \times 10^5\,\mathrm{Pa}. \tag{38}$$

$$\tag{39}$$

Here, the following values are used: $\eta = 9.8 \times 10^{-6}\,\mathrm{Pa\,s}$, $r = 0.075\,\mathrm{mm}$ and a length of $l = 60\,\mathrm{cm}$ (these are the characteristics of the used metal capillary).

With this relation between the flow and the pressure, it is possible to only measure the C_2H_4 pressure $p_{C_2H_4}$ and calculate the C_2H_4 flow from that. Measuring the pressure is much more easily realized compared to measuring the flow and saves weight and space.

With flow calibration measurements the actual dependence of the flow from $p_{C_2H_4}$ can be determined and compared to the theoretical calculations. These measurements are done using a pneumatic trough, the setup is depicted in Fig. 14.

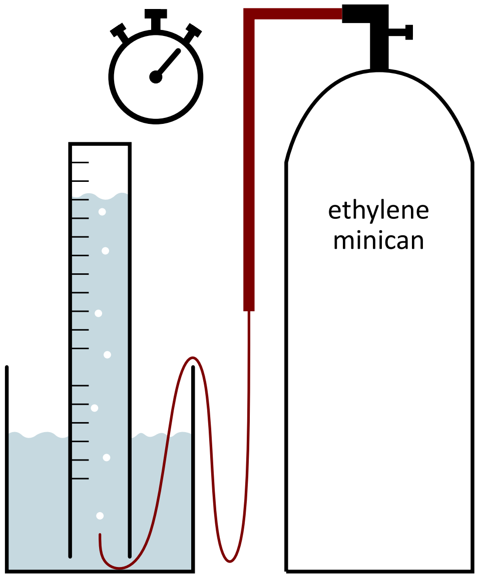

Figure 14: Schematic of a pneumatic trough to measure the volume flow of C_2H_4 through the capillary. The capillary is inserted on the underside of the fully-filled measuring cylinder ($V = 20\,\text{ml}$) and the time t for C_2H_4 to displace certain volume V of water is measured. Figure taken from Bräutigam (2022).

A measuring cylinder ($V = 20\,\text{mL}$), fully filled with water, is placed upside down in a larger trough and the capillary is inserted on the underside. The constant C_2H_4 flow displaces the water in the measuring cylinder and the time t for C_2H_4 to displace a certain volume V of water is measured. Simultaneously the pressure before the capillary $p_{\mathrm{C_2H_4},start}$ and $p_{\mathrm{C_2H_4},end}$ is measured, to determine the average C_2H_4 pressure $p_{\mathrm{C_2H_4}}$ over this time period.

To validate these measurements the C_2H_4 flow is additionally determined trough the volume loss in the Minican. With pressure sensor (H, see Fig. 9) the fill level of the Minican p_{bottle} is constantly monitored during a measurement. This enables us to determine the volume loss in the Minican V over the respective time span t,

$$V = \frac{\Delta p_{\text{bottle}} \cdot V_{\text{bottle}}}{p_{\text{ambient}}} = \frac{(p_{\text{Start,bottle}} - p_{\text{End,bottle}}) \cdot V_{\text{bottle}}}{p_{\text{ambient}}}, \tag{40}$$

with $p_{\text{ambient}} = (1013 \pm 15)\,\text{hPa}$, $V_{\text{bottle}} = 1\,\text{L}$. For the pressure measurements of the Minican (start and end pressure equally, from which the volume is determined) an uncertainty that is twice as large as the standard deviation around the zero point of the pressure sensor is assumed. With the time during which the valve at the C_2H_4 Minican is opened, the mean C_2H_4 flow during the measurement can be calculated. For the start and end time an uncertainty of 2 s is used. In order to connect the volume flow with the corresponding $p_{\mathrm{C_2H_4}}$, the mean pressure $p_{\mathrm{C_2H_4},\text{ mean}}$ (and the standard deviation as uncertainty measure) during this time span are determined.

The results from both the pneumatic trough technique and the volume loss technique are shown in Fig. 15. The data points determined with the different techniques agree within the uncertainty ranges, except for one outlier. However, the flow determined from the volume loss in the Minican gives slightly smaller flow values for the same $p_{\mathrm{C_2H_4}}$.
Both Eqn. 36 and 32 are used as functions to be fitted to the data points. It can be seen that the fit from the compressible and the incompressible Hagen-Poiseuille equation are nearly indistinguishable from one another.
Additionally, dependencies calculated theoretically using the manufacturer's information on the radius are shown. The theoretically determined compressible dependency does not closely match any of the experimental data. For high C_2H_4 pressures, the theoretically determined dependency from the incompressible equation aligns well with the measured

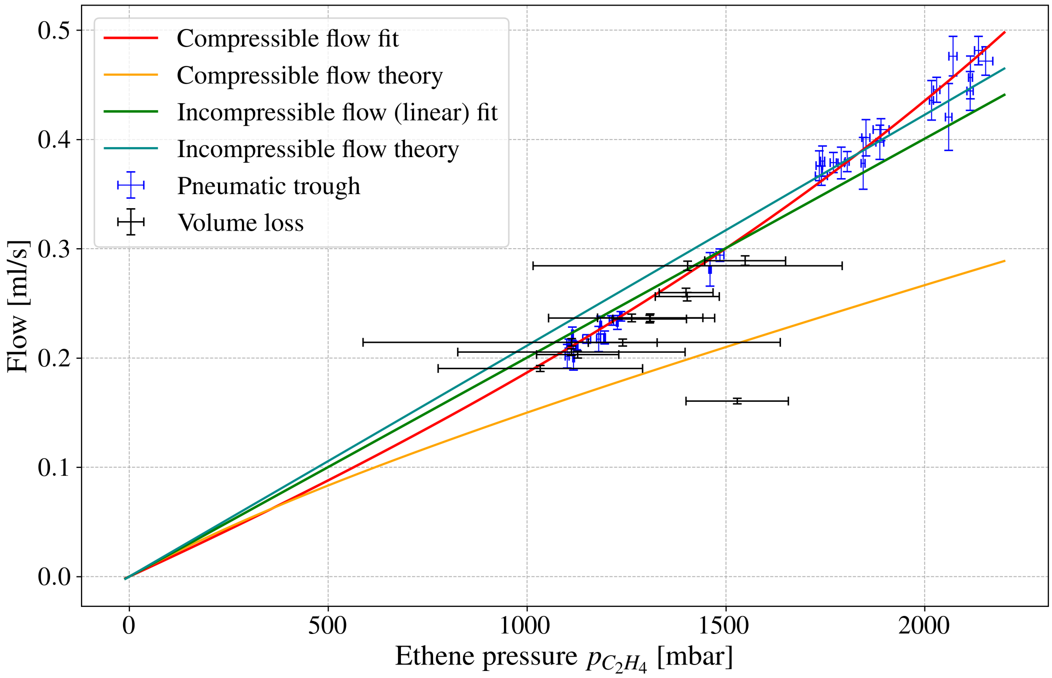

Figure 15: Measured C_2H_4 flow as a function of $p_{\mathrm{C_2H_4}}$. Two different techniques are used to determine the C_2H_4 flow experimentally (pneumatic trough measurements and volume loss in the Minican). To the data points the expected theoretical dependence is fitted, and the fully theoretically calculated dependence both for compressible and incompressible flow is plotted. The theoretical and experimental incompressible flow fit well to the data and to each other. The compressible flow fit describes the data the best but strongly deviates from the theoretically expected dependence.

data. However, this is likely coincidental rather than a reflection of the theory accurately describing the data points.

⇒ Fit parameter incompressible:

$$a_{\text{fit}} = (2.004 \pm 0.020) \times 10^{-6}\,\frac{\text{mL}}{\text{Pa s}} \qquad a_{\text{theory}} = 2.11 \times 10^{-6}\,\frac{\text{mL}}{\text{Pa s}} \tag{41}$$

⇒ Fit parameter compressible:

$$a_{\text{fit}} = (8.37 \pm 0.10) \times 10^{-7}\,\frac{\text{mL}}{\text{Pa s}} \qquad a_{\text{theory}} = 1 \times 10^{-6}\,\frac{\text{mL}}{\text{Pa s}} \tag{42}$$

$$b_{\text{fit}} = (-5.32 \pm 0.24) \times 10^{17}\,\text{Pa} \qquad b_{\text{theory}} = 1 \times 10^{5}\,\text{Pa} \tag{43}$$

$$c_{\text{fit}} = (-6.77 \pm 0.01) \times 10^{-12}\,\frac{\text{mL}}{\text{s}} \qquad c_{\text{theory}} = 0\,\frac{\text{mL}}{\text{s}} \tag{44}$$

The discrepancy between observed data and the theoretical description for compressible flow remains unclear, especially when such a model should be applicable. This raises questions about the nature of the flow and the underlying processes. Even though the compressible fit shows significant deviations from the compressible theory, this fit is chosen for further considerations and calculations, this prioritises the empirical observation over theoretical description.

5. Characterisation of the monitor

This section focuses on the characterisation of the CL O_3 monitor. For the characterisation firstly the dark current and its temperature dependence have to be determined. Then the monitor is calibrated and the applicability of conversion factor to calculate the O_3 mixing ratio from the measured signal is examined. The validation of this conversion factor is in particular relevant for the considerations of the measurement uncertainty, together with the contributions arising from the correction of the dark current and the calibration. Finally, the response time of the monitor is determined.

5.1. Dark current correction

An important parameter when working with PMTs is the dark current, which is the measurable signal if no photons hit the photosensitive area of the PMT. Its magnitude is strongly temperature dependent and, since the PMT used here is not temperature stabilised, the dark current has to be corrected. In the following, we show that this correction is feasible and only introduces a small uncertainty of less than 1 ppb.

The dark current is caused by indispensable thermionic emission of electrons (also known as thermal electron emission), ohmic leakage, field emissions and radioactivity (Photonis, n.d.). The magnitude of these effects depends on material characteristics and on temperature (Baicker, 1960). Without temperature stabilisation, the temperature of the PMT adjusts to the temperature inside the monitor, which increases during the course of a measurement since some of the electrical components (e.g. Raspberry Pi, Step-down converter and the pump) produce heat. The temperature of the PMT is recorded using a PT1000 temperature sensor which is glued to the surface of the PMT housing. To thermally isolate it from the environment styrofoam is placed on top of it. Assuming a temperature range of 5 °C to 45 °C, the dark current is dominated by thermionic emissions. These thermionic emissions vary strongly with temperature and are usually described for a PMT with current output I by the Richardson law:

$$I = AT^2 \exp\left(-\frac{W_e}{k_B T}\right) \tag{45}$$

$$\text{with } A = \frac{4\pi m k_B^2 e}{h^3} \approx 1 \times 10^6 \, \tfrac{\mathrm{A\,K^2}}{\mathrm{m^2}} \tag{46}$$

Here, a PMT with voltage output is used, therefore the Richardson law has to be modified in the following way to describe a voltage output,

$$V = R \cdot AT^2 \exp\left(-\frac{W_e}{k_B T}\right) \tag{47}$$

$$\text{with } R = 10^7\,\Omega \text{ (as given by the PMT data sheet, see Appendix C.2)} \tag{48}$$

$$\Rightarrow R \cdot A \approx 1 \times 10^{13} \, \tfrac{\mathrm{A\,K^2}}{\mathrm{m^2}} \tag{49}$$

For a typical bialkali cathode the Richardson law predicts roughly a ten-fold increase for a 15 °C temperature rise (Photonis, n.d., page 16). It is therefore important to record the temperature of the PMT to account for changes in the amplitude of the dark current. As the strength of the dark current and also of the thermionic emissions is characterised by the material used it is best to determine the temperature dependence experimentally.

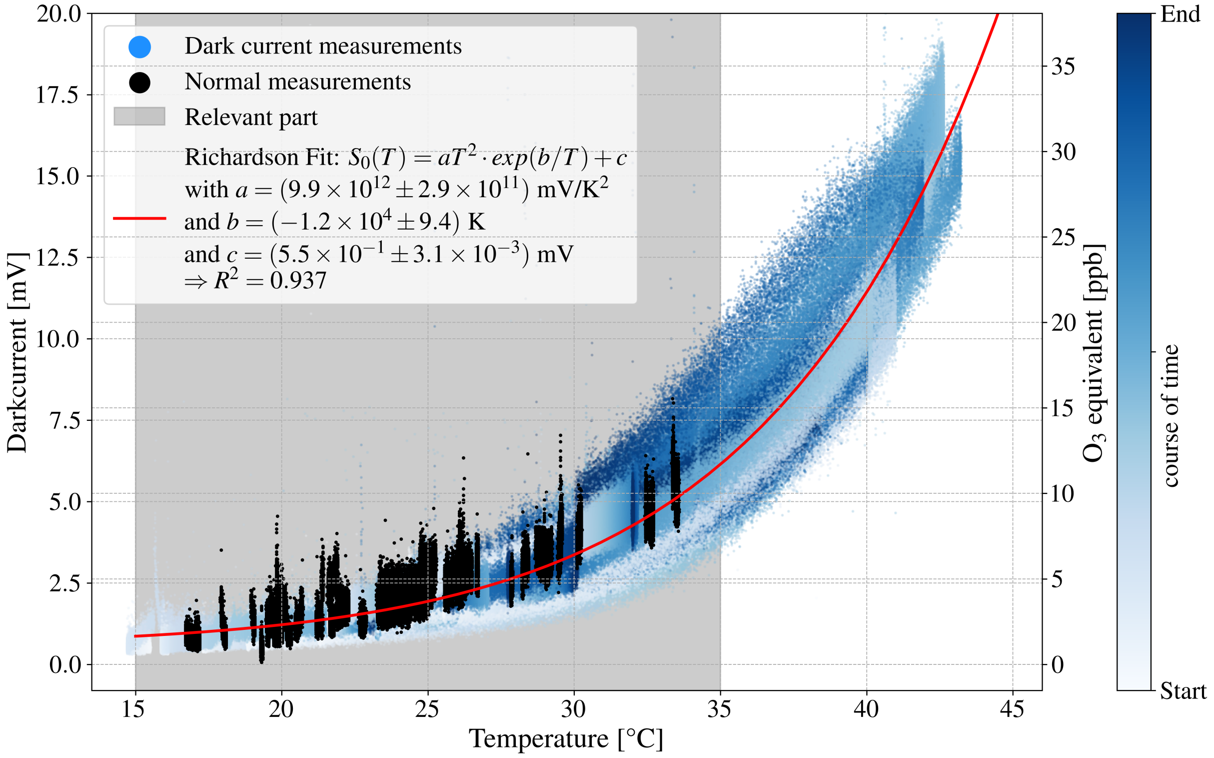

Figure 16: Temperature dependence of the dark current. The blue data points are measurements solely dedicated to determine the dark current. The darker blue the colour the later in the measurement the data point is recorded. The black points represent 'normal' O_3 measurements during which also dark current periods were recorded. To the data a Richardson and an exponential function are fitted. The Richardson fit is then used to correct the temperature dependence of the dark current.

Several measurement are conducted and compiled in Fig. 16. Some record the 'natural' temperature rise during a measurement while during others ambient temperature was actively changed (increasing the temperature by placing the monitor in an oven, decreasing the temperature by taking it out of the oven). Additionally, periods from other measurements during which the dark current was measured (by using a scrubber or zero gas of the O_3 generator) are also included here. These data points are crucial as they represent the dark current during actual measurements, to which the dark current correction is applied later on.

The data reveals a significant increase in dark current with temperature, particularly noticeable from a temperature of 30 °C onwards.

The data points from 'normal' measurements, typically show higher values than those during dark current experiments.

Interestingly, the data exhibits a hysteresis effect, indicating that the direction of temperature change (increase or decrease) affects the dark current. Consequently, it is not possible to unambiguously associate the measured temperature at the PMT with a specific value of the dark current. This effect becomes more pronounced at higher temperatures, starting roughly from 35 °C. This temperature regime is usually not reached during measurements.

This observed hysteresis most likely arises because the temperature measurement at the housing of the PMT is measured does not correspond to the temperature that determines the dark current. The temperature relevant for the dark current is probably mainly de-

pendent on the temperature of the photo cathode. Notably, the time constant with which these two different temperatures adapt to changes differs.
This presents a challenge when trying to correct for the dark current, particularly during rapid changes in ambient temperature, which often lead to rapid changes in the dark current, making the correction difficult. Therefore, such temperature fluctuations should be avoided as best as possible.

In order to correct the dark current to the data the following function (see Eqn. 47) are fitted,

$$S_0(T) = a_1 \cdot T^2 \cdot \exp\left(\frac{b_1}{T}\right) + c_1. \tag{50}$$

The Richardson fit was modified to account for an intercept in order to describes the measured data better. The fit parameters are shown in the graph, Fig. 16. The parameters of the Richardson fit correspond very well to the theoretical values. The temperature needed for a tenfold-increase in the signal can be numerically determined,

$$\Theta_{10} = (19.36 \pm 0.04)\,^{\circ}\mathrm{C}. \tag{51}$$

This corresponds reasonably well to the tenfold-increase temperature of 15 °C given in the literature (Photonis, n.d.).

In order to evaluate the fit and therefore the uncertainty arising from the dark current correction, the histogram of the deviations from the dark current periods of the 'real' measurements to the fit is analysed. It is displayed in Fig. 17. Even it is evident from the histogram that the determined fit cannot completely correct the dark current (mean of the distribution $S_{0,\mathrm{mean}}$ is larger than zero and the distribution is not symmetrical), the dark current correction is sufficiently accurate. $S_{0,\mathrm{mean}}$ is treated as the uncertainty arising from the dark current correction, leading to a uncertainty of only 1 ppb, as it can be seen in Fig. 17.

To correct some of the problems of the dark current correction an easy practical solution is to subtract $S_{0,\mathrm{mean}}$ from each measurement,

$$S_{\text{no dark current}} = S - S_0(T) - S_{0,\mathrm{mean}}, \tag{52}$$

where S is the measured signal, the output signal of the PMT given in mV. The dark current periods with this correction are shown in Fig. 18. For comparison, the solely temperature corrected signal is also shown (black data points). While the correction improves when the mean values are additionally subtracted, there are still deviations from zero, which are most likely related to the hysteresis effect.

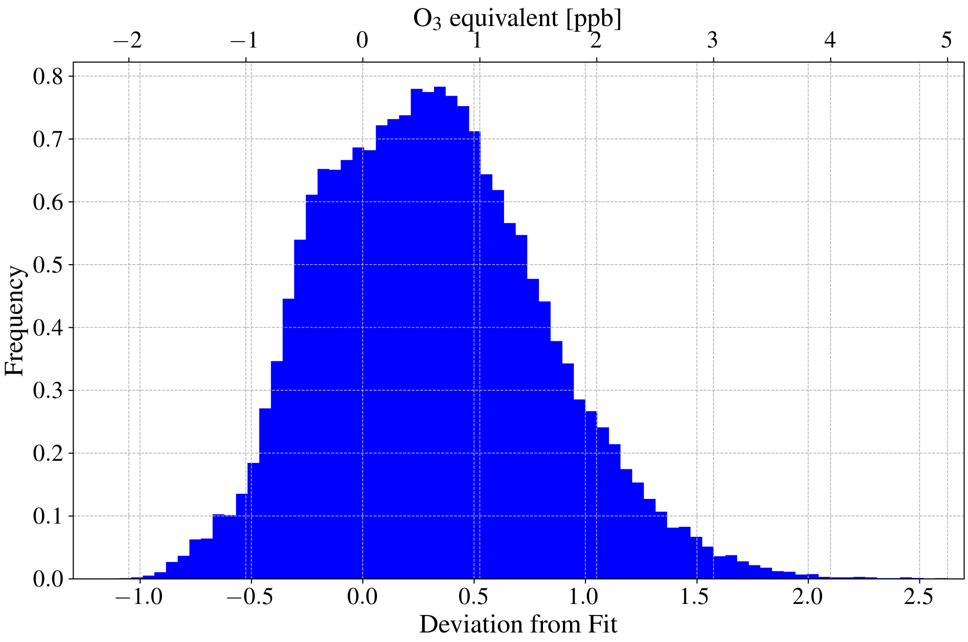

Figure 17: Histogram of the deviation from the 'normal' measurements to the fit. The distribution is not symmetric and shows a positive mean, indicating that the used function cannot properly describe the data.

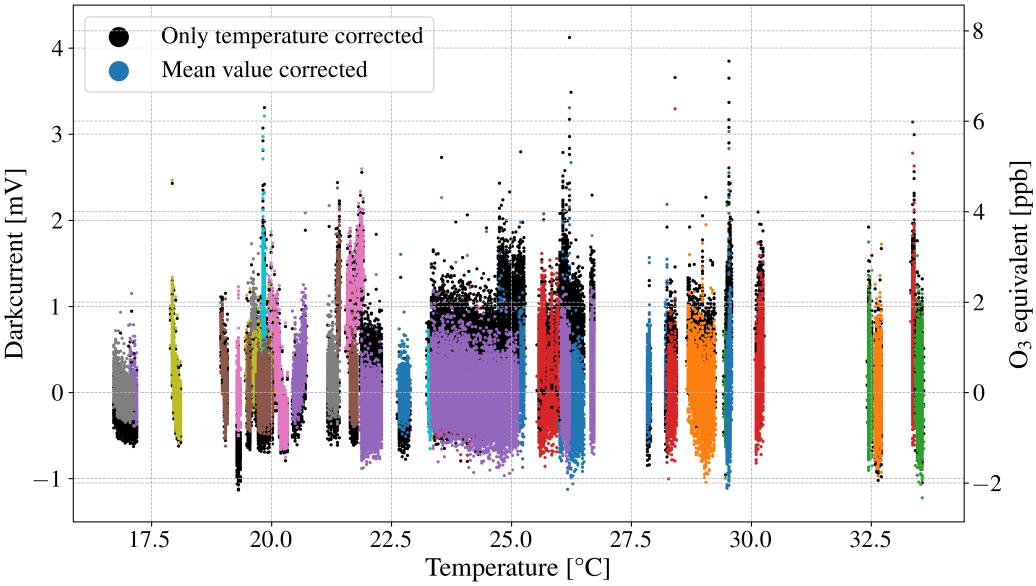

Figure 18: Corrected dark current periods once only correcting the temperature dependence of the dark current (black) and once correction additionally with the mean of the dark current after the temperature correction (colourful). The different colours indicate different measurements.

5.2. Calibration

Since the CL method is not a direct measurement technique, the mixing ratio of O_3 cannot be calculated directly from the measured signal with the theoretical considerations in Sec. 3.2.3 and calibration is needed. The calibration factor which is needed to convert the measured signal to an O_3 mixing ratio is dependent on many factors that cannot be determined theoretically, such as the collection efficiency of the PMT or the quantum efficiency of the reaction. Taking the considerations about the dark current into account (see previous Sec. 5.1), the following relationship can be determined from the theoretical description (see Eqn. 31),

$$\gamma = a_{\text{calibration}} \cdot [S - S_0(T) - S_{0,\text{mean}}] \tag{53}$$

$$\Rightarrow x_{\mathrm{O}_3} = a_{\text{calibration}} \cdot c_{\text{con}}(p_{\mathrm{C_2H_4}}, p, T) \cdot [S - S_0(T) - S_{0,\text{mean}}] \tag{54}$$

$$\Rightarrow x_{\mathrm{O}_3} = a_{\text{calibration}} \cdot S_{\text{con}}, \tag{55}$$

where S is the measured signal, $S_0(T)$ the temperature dependent dark current, and $S_{0,\text{mean}}$ the mean fit residuals from the dark current temperature correction, c_{con} the theoretically determined conversion factor (see Sec. 3.2.2) and $a_{\text{calibration}}$ the calibration constant. S_{con} is the dark current corrected signal multiplied with the conversion factor, and is denoted as the converted signal (given in $\frac{\text{mV K s}}{\text{Pa mL}}$).
Here, no calibration offset is considered as any potential offset in the data is taken care off by applying the dark current correction.

The CL O_3 monitor is calibrated using an O_3 generator, primarily the Ozone Calibration Source Model 306 by 2B Technologies. It is a portable O_3 generator and can provide O_3 in the range ot 0 to 1000 ppb. The other O_3 generator used is an ANYSCO type SYCOS KT-O_3/SO_2 test gas generator and can provide 0 and 150 ppb of O_3.

To calibrate the monitor several calibration measurements with varying O_3 mixing ratios in different sequences are made. Then the dark current corrected and the converted signal are calculated by subtracting the dark current ($S_0(T)$ and $S_{0,\text{mean}}$), and multiplying with c_{con}, respectively. Comparing these two signals allows to asses the influence of the conversion factor c_{con} as well as examine its validity. For the periods of constant O_3, the converted and the dark current corrected signal are averaged and plotted against the sampled O_3 mixing ratios as shown in Fig. 19. A linear fit is performed, its fit parameters are then used for the calibration. The colours indicate the mean C_2H_4 pressure $p_{\mathrm{C_2H_4}}$ during the respective part in the measurement. Additional calibration plots where the data points are colour-coded according to ambient pressure and temperature can be found in Appendix A.1.

It can be seen that without the conversion the measured values for the same O_3 mixing ratio vary significantly. In particular, the measured values are smaller the lower the back pressure is. This is expected, as a lower C_2H_4 pressure leads to a smaller C_2H_4 flow which in turn leads to a smaller signal (see Sec. 3.2.2).
These significant deviations in the calibration measurements can be resolved when applying the conversion factor.
When considering the influence of the other ambient parameters in the conversion it becomes clear that $p_{\mathrm{C_2H_4}}$ has the strongest influence (see Appendix A.1). This is also what is expected from the theoretical consideration in Sec. 3.2.3.

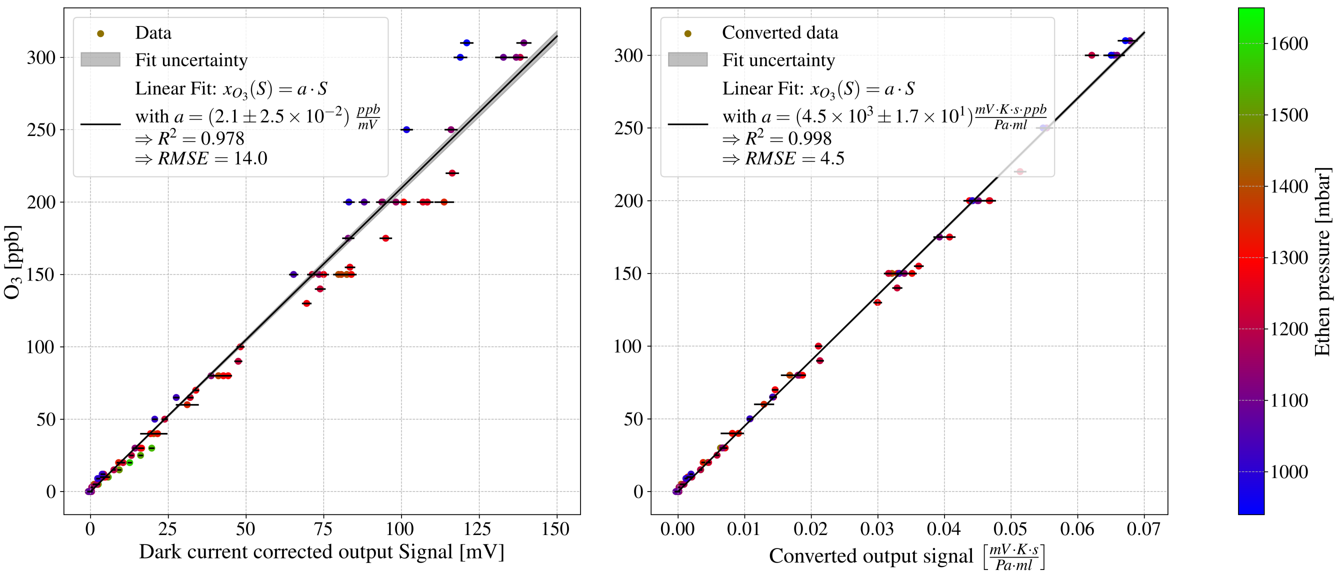

Figure 19: Calibration plot of the CL O_3 monitor. To obtain the data points, the signal is averaged over the periods of constant O_3 mixing ratios, the uncertainty is given by the standard deviation. The colour of the data points indicates the respective C_2H_4 pressure $p_{C_2H_4}$. On the left side, the calibration plot with the dark current corrected signal is shown. Strong deviations from the calibration fit can be seen in the data points. After the conversion, on the right side, the calibration curve fits the data points significantly better. For both cases the calibration fit with the fit parameters as well as root mean squared error (RSME) is shown.

5.3. Validation of the theoretical signal conversion

The calibration measurements show that the theoretical conversion $c_{\mathrm{con}}(p_{C_2H_4}, p, T)$ yields reasonable results, see Fig. 19. This is a first indication that the theoretically calculated signal is a good description of reality. In order to further validate the applicability of the theoretical description, the calibration measurements can be used further and also additional measurements are helpful where one parameter is changed while keeping the other parameters constant. For both techniques, calculating a relative signal from the measured signal allows to compare the experimental results with the theoretical results presented in Sec. 3.2.3 and allows to estimate the deviations between theory and experiment. Notably, these deviations are approximately only 4%, highlighting the applicability of the theory.

5.3.1. Calibration

To evaluate whether the theoretical description is able to describe the data, the periods with constant O_3 mixing ratio during calibration measurements can be used. During these periods, the relative signal S_{rel} is derived by dividing the signal with its mean $S_0 = S_{\mathrm{mean}}(T_0, p_0, p_{C_2H_4,0})$. $T_0, p_0, p_{C_2H_4,0}$, are determined by finding the part in the measurement during which the the determined mean S_0 is measured. The values for $T, p, p_{C_2H_4}$ that are recorded during this period are then used as the reference values $T_0, p_0, p_{C_2H_4,0}$.

For the theoretical relative signal γ_{rel}, only the ambient parameters, namely T, T_0 and p,

p_0, along with the C_2H_4 pressure, $p_{C_2H_4}$, $p_{C_2H_4,0}$ have to be considered,

$$S_0 = S_{\text{mean}} \rightarrow \text{determine from this } T_0, p_0, p_{C_2H_4,0} \tag{56}$$

$$\Rightarrow \gamma_0 = \gamma(T_0, p_0, p_{C_2H_4,0}) \tag{57}$$

$$= \frac{(f_{\text{tot}} - f_{C_2H_4}(p_{C_2H_4}))\frac{p}{T} \cdot \left[1 - \exp\left(-k(T) \cdot \frac{f_{C_2H_4}(p_{C_2H_4})}{f_{\text{tot}}} \cdot \frac{p}{k_b T} \cdot \frac{V_{\text{cell}}}{f_{\text{tot}}}\right)\right]}{(f_{\text{tot}} - f_{C_2H_4}(p_{C_2H_4,0}))\frac{p_0}{T_0} \cdot \left[1 - \exp\left(-k(T_0) \cdot \frac{f_{C_2H_4}(p_{C_2H_4,0})}{f_{\text{tot}}} \cdot \frac{p_0}{k_b T_0} \cdot \frac{V_{\text{cell}}}{f_{\text{tot}}}\right)\right]} \tag{58}$$

where (f_{tot} and $f_{C_2H_4}$ represent the total and the C_2H_4 flow respectively. To determine the how well the theory describes the measured signal the deviations between the measured and theoretical relative signal are calculated and then averaged. For this only the absolute values are of interest.

$$S_{\text{rel}} = \frac{S}{S_0} \tag{59}$$

$$\gamma_{\text{rel}} = \frac{\gamma}{\gamma_0} \tag{60}$$

$$\Rightarrow \overline{|S_{\text{rel}} - \gamma_{\text{rel}}|} \approx 0.034 \tag{61}$$

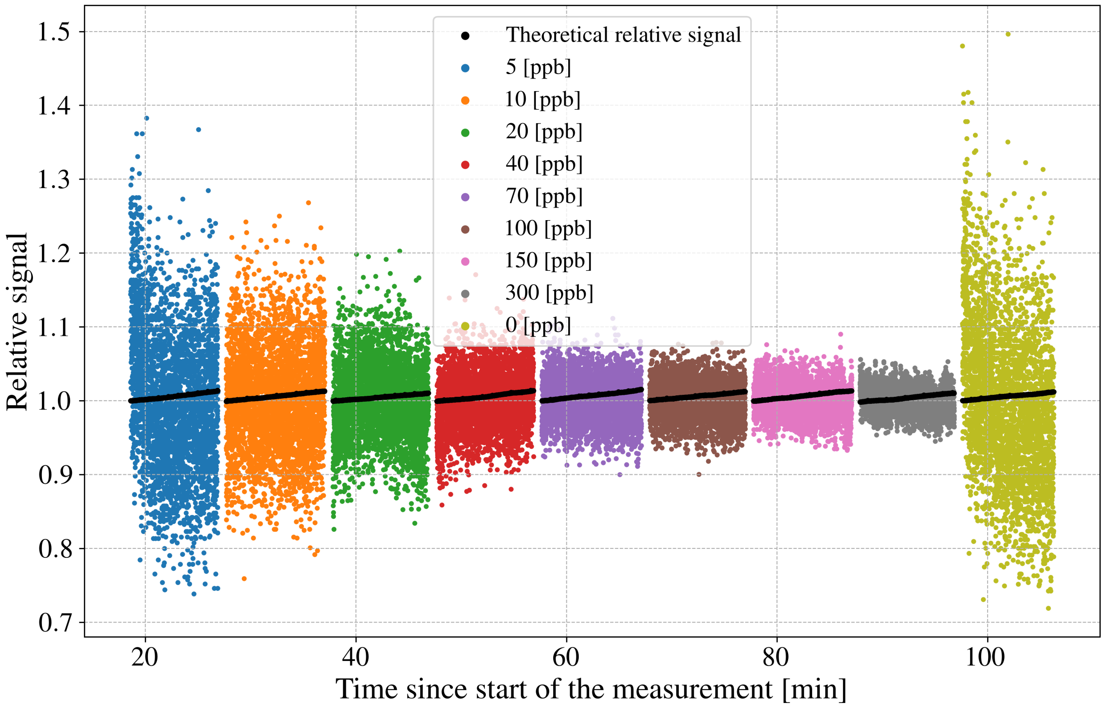

Figure 20: The relative signal for the periods of constant O_3 mixing ratios during a calibration measurement is shown. Also the theoretically determined relative signal (as explained in the text) is shown. The different colours indicate different sampled O_3 mixing ratios. The theoretical signal is able to describe the data well, with a mean deviation of 3.4%. This plot also shows the change in the relative noise of the signal (more details on that can be found in Sec. 5.4).

5.3.2. Changes in ethylene pressure

In this context, measurements were conducted with varying C_2H_4 pressure, while the other parameters (such as O_3 mixing ratio, ambient pressure, and temperature) are not changed. Ambient pressure and temperature are not actively held constant during and in between different measurements. However, it can be assumed that during a single measurement the changes in these parameters can be neglected.

The effect of the changing C_2H_4 pressure on the signal is shown in Fig 21. Here, a constant O_3 mixing ratio of 150 ppb is measured over a period of 2 h. The back pressure changes from around 1525 mbar (neglecting the initial pressure rise) to 1300 mbar which leads to a change in the O_3 signal of around 10 mV (corresponding to 10% decrease).

For all measurements the relative signal is determined by dividing the measured signal by a reference signal at a C_2H_4 pressure of $p_{C_2H_4}$ =1300 mbar. This relative signal is then plotted against the recorded back pressure which can be seen in Fig. 22, blue dots. In some measurements only the naturally occurring pressure decrease over the measurement time is recorded (Fig. 22, dense accumulation of data points at ∼1400 mbar). For others the valve at the C_2H_4 bottle is opened and closed several times to create pressure drops of stronger magnitude (Fig. 22, data points corresponding to lower $p_{C_2H_4}$). These fast drops in pressure are however not representative of pressure changes during O_3 measurements.

In addition, the theoretically calculated relative signal is shown in the graph. This signal is computed by dividing the absolute number of generated photons (calculated from the recorded parameters, $p_{C_2H_4}$, ambient pressure, and temperature) by the reference signal. This reference signal is based on the parameters measured during the time of the experimentally determined reference signal, similar to the procedure previously described in Sec. 5.3.1,

$$S_0 = S(p_{C_2H_4,0}) \rightarrow \text{determine from this } T_0, p_0 \tag{62}$$

$$\Rightarrow \gamma_0 = \gamma(T_0, p_0, p_{C_2H_4,0}). \tag{63}$$

Deviations between the experimental results and the theoretical predictions are particularly evident at small and large values of $p_{C_2H_4}$. These are, however, usually not the C_2H_4 pressure regimes encountered in normal O_3 measurements, the relevant part, 700 mbar to 1900 mbar, is also highlighted in Fig. 22. A notable discrepancy is the offset in the relative signal. A likely reason for this deviation is the observed 'airglow' signal . The 'airglow' signal, is the signal that can be observed even when no C_2H_4 is injected into the measurement cell, for a more detailed description see Sec. 6.
To test this hypothesis, a rudimentary description of the 'airglow' is subtracted from the data. We estimated that the 'airglow' signal contributes approximately 15% of the reference value to the overall signal (see Sec. 6.1). The so adjusted data, presented in Fig. 22 as black dots, aligns more closely with theoretical predictions. This supports the hypothesis that the 'airglow' contributes as a non-constant offset to the 'normal' O_3 signal.

However, for the relevant C_2H_4 pressure regimes, the difference between the measured signal and the signal where the 'airglow' signal is subtracted is not as pronounced.

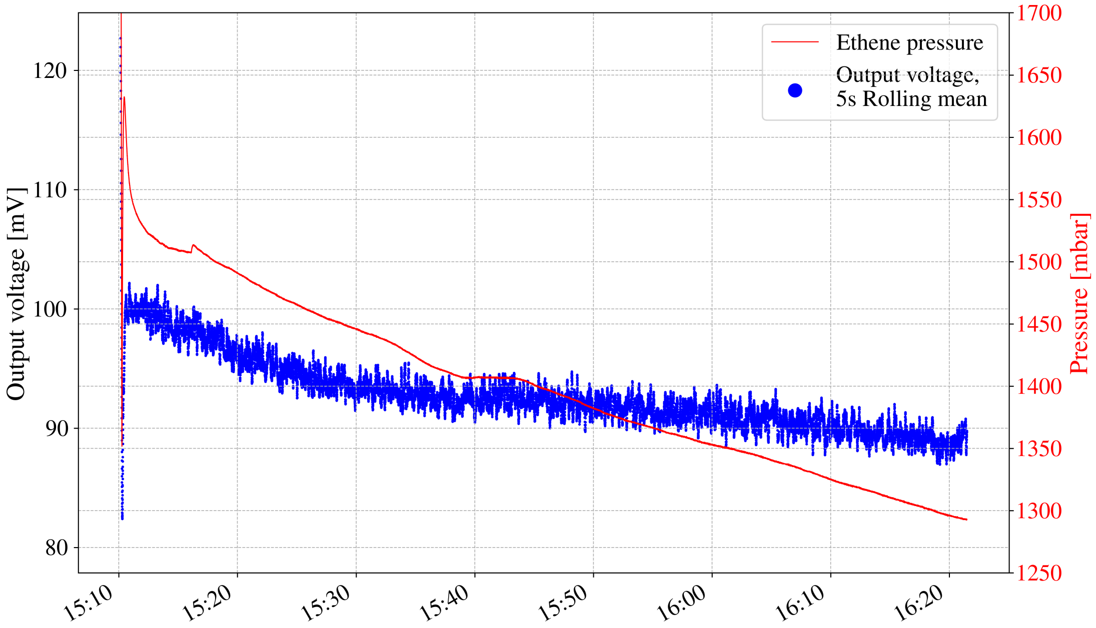

Figure 21: Signal drift for a 150 ppb O_3 signal caused by the drift in the C_2H_4 pressure. To convert the output voltage of the PMT into ppb O_3 equivalent for standard conditions, the output voltage simply has to be multiplied by the factor 2.

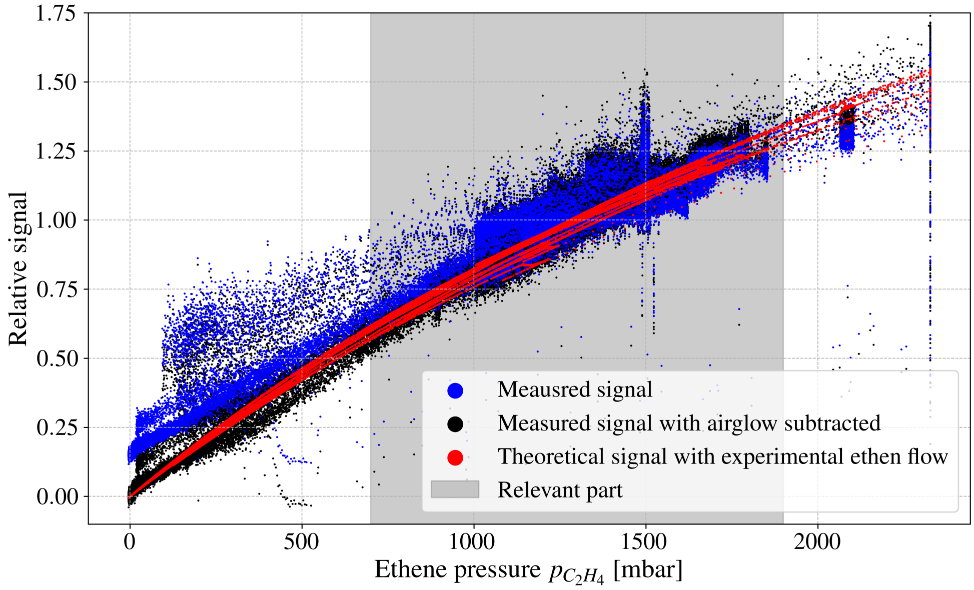

Figure 22: Measured relative signal (signal divided by reference signal at $p_{\mathrm{C_2H_4}} = 1300\,\mathrm{mbar}$) plotted against $p_{\mathrm{C_2H_4}}$ (blue dots). Additionally, the theoretically calculated signal is shown in red. The deviations can be mainly attributed to the 'airglow' signal (see Sec. 6). The black dots represent the measured signal with the 'airglow' signal subtracted. The theoretical description fits well to these data points. However, for the relevant pressure regime (marked in grey) the deviations from the measured data to the theory are around 4%.

In this setup also the deviations between the measured and theoretical relative signal are calculated and then averaged. Here again the absolute deviations are considered. For this only the data in the data points in the as relevant marked pressure regime are considered.

$$\overline{|S_{\text{rel, relevant part}} - \gamma_{\text{rel, relevant part}}|} \approx 0.040 \tag{64}$$

This deviation is slightly increased compared to the deviation obtained from the calibration measurements, where the mean absolute deviation is 3.4%. This difference is however not significant.

5.3.3. Changes in ambient pressure

Additionally, we investigate the impact of changes in ambient pressure on the signal. To achieve this, the O_3 generator is used to maintain a constant O_3 mixing ratio while varying the ambient pressure through varying the altitude. This is done by driving up and down the flanks of Etna. During the measurements, maintaining a constant C_2H_4 pressure is not possible, resulting in the simultaneous variation of the two parameters. Consequently, validating the correction for only changes in ambient pressure becomes somewhat more complex. Here, validation is therefore only conducted by applying the conversion and calibration to the time series. Ideally, by doing so, the measured data should show a constant O_3 mixing ratio over the entire measurement duration.

Three such measurements were conducted, one of them is presented in Fig. 23. The other measurements exhibit similar characteristics and are shown in Appendix A.2.

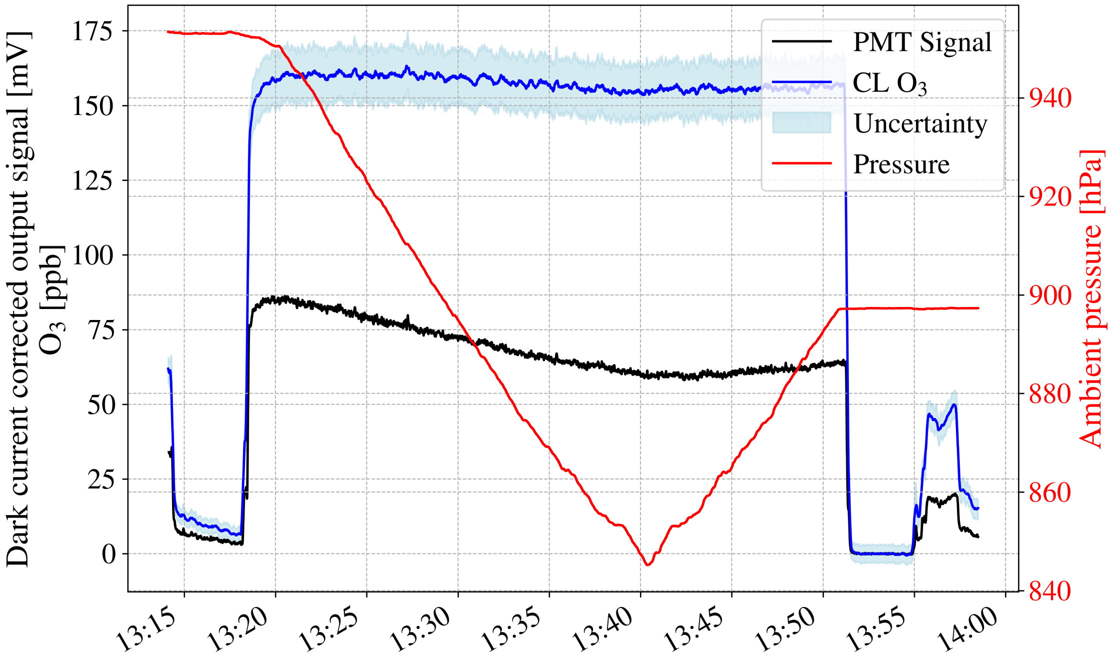

Figure 23: Influence of changing ambient pressure on the signal. Once the PMT signal as it is recorded (black) is shown as well as the calculated O_3 mixing ratio (blue). This shows that the signal indeed changes with the ambient pressure, applying the calibration reduced this dependence. The corresponding ambient pressure is shown in red.

The figure displays both the recorded PMT signal, which does show a pressure dependence as expected, and the calculated O_3 mixing ratio, which shows a considerably reduced pressure dependence.
However, some fluctuations are still evident in the measurements. It is noteworthy that under controlled laboratory conditions in Heidelberg, the calibration measurements did not exhibit such large fluctuations. One explanation for the discrepancy might be that the O_3 generator was operated within the car and powered through the car battery, since the monitor's internal battery was defective. The change in power supply as well as smaller vibrations and bumps during the drive might have influenced the reliability of the O_3 generator.
Despite these uncertainties, the test indicates that the conversion factor yields reasonably accurate results.

5.4. Detection limit and measurement uncertainty

Both the detection limit and the measurement uncertainty are crucial characteristics of any instrument. Following the definition of Gold (2019) the detection limit (also referred to as limit of detection (LoD)) is the 'minimum single result which, with a stated probability, can be distinguished from a suitable blank value' (Gold, 2019, p. 399). Here, the detection limit is determined by the measurement uncertainty of the blank value.

To determine the uncertainty of the mixing ratio of O_3, error propagation is applied. This requires taking the derivative of the O_3 mixing ratio formula with respect to each potential uncertainty source.

$$x_{O_3} = a_{\text{calibration}} \cdot c_{\text{con}}(p_{C_2H_4}, p, T) \cdot (S - S_0(T) - S_{0,\text{mean}}) \tag{65}$$

$$\Delta x_{O_3} = \left\{ \left(\frac{\partial x_{O_3}}{\partial S} \Delta S \right)^2 + \left(\frac{\partial x_{O_3}}{\partial S_0} \Delta S_0 \right)^2 + \left(\frac{\partial x_{O_3}}{\partial c_{\text{con}}} \Delta c_{\text{con}} \right)^2 \right. \tag{66}$$

$$\left. + \left(\frac{\partial x_{O_3}}{\partial a_{\text{calib}}} \Delta a_{\text{calib}} \right)^2 \right\}^{1/2} \tag{67}$$

$$\Rightarrow \frac{\partial x_{O_3}}{\partial S} = -\frac{\partial x_{O_3}}{\partial S_0(T)} = a_{\text{calibration}} \cdot c_{\text{con}}(p_{C_2H_4}, p, T) \tag{68}$$

$$\Rightarrow \frac{\partial x_{O_3}}{\partial c_{\text{con}}} = a_{\text{calibration}} \cdot (S - S_0(T) - S_{0,\text{mean}}) \tag{69}$$

$$\Rightarrow \frac{\partial x_{O_3}}{\partial a_{\text{calib}}} = c_{\text{con}}(p_{C_2H_4}, p, T) \cdot (S - S_0(T) - S_{0,\text{mean}}) \tag{70}$$

To assess the uncertainty associated with the signal itself ΔS, the standard deviation of the measured signal is determined during periods of constant O_3. When considering the calibration measurements, we see that both the absolute and the relative noise increase for increasing O_3 mixing ratios (as can be seen in Fig. 20). In order to determine the standard deviation in dependence of the measured signal, these two quantities are plotted against each other. This is presented in Fig. 24. To the data a logarithmic function is fitted, from which the uncertainty in dependence of the measured signal can be determined,

$$\Delta S = \sigma_S = a \cdot \ln(b \cdot x + c). \tag{71}$$

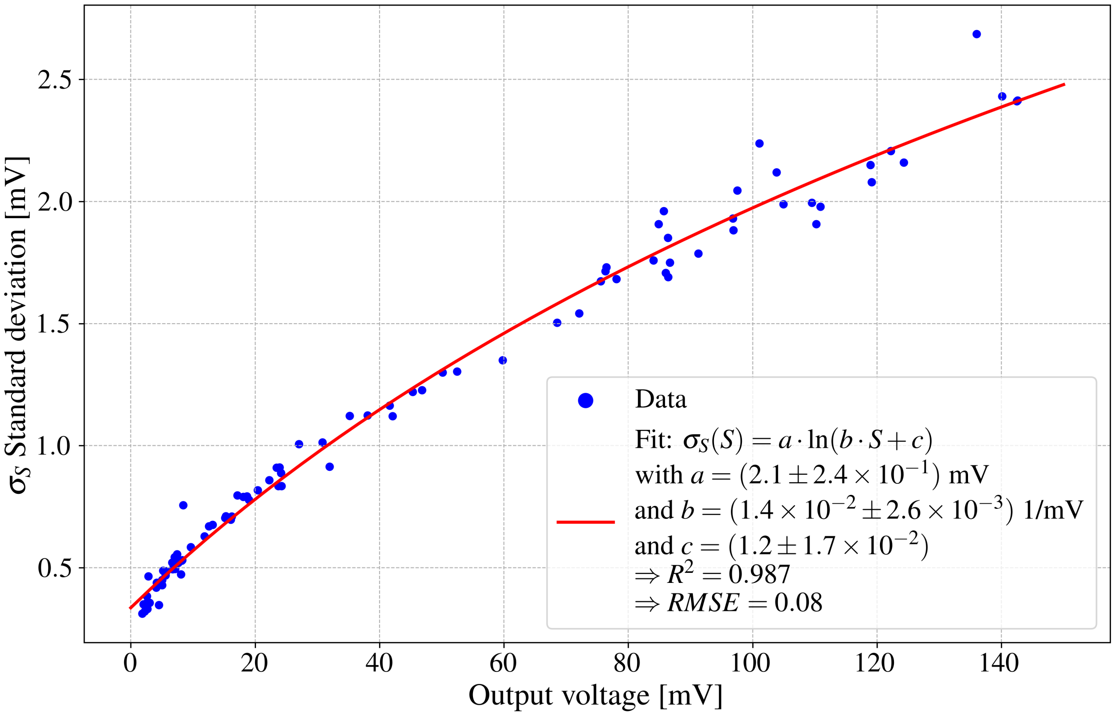

Figure 24: Standard deviation of the signal plotted against the signal. A logarithmic function is fitted to the data, which has been empirically found to fit the data the best. This enables to determine the uncertainty for a specific values of the signal.

ΔS_0 represents the uncertainty arising from correcting the temperature dependence of the dark current. This correction is based on the fit to the measured dark current, but the deviation of data from the fit tends to be more significant than the fit parameter uncertainties indicate. Therefore, rather the mean deviation from the considered measurement to the fit is used as uncertainty,

$$\Delta S_0 = \overline{(S - S_0(T))} \approx 0.5\,\mathrm{mV}. \tag{72}$$

The uncertainty arising from the calibration is quantified by the uncertainty of the fit parameter $\Delta a_{\mathrm{calib}} = 24\,\frac{\mathrm{hPa\,mL\,s}}{\mathrm{mV\,K}}$.

Determining the uncertainty associated with the conversion of the signal is not as straight forward as the other contributions. A direct comparison between theoretical predictions and experimental results is challenging since the precise number of emitted photons, or those reaching the PMT, is not possible. Additionally to a possible systematic error in the theory, the conversion factor is calculated using the measured variables like pressure p, temperature T, and C_2H_4 pressure $p_{C_2H_4}$, introducing another layer of uncertainty as all of these measurements carry uncertainties. Moreover, the dependence of the conversion factor on $p_{C_2H_4}$ is an indirect one, as the direct influencing parameter is the C_2H_4 flow $f_{C_2H_4}$. The relationship between $f_{C_2H_4}$ and $p_{C_2H_4}$ is determined experimentally and also carries significant uncertainties (see Sec. 4.3).

However, from the comparison of the theoretically calculated relative signal with the experimental data (Sec. 5.3), we have seen that the data shows a mean deviation to the theoretical description of about 4%. This relative deviation serves as the uncertainty attributed to signal conversion.

With this we arrive at the following error analysis, for a representative signal of $S = 20\,\mathrm{mV}$, which corresponds to an O_3 mixing ratio of ∼40 ppb under standard conditions:

$$\frac{\partial x_{O_3}}{\partial S}\Delta S = a_{\mathrm{calibration}} \cdot c_{\mathrm{con}}(p_{C_2H_4}, p, T) \cdot \sigma_S \tag{73}$$

$$\approx 0.05 \cdot x_{O_3} \tag{74}$$

$$\frac{\partial x_{O_3}}{\partial S_0(T)}\Delta S_0 = a_{\mathrm{calibration}} \cdot c_{\mathrm{con}}(p_{C_2H_4}, p, T) \cdot \overline{(S - S_0(T))} \tag{75}$$

$$\approx 0.025 \cdot x_{O_3} \tag{76}$$

$$\frac{\partial x_{O_3}}{\partial c_{\mathrm{con}}}\Delta c_{\mathrm{con}} \approx 0.04 \cdot x_{O_3} \tag{77}$$

$$\frac{\partial x_{O_3}}{\partial a_{\mathrm{calib}}}\Delta a_{\mathrm{calib}} = c_{\mathrm{con}}(p_{C_2H_4}, p, T) \cdot (S - S_0(T) - S_{0,\mathrm{mean}}) \cdot \Delta a_{\mathrm{calib}} = \frac{\Delta a_{\mathrm{calib}}}{a_{\mathrm{calib}}} \cdot x_{O_3} \tag{78}$$

$$= \frac{24}{4555} \cdot x_{O_3} = 0.005 \cdot x_{O_3} \tag{79}$$

$$\Rightarrow \Delta x_{O_3} \approx \left(0.05^2 + 0.025^2 + 0.04^2 + 0.005^2\right)^{1/2} \cdot x_{O_3} \approx 0.07 \cdot x_{O_3} \tag{80}$$

Using $\sigma_{S,0} \approx 0.4\,\mathrm{mV}$ and assuming that after the dark current correction the dark current signal actually is zero, the detection limit can be approximated by:

$$\frac{\partial x_{O_3}}{\partial S}\Delta S = a_{\mathrm{calibration}} \cdot c_{\mathrm{con}}(p_{C_2H_4}, p, T) \cdot \sigma_{S,0} \tag{81}$$

$$\approx 0.8\,\mathrm{ppb} \tag{82}$$

$$\frac{\partial x_{O_3}}{\partial S_0(T)}\Delta S_0 = a_{\mathrm{calibration}} \cdot c_{\mathrm{con}}(p_{C_2H_4}, p, T) \cdot \overline{(S - S_0(T))} \tag{83}$$

$$\approx 1\,\mathrm{ppb} \tag{84}$$

$$\Rightarrow \Delta x_{O_3,0} \approx \left(0.8^2 + 1^2\right)^{1/2}\mathrm{ppb} \approx 1.3\,\mathrm{ppb} \tag{85}$$

It has to be noted, that this is the detection limit under ideal conditions. For measurements during which the dark current corrections are unable to fully account for the dark current, there are also contribution from the other two uncertainty sources.

Looking at the detection limit for zero-value measurements for some exemplary measurements (measurements used for the determination of the dark current correction see Fig. 16, or the drone measurement at Kleiner Feldberg, Sec. 7.2, Fig. 33) we see that this value accurately describes the detection limit. During these measurements the detection limit ranges between 1 ppb and 1.5 ppb.

5.5. Response time

In this section the response time of the monitor is determined. First, the theoretical description is considered and then compared to the experimentally determined response time.

The theoretical response time (also known as the flushing time) of the monitor can be estimated by dividing the volume of reaction chamber V_{chamber} and the volume of the hose in front of the chamber by the flow rate of the pump f_{tot},

$$t_{\text{theo}} = \frac{V_{\text{tot}}}{f_{\text{tot}}} = \frac{V_{\text{hose}} + V_{\text{chamber}}}{f_{\text{tot}}} = \frac{\pi \cdot r_{\text{hose}}^2 \cdot l_{\text{hose}} + V_{\text{chamber}}}{f_{\text{tot}}} = 1.9\,\text{s}, \tag{86}$$

where $V_{\text{chamber}} = 20\,\text{mL}$, $f_{\text{tot}} = 21\,\frac{\text{mL}}{\text{s}}$, $r_{\text{hose}} = 4\,\text{mm}$ is the inner radius, $l_{\text{hose}} = (40 \pm 4)\,\text{cm}$ the length of the hose. When assuming plug flow conditions, for which no mixing happens and the flow is assumed to be linear, this describes the time needed to replace 100% of the volume. When however perfect mixing is assumed this time describes the time for which 63% ($0.63 \approx 1 - \frac{1}{e}$) of the volume are exchanged. In this setting, the incoming air mixes uniformly with the existing fluid, and the exchange of the existing air happens in an exponential fashion. Usually, the response time is defined as the time it takes for the signal to reach ~63%, therefore under plug flow conditions the response time has to be adapted,

$$\tau_{\text{theo,plug}} = \tau_{\text{theo}} \cdot 0.63 = 1.2\,\text{s} \tag{87}$$

$$\tau_{\text{theo,mixing}} = \tau_{\text{theo}} = 1.9\,\text{s} \tag{88}$$

In the setup of the monitor, it is most likely that the experimental response time lies closer to $\tau_{\text{theo},mixing}$ since the exchange of the reaction chamber volume most likely happens under mixing.

In order to determine the response time of the monitor experimentally, step changes in the O_3 mixing ratios are of interest. However, measured step changes produced by the O_3 generator are determined by the combination of the response time of the O_3 monitor and the O_3 generator. As the generator has a response time of 10 s (given by the data sheet) and the O_3 monitor an expected response time of 1.2 s, the O_3 monitors response time cannot be determined using theses step changes. To circumvent the generator's response time, one can produce a consistent O_3 mixing ratio using the generator, but without attaching the hose to the monitor. Once a stable mixing ratio is achieved, the hose can be swiftly connected to the monitor. The step change recorded in this manner should reflect the response time of the O_3 monitor.

To these increasing and decreasing step changes these exponential functions are fitted, respectively,

$$f_{\text{incr}}(t) = a \cdot \left(1 - \exp\left(-\frac{(t-c)}{b}\right)\right) + d \tag{89}$$

$$f_{\text{decr}}(t) = a \cdot \exp\left(-\frac{(t-c)}{b}\right) + d \tag{90}$$

where the fit parameter b is the response time of the monitor.

In total 3 measurements with a total of 32 step changes were used. To get a good measure of the monitors response time the obtained values from the different fits are averaged. As not all fits give a good representation of reality only fits with an R^2 larger than 0.9 are used, resulting in 25 fits used in total, 8 for increasing and 17 for decreasing step changes. The averaged time constant for decreases is $\tau_{\text{exp, decr},1/e} = 1.93 \pm 0.03 \pm 0.04\,\text{s}$, for increases $\tau_{\text{exp, incr},1/e} = 2.13 \pm 0.06 \pm 0.05\,\text{s}$. where the first uncertainty is the statistical uncertainty given by the standard deviation of the averaged fit parameters, the second is the uncertainty associated with the fits. When assuming that both increase and decrease display the same characteristics, the experimental response time of the monitor is given by $\tau_{\text{exp},1/e} = 2.00 \pm 0.04 \pm 0.04\,\text{s}$.

Comparing the experimental value to the two theoretically determined response times we see indeed that the conditions in this setup align very well with the assumptions of perfect mixing during the exchange of the volume. $\tau_{\text{exp},1/e}$ aligns with $\tau_{\text{theo},mixing} = 1.9\,\text{s}$ within 2σ.

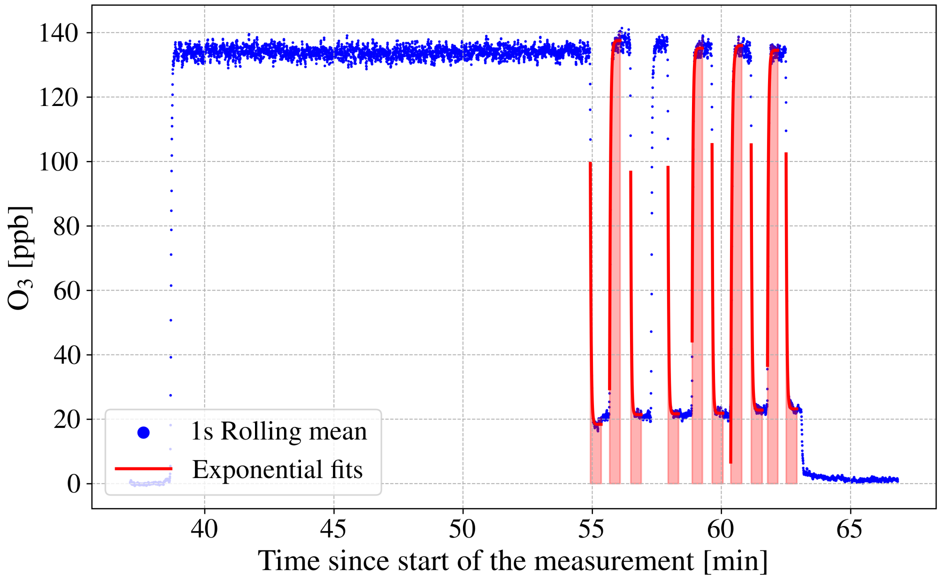

Figure 25: Time series of an O_3 measurement that is used to determine the response time of the monitor. For this a stable O_3 mixing ratio is produced with the O_3 generator and the the hose is connected to the monitor. The step changes are automatically detected and exponential increases or decreases are fitted to the data. Only the fits with a R^2 value larger than 0.6 are shown here, these are also the fits used to determine the response time of the monitor.

6. ‘Glowing of ambient air’

Even when no C_2H_4 is used a signal well above the detection limit can be measured for some configurations. A signal can be measured when an O_3 generator is used or simply when ambient air from the outside is sampled. Measuring indoor air however, does not produce this signal. For lack of a better term this signal will be referred to ‘glowing of ambient air’ or ‘airglow’.
In the following section, this signal is examined in a series of measurements, in order to better understand it.

This phenomenon already occurred during the characterisation of the first prototype of the CL O_3 monitor (Rüth, 2021). The conclusions from the measurements without C_2H_4 done there are the following:

- Signal is (somewhat) correlated with O_3 measurements.
- Measurements during the day and during the evening without sunlight do not show significant deviations.
- Closing the window during the measurement leads to a decrease in the signal (similar to that of O_3) with time constants of around 15-20 min (in simultaneous O_3 measurement the time constant was 20-30 min).
- Measurements using a O_3 generator were done, the signal being around 20% of the signal when C_2H_4 was used.
  ⇒ Whether the cause of these signals is the same could not be determined.

It is believed that the signal could have two plausible causes:

1. The reaction, $O_3 + \mathrm{Y} \longrightarrow \text{products}$,
   is responsible for the signal. This is not far-fetched as reactions with O_3 are known to often produce CL.
2. The reaction, $\mathrm{X} + \mathrm{Y} \longrightarrow \text{products}$,
   causes the signal.

Here, X and Y are unknown molecules.
In order to better understand the nature and origin of this signal several experiments have been conducted.

6.1. Calibration of the ‘airglow’ signal

The initial step involved analysing the signal using an O_3 generator. This enables to determine the monitor’s response to known and variable O_3 mixing ratios. Fig. 26 illustrates a measurement obtained by using the O_3 generator with no C_2H_4 injected into the measurement cell.
The correlation between the sampled O_3 mixing ratio and the recorded signal is shown in Fig. 27. Here, also another ‘airglow’ calibration measurement is included. Additionally, also measurements during which both the ‘airglow’ signal and the O_3 signal are recorded with the CL monitor are included. To obtain the data points the last 200 data points of the ‘airglow’ signal before the C_2H_4 Minican is opened are averaged and compared to the first 200 data points of the O_3 signal. The same procedure is applied to the the end of the O_3 measurement period and the beginning of the ‘airglow’ measurement period.

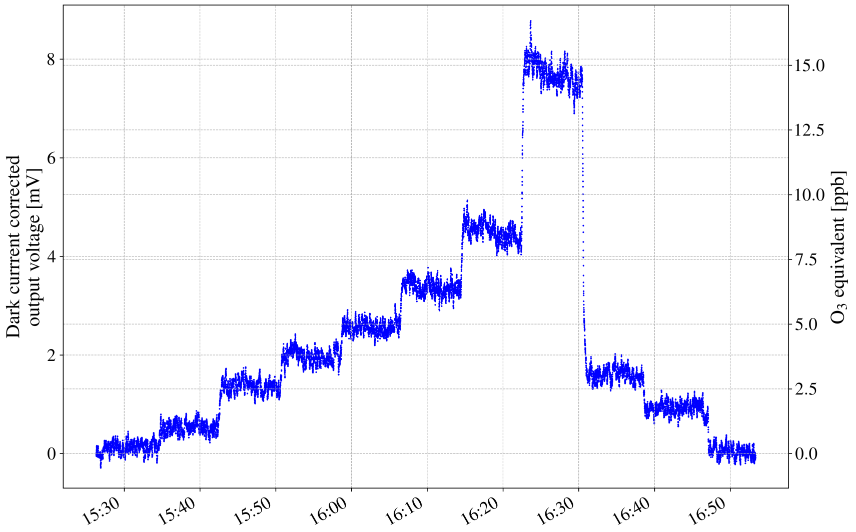

Figure 26: Calibration measurement of the ‘airglow’ signal. For this the O$_3$ generator is used. The ‘airglow’ signal clearly follows the sampled O$_3$ mixing ratio.

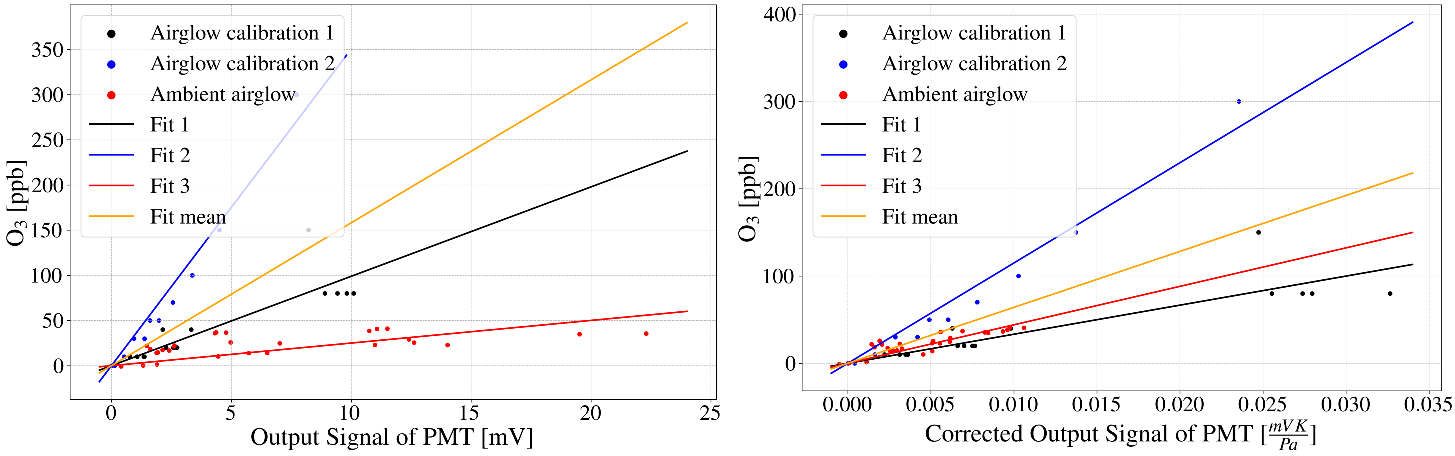

(a) Calibration plot for the ‘airglow’ signal. Periods of constant O$_3$ mixing ratio are averaged and the corresponding output signal of the PMT is plotted against the O$_3$ mixing ratio. Strong deviations between different measurements are evident.

(b) Calibration plot for the ‘airglow’ signal using the corrected signal (multiplying with $\frac{T}{p}$). Although not all deviations can be fully compensated for, they are significantly improved.

Figure 27: Calibration plot of the ‘airglow’ signal. For this plot the calibration measurements are used. Additionally, measurements during which both ‘airglow’ and O$_3$ by injecting C$_2$H$_4$ into the measurement cell are considered. The measured O$_3$ value shortly after opening the valve (or shortly before closing) is compared to the measured ‘airglow’ signal.

Fig. 27 shows that the ‘airglow’ signal is indeed to some variable extent correlated with the O$_3$ mixing ratio. However, the output voltage of the PMT that is associated with the same O$_3$ mixing ratio is not stable between different measurements. The variations are as large, that during one measurement 150 ppb and during another one 25 ppb of O$_3$ produce the same output voltage of around $\sim$5 mV. To each measurement a linear function is fitted. From these fits we can see that the ‘airglow’ signal ranges from around 6% to around 80% of the ‘normal’ signal (signal when injecting C$_2$H$_4$). Averaging the fit parameters of the 3 fits shows that the mean 'airglow' signal corresponds to about 13% of the 'normal' signal. Why these deviations between different measurements are visible is not known. One idea is that parts of these changes might be attributable to changes in the ambient parameters such as the temperature and the ambient pressure, as these change the concentration of the components involved, similarly to the conversion of the O_3 signal to O_3 mixing ratio. Applying a correction factor that is proportional to T and inversely proportional to p reduces the deviations but not to a desirable level. The discrepancies might be associated with the second unknown reactant (provided that the measured signal is in some form related to O_3) and in which concentration this reactant is available. However, if the signal were occasionally constrained by the availability of this second reactant, it should plateau rather than increase further with rising O_3 levels.

As these discrepancies between different 'airglow' calibrations cannot be explained no generally applicable factor to convert the measured signal to ppb O_3 equivalent is found. Nonetheless, a calibration factor is determined by fitting a linear function to the corrected data points of each measurement and then averaging the obtained fit parameters. All four of these linear fits are shown in Fig. 27b. This mean conversion factor for the 'airglow' signal is then later applied to the 'airglow' measurements.

6.2. Comparative measurements of the 'airglow'

Measurements were carried out during which both the 'glowing air' and O_3 were measured simultaneously. The CL monitor was employed to record the glowing air signal, while the 2B Technologies Personal Ozone Monitor (POM), an UV absorption O_3 monitor (more details on the monitor can be found in Sec. 3.1, Sec. 8.2 and the manual (2B Technologies, 2020)) was utilized to record the O_3 mixing ratio. Additionally, for brief intervals, the C_2H_4 Minican was opened to also record the O_3 mixing ratio with the CL monitor. This comprehensive approach allowed us to assess potential offsets and differences among the measurement techniques.

In the measurements it can be seen that the 'airglow' signal does show similar characteristics as the O_3 signal. However, as expected, the determined 'airglow' calibration factor cannot reliably reproduce the actually measured absolute O_3 values. In Fig. 28a the conversion to O_3 equivalent works surprisingly well, however, in Fig. 28b the calculated O_3 equivalent does not closely match the actually recorded O_3 mixing ratio. This is again an expression of the conclusions drawn during the 'airglow' calibration process. It is likely that during the measurement represented in Fig. 28a, sufficient quantities of the second reactant were available, whereas in Fig. 28b, the limited availability of this reactant led to a reduction in the absolute value of the signal to that of O_3.

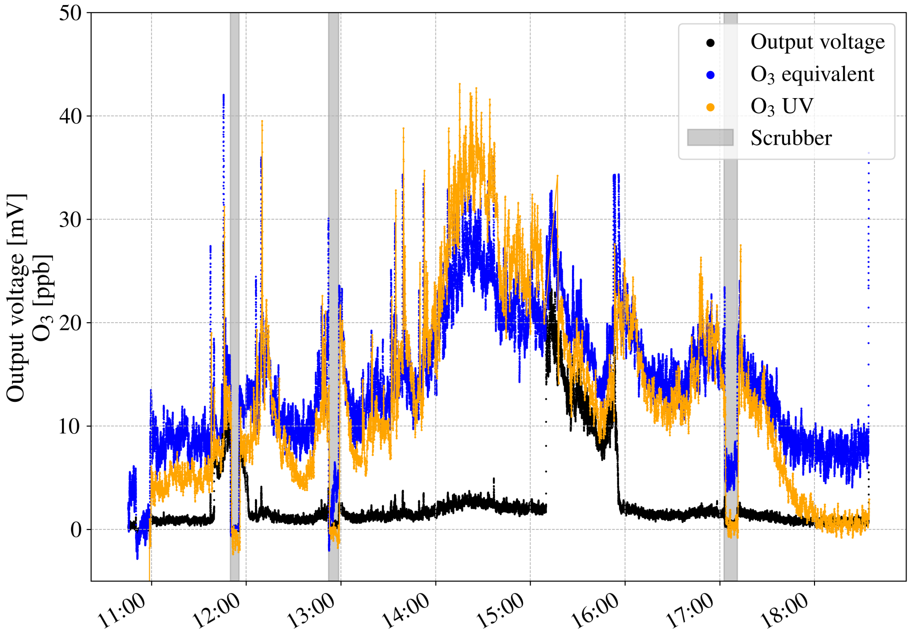

(a) ‘Airglow’ signal and simultaneous O_3 measurement match well.

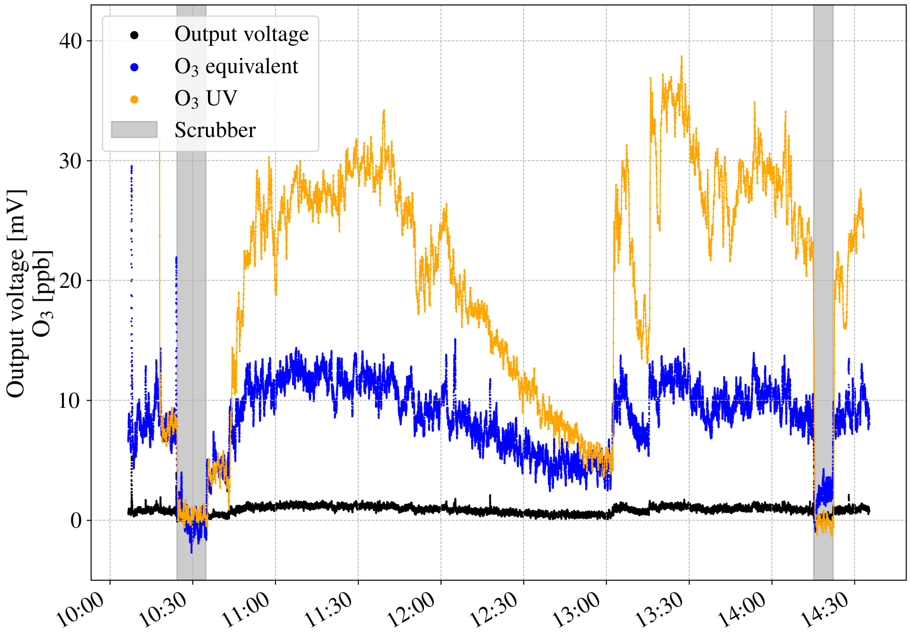

(b) ‘Airglow’ signal and simultaneous O_3 measurement show similar characteristics but deviate significantly in the absolute values.

Figure 28: Time series of ‘airglow’ signal and simultaneous O_3 measurement. The black curve corresponds to the measured PMT output signal, in blue the signal converted to ppb O_3 equivalent (see Fig. 27 for more details) is shown. The orange time series corresponds to the O_3 measurement with the POM.

6.3. 'Airglow' decay time

Additionally, the decay time of the signal is examined. This idea stems from the observation that the 'airglow' signal is not detectable when indoor air is sampled. It is hypothesized that a mechanism analogous to that of O_3 occurs. O_3 reacts with surfaces and is after a certain period completely depleted within a sealed environment. Two approaches are used to analyse the decay in the 'airglow' signal.

The first method investigates the decay time within the entire room. Initially, the 'airglow' signal is recorded while the window is open (long enough to fill the room with fresh air). Then, the window is closed, and the signal decay is recorded. An exponential function can be fitted to the data, where the time constant of the fit represents the decay time of the signal in the room. This is also done for O_3, here the same procedure is followed but the monitor is operated in its normal setup, where C_2H_4 is injected into the measurement cell. The decay times using this method, for the 'airglow' signal and O_3 are presented in Fig. 29a.
In the alternative method, the pump is switched off during the measurement. This prevents fresh air from entering the measurement cell, leading to a signal decrease analogous to the scenario where the window is closed. This approach is also conducted for the decay time of O_3. The measurement is presented in Fig. 29b.

The difference in these two approaches lies in the altered surface-to-volume ratio. With the initial assumption that the relevant reactants interact with surfaces, we expect that the decay time should decrease with an increased surface-to-volume ratio. Estimating the surface-to-volume ratio for both the measurement cell and the room,

$$A_{\text{cell}} = \pi\left(\frac{d}{2}\right)^2 \cdot l \qquad V_{\text{cell}} = 2\cdot\pi\left(\frac{d}{2}\right)^2 + \pi d \cdot l \tag{91}$$

$$\frac{A_{\text{cell}}}{V_{\text{cell}}} = 172\,\frac{1}{\text{m}} \qquad \text{with } d = 3.155\times10^{-2}\,\text{m}, l = 2.85\times10^{-2}\,\text{m} \tag{92}$$

$$A_{\text{room}} = 2\cdot(l\cdot d + l\cdot h + d\cdot h) \qquad V_{\text{room}} = l\cdot d\cdot h \tag{93}$$

$$\frac{A_{\text{room}}}{V_{\text{room}}} = 1.5\,\frac{1}{\text{m}} \qquad \text{with } l = 6\,\text{m}, d = 4\,\text{m}, h = 3\,\text{m} \tag{94}$$

$$\Rightarrow \frac{A_{\text{cell}}}{V_{\text{cell}}} \Big/ \frac{A_{\text{room}}}{V_{\text{room}}} = 114, \tag{95}$$

we see that the decay of the signal in the room should be roughly by a factor of 114 larger than the the decay time in the measurement cell.

The decay times, for both 'airglow' signal and O_3, for both scenarios are depicted in Fig. 29. It can indeed be seen that the decay time inside the measurement cell is much shorter compared to that in the entire room.
The decay times for the 'airglow' and O_3 signal in the room match very well, for both a decay time of ~28 min is determined.
Inside the measurement cell, the decay times of the 'airglow' and the O_3 signal are on the order of tens of s, for the 'airglow' signal it is determined to be ~18 s. However for the decrease of the O_3 signal in the measurement cell, the decay time is only 6 s, reduced by roughly a factor of 3 compared to that of the 'airglow' signal. This is likely related to the fact that C_2H_4 is still injected into the measurement cell and the remaining O_3 also reacts with the C_2H_4 instead of only reacting with the walls of the measurement cell. What is also striking, is the observation that even when the pump is switched off for several

minutes the 'airglow' signal does not fully diminish. Only when a scrubber is attached to the air inlet and the pump is switched on again does the signal go away. This suggests that the 'airglow' signal actually consists of two separate signals, one showcasing a fast decay, the other one a significantly slower.

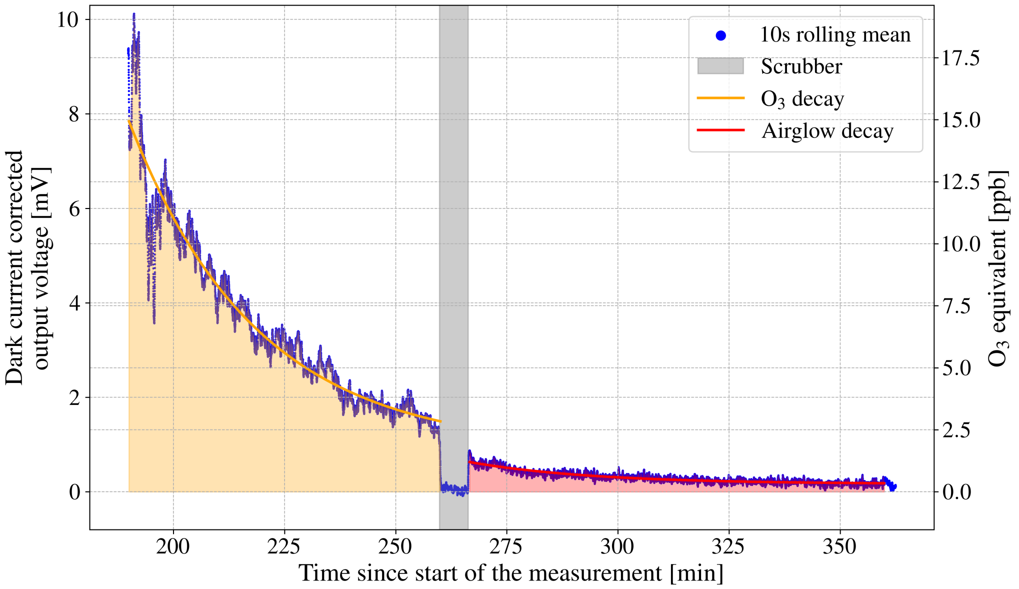

(a) Decay of the 'airglow' and the O_3 signal inside the room. First the signals are recorded with the window open, after the window is closed the decrease in the signal can be observed. In between the two measurements a scrubber is attached to the air inlet.

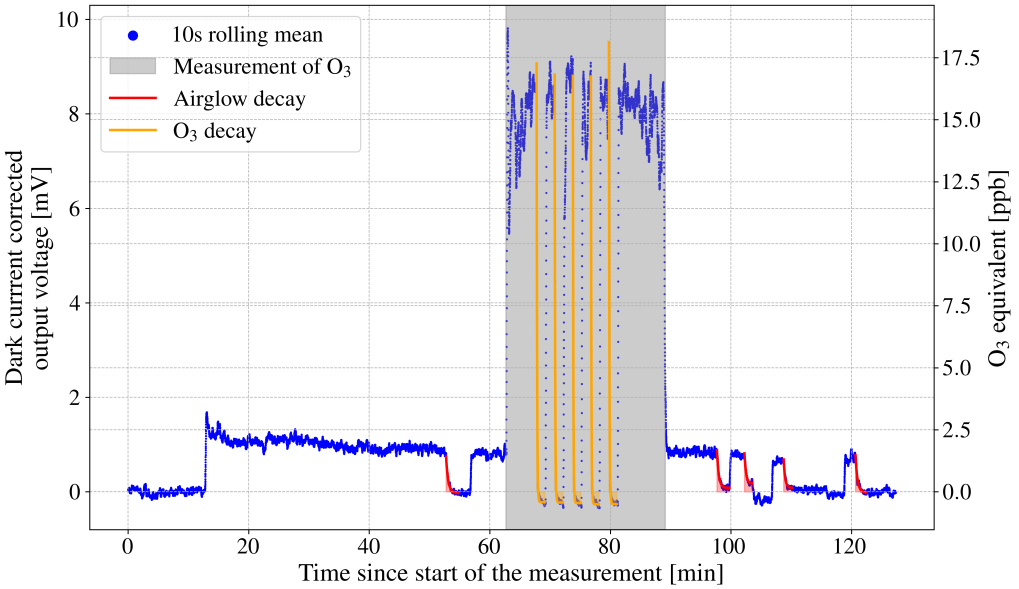

(b) Decay of the 'airglow' and the O_3 signal inside the measurement cell. To observe this the pump is switched off during the measurement. At the end of the 3. and 4. 'airglow' signal decay a scrubber is attached and the pump is switched back on, leading to the sudden drop in the signal at the end of the decrease.

Figure 29: Decay times of the 'airglow' and the O_3 signal for different sealed environments.

Comparing the results from the decay times of the ‘airglow’ and O_3 signal in the room and the measurement cell we see that they are somewhat consistent with the findings of the surface-to-volume ratio. With the surface-to-volume ratio the expected decay time in the room can be calculated from the observed decay time in the measurement cell,

$$t_{\text{room, theo}} = 114 \cdot t_{\text{cell}} \tag{96}$$

$$t_{\text{room, theo},O_3} = 114 \cdot t_{\text{cell},O_3} = 114 \cdot 6\,\text{s} = 11\,\text{min} \qquad t_{\text{room},O_3} = 28\,\text{min} \tag{97}$$

$$t_{\text{room, theo,ag}} = 114 \cdot t_{\text{cell,ag}} = 130 \cdot 18\,\text{s} = 34\,\text{min} \qquad t_{\text{room,ag}} = 28\,\text{min} \tag{98}$$

For the ‘airglow’ signal the from the surface-to-volume ratio determined decay times correspond quite well, for O_3 the decay times do not match well. This discrepancy can likely be attributed to the high concentration of C_2H_4 in the measurement cell compared to the room, as mentioned above.

6.4. ‘Airglow’ at night

Another interesting question regarding the ‘airglow’ signal is whether it persists at night. Analysing this, gives indications into the signals relation to photochemistry. Measurements suggest that the signal is still there even during the night. The measurement is presented in Fig. 30.

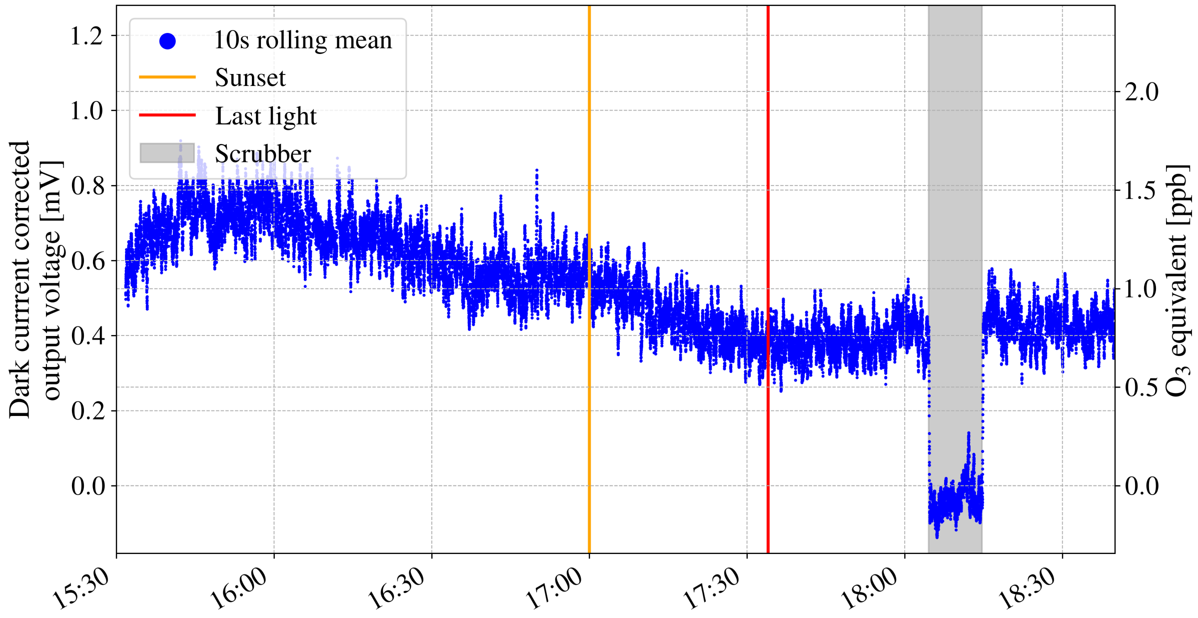

Figure 30: Airglow signal during the evening and the night. The sunset and last light are marked. The signal decreases as the available light decreases but can still be observed even after the last light.

6.5. Is ‘airglow’ observable with the naked eye?

To gain a clearer understanding of the observed signal we determine the expected number of photons inside the measurement cell when the ‘airglow’ signal is observed. For this a ‘calibration’ factor that translates the PMT output signal (in mV) into the number of photons per second in the measurement cell is derived. All influential parameters have to be known, to calculate the theoretical number of photons produced per second (using Eqn. 29). Therefore calibration measurements are used when a known O_3 mixing ratio is sampled. The theoretical number of photons can then be compared against the measured signal and a calibration curve can be derived, as depicted in Fig. 31.

Assuming a PMT signal of 2 mV as a representative ‘airglow’ signal, approximately 8.8×10^4 photons/s are generated within the measurement cell. With this the number of photons per second and cm^3 can be determined,

$$\frac{\gamma}{V} = \frac{8.8 \times 10^4\,\text{photons/s}}{20\,\text{cm}^3} = 4.4 \times 10^3\,\text{photons/s/cm}^3. \tag{99}$$

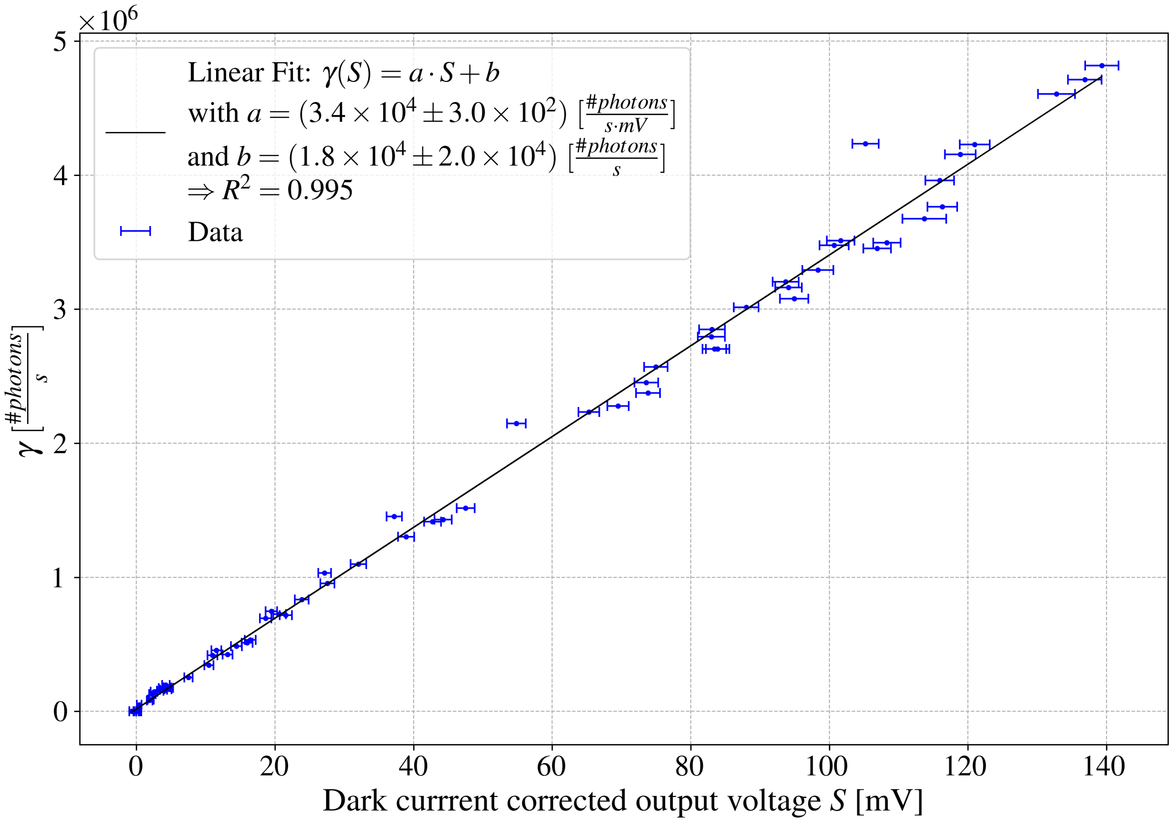

Figure 31: The theoretically calculated number of photons per second is plotted against the measured output voltage. The linear fit to the data points, together with the determined fit parameters and the R^2 value, is shown.

The interesting question is now whether this signal is observable with the naked eye. For this we will make the following assumptions:

- The emitted photons are in the visible range, with a mean wavelength of 555 nm. This is assumed since the human eye is most sensitive for this wavelength, and therefore conversion from the photon flux (photons per second) to the luminous flux (lumen), or the conversion from irradiance ($\frac{\mathrm{W}}{\mathrm{m}^2}$) to illuminance (lux) is maximal.

- The relevant reactions only take place in the first kilometre of the troposphere. Here, it is most likely that the relevant reactants are available in the needed quantities.
- A homogeneous distribution of the relevant reactants is assumed in this first kilometre of the troposphere.

These are only crude assumptions, and should only serve to determine the upper bound for the photons observable with the eye.
We can determine the number of photons per second coming from a column with the area of $1\,\mathrm{m}^2$ of sky,

$$f = 4.4 \times 10^3\,\mathrm{photons/s/cm}^3 \cdot 10^3\,\mathrm{m} = 4.4 \times 10^{12}\,\mathrm{photons/s/m}^2. \tag{100}$$

Assuming the energy of the photons to be $e = 3.5 \times 10^{-19}\,\mathrm{J}$ (for wavelength of $555\,\mathrm{nm}$) the irradiance of the ‘airglow’, and from this the illuminance I (given in lux, lx) can be determined,

$$E_e = f \cdot e = \frac{1}{2} \cdot 4.4 \times 10^{12}\,\mathrm{photons/s/m}^2 \cdot 3.5 \times 10^{-19}\,\mathrm{J} = 0.63 \times 10^{-7}\,\frac{\mathrm{W}}{\mathrm{m}^2} \tag{101}$$

Using: $1\,\mathrm{lx} \equiv 1.464\,\frac{\mathrm{mW}}{\mathrm{m}^2}$ at a wavelength of $555\,\mathrm{nm}$

$$I = \frac{E_e}{1.464 \times 10^3\,\mathrm{mW/m^2/lx}} = 0.43 \times 10^{-4}\,\mathrm{lx} \tag{102}$$

Here we assumed that only one half of the photons are actually emitted in the downwards direction. For comparison some examples of the illuminance are listed below. The ‘airglow’ signal roughly makes up half of the illuminance reached for a moonless, overcast night sky, and is therefore most likely not really observable with the naked eye.

Illuminance	**Surfaces illuminated by**
1×10^{-4}	Moonless, overcast night sky
2×10^{-3}	Moonless clear night sky with airglow
100	Very dark overcast day
1×10^{4}	Full daylight (not direct sun)

Table 1: Compilation of some example illuminance.

7. Measurements

In this section ground based as well as drone based ambient measurements are presented. In Heidelberg, a first measurement during sunrise is conducted, showcasing parts of the diurnal cycle of O_3. Additionally, drone based measurements are shown, from which also a vertical O_3 profile is conducted.

7.1. Measurements in Heidelberg

The diurnal cycle of O_3 strongly depends on the conditions of the respective location. The Neuenheimer Feld in Heidelberg, Germany, where the Institute for Environmental Physics is located, is considered an urban area. There, O_3 concentrations typically exhibit a diurnal cycle, with the lowest levels observed in the early morning hours, increasing during the day to peak in the afternoon, and then decreasing again during the evening and night. This pattern arises mainly due to the interplay of photochemical production of O_3 during the day and its depletion at night (Roedel and Wagner, 2017; Pryor and Steyn, 1995). During the day, NO_2 is photolised to produce NO and O, which can then react with O_2 to form O_3. In a polluted area where hydrocarbons are present NO can be oxidised to NO_2 without the destruction of O_3. This leads to increased O_3 levels during the day. During the night, photolysis of NO_2 is not possible and therefore the production of O_3 is hindered, leading to a decrease in O_3 levels during the night, as O_3 is a potent oxidant and very reactive. However, the diurnal cycle can vary since other anthropogenic emissions, meteorological factors, and vertical mixing can also significantly influence these patterns.

An O_3 measurement during sunrise was conducted at the Institute for Environmental Physics in Heidelberg (see Fig. 32), since during sunrise the most drastic change in the O_3 levels are expected.

To validate the measurement, data from the Umweltinformationssystem (UIS) provided by LUBW Landesanstalt für Umwelt Baden-Württemberg (2023) is used. They operate a measurement station in Heidelberg, located on the Berliner Straße (at the intersection with the Blumenthalstraße). This station is merely a street away from the Institute, making it a good choice as benchmark. Unfortunately, the station only offers hourly data, limiting the precision of the comparison. Nevertheless, a general comparison, particularly concerning the order of magnitude, remains feasible. To better compare the two measurements also hourly averaged data of the CL O_3 monitor is shown. The error bar here, solely consists of the standard deviation which arises from the averaging process.
In the plot, the validation points from the LUBW station align reasonably well with the measurements from the CL O_3 monitor. For all values the two measurement techniques agree with each other within less than 2 sigma, except for the data point at 8 am in the morning, where the deviation corresponds to 2.5 sigma. The deviations are therefore not significant.

The general characteristics of the measured time series aligns with the anticipated course of O_3 levels. The minimum O_3 value is observed around 8:00 with ~ 20 ppb. Then, the O_3 mixing ratio consistently rises until the end of the ambient O_3 measurement at around 12:30 with a value of ~ 35 ppb.

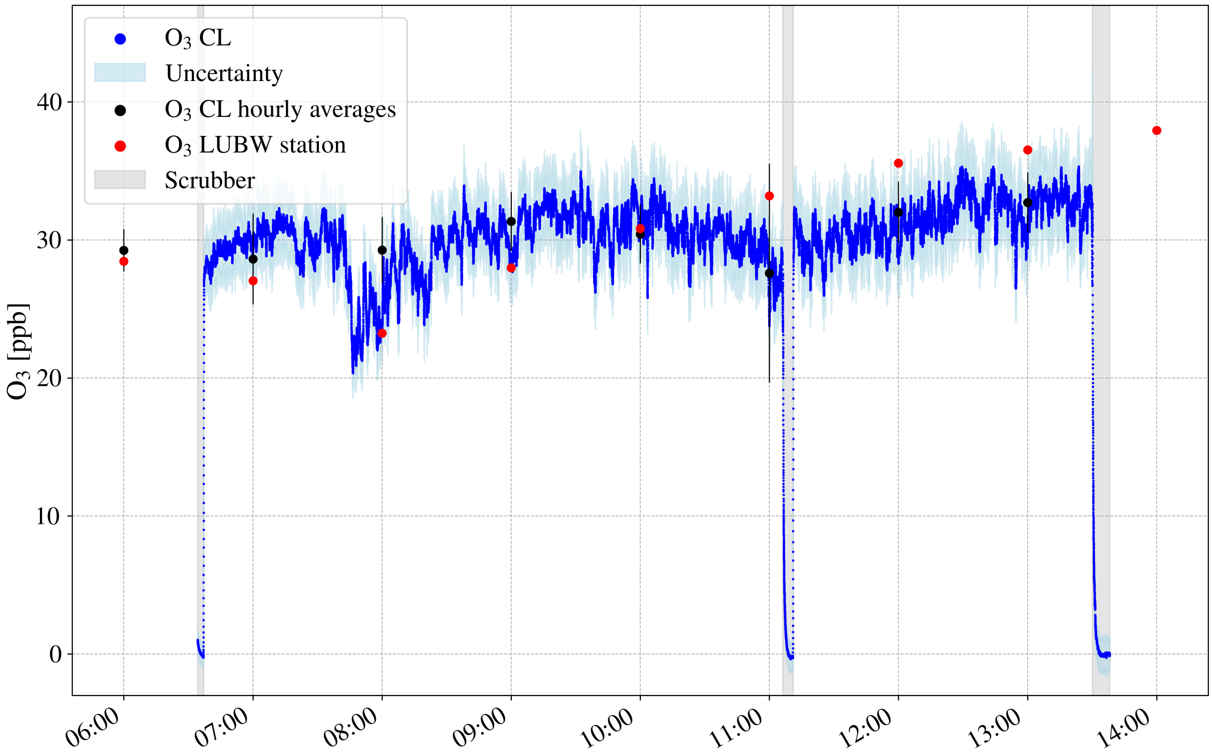

Figure 32: Time series of the O_3 measurement during sunrise as recorded with the CL monitor (blue). Additionally the hourly averaged O_3 mixing ratio is shown (black points). The uncertainty is given by the standard deviation. For validation the hourly measurements from LUBW are shown (red dots). The lowest O_3 value is measured at around 8:00, after that the O_3 mixing ratio increases, as expected. The data from LUBW shows a stronger trend compared to the CL O_3 measurement, but the data still agrees within 2σ with each other.

7.2. Vertical Ozone Profile

With height, O_3 mixing ratios usually increase and reach their maximal value at around 2 to 3 km altitude. This increase with height can be explained with the destruction of O_3 close to the ground, mainly through organic material (Roedel and Wagner, 2017).

A first drone-based measurement was conducted on February 24th, 2023, at Kleiner Feldberg, Taunus, Germany, the second-highest peak in the Taunus region with a height of 825 m. At this location there is an air quality monitoring station of the Hessisches Landesamt für Naturschutz, Umwelt und Geologie (HLNUG) (2023), and a weather station of the Deutscher Wetterdient (DWD) (2023). The measuring stations are located at an elevation of 811 m and are surrounded by woods and farming areas with minimal traffic. The HLNUG station measures NO, O_3 and particulate matter, as well as meteorological data such as wind direction and velocity, air temperature, humidity, and global radiation. This makes the site a suitable choice for a comparison of O_3 measurements carried out by a permanent installed O_3 monitor and the in this thesis developed CL O_3 monitor.

Fig. 33 shows the monitor on the drone as well as the O_3- and pressure measurement.

(a) Monitor mounted on the drone at the Kleiner Feldberg.

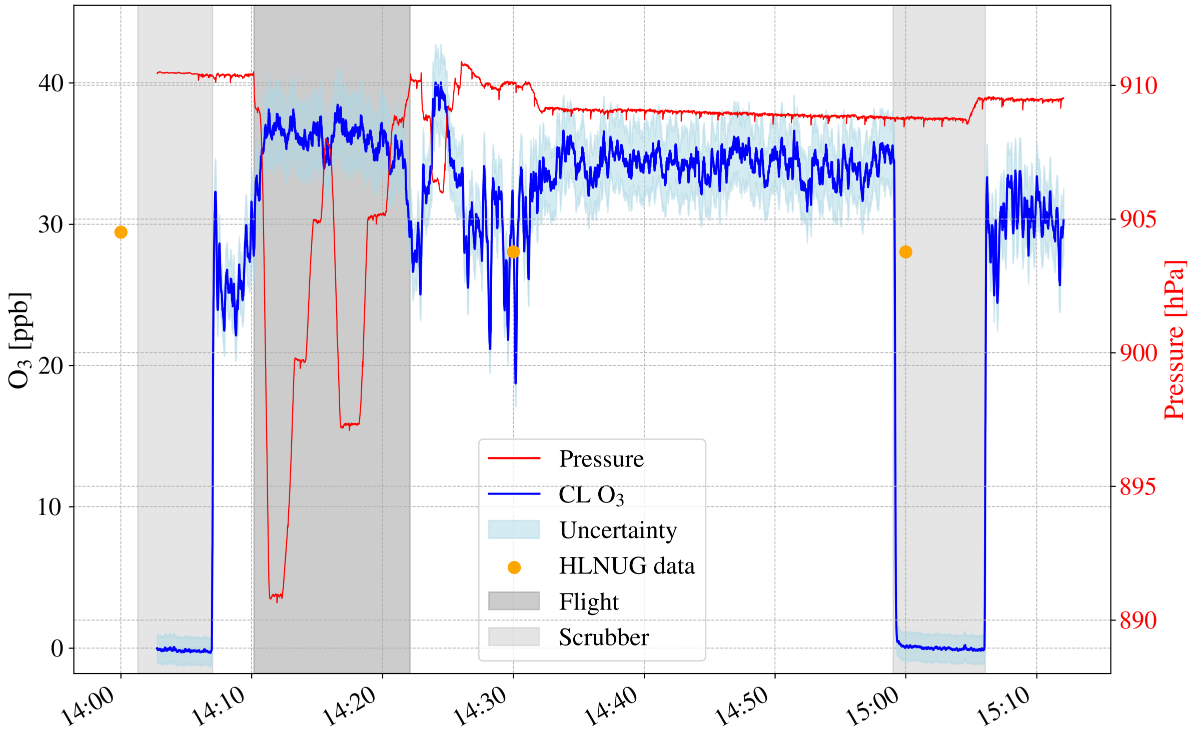

(b) O$_3$ measurement (blue) overlaid with the pressure measurement (red) indicating the height. The period of the flight is marked by the grey shaded area. The data from the HLNUG measurement station is also shown as red data points.

Figure 33: Drone-based measurement at Kleiner Feldberg.

The measurement was started on the ground before attaching the monitor to the drone. At approximately 14:00 the drone took off, first reaching around 180 m altitude above ground (see first dip in the pressure in Fig. 33) before descending due to high wind speeds. Later the drone ascended again to around 120 m. Following a brief moment of ground based measurements, the drone manoeuvred above the close by forest at around 14:25. After the drone landed again, the monitor was carried over a grassy area to where the drone initially started. This time period is characterised by stronger O$_3$ variations compared to the rest of the measurement.

Afterwards, the measurement continued on the ground. From 14:32 to 15:05, the monitor was positioned on the slightly elevated measurement platform (roughly 2 stories high), indicated again by a drop in ambient pressure.

The expected results, namely increasing O_3 levels with increasing altitude, can be seen in the measurement. Notably, the difference between 10 m (height of the platform) to 180 m is not as pronounced as the difference between near-ground and 10 m elevation. Considering that O_3 is destroyed close to the ground mainly trough organic material, this is not surprising. The maximum O_3 value was measured above the forest, and the lowest O3 value was recorded above the grass land.

Further vertical O_3 profiles were recorded. One flight took place in Heidelberg, Germany, in an agricultural area close to the university, the Neuenheimer Feld. Another flight was conducted at Piano Provenzana (starting elevation: ∼1810 m, Etna, Sicily (more details on Etna can be found in Sec. 8.1). These measurements can be found in the Appendix (see Sec. B).
Another vertical O_3 profile was recorded at Piano Vetore, at the southern flank of Etna in June 2023. This measurement is shown in Fig. 34. Here, the starting altitude of ∼1740 m is much higher compared to the measurement at Kleiner Feldberg (∼800 m). This and additionally, the change in season (from winter to summer) and location, might explain the already higher mixing ratio at the ground. In this measurement as well, the typical characteristics of an increasing O_3 mixing ratio with height can be seen. Additionally, O_3 is measured using the UV absorption monitor, POM, for comparison during the measurement duration at the ground. During this measurement the POM exhibits significant variations in the O_3 measurement that can not be observed with the CL monitor. Even for periods during which a scrubber was used these strong fluctuations can be seen in the time series of the POM. This indicates that the fluctuations are most likely an artefact of the measurement from the POM.

These drone based measurements shown (and mentioned) here, as well the plume measurements (refer to Sec. 8.3), show an increased mixing ratio of O_3 at ground level after the flight compared to before the flight. Why this is the case is not known.

A vertical O_3 profile is constructed using the measurements shown here, the plume measurements, and a set of further ambient measurements with varying ambient pressure values (measurements conducted at different altitudes but constant altitude during the measurement itself). In this profile, periods during which ambient O_3 is measured (excluding periods within the plume where $SO_2 > 1\,\text{ppm}$) are plotted against their corresponding altitudes. The altitude is calculated from the ambient pressure using the barometric height formula:

$$h = \frac{RT}{g} \ln\left(\frac{p_0}{p}\right), \tag{103}$$

where h is the altitude above sea level, R is the universal gas constant, T is the ambient temperature in Kelvin, g is the acceleration due to gravity, p_0 is the pressure at sea level, p is the pressure at altitude h.

Based on this, an average expected O_3 mixing ratio for each altitude can be determined. For this the mean O_3 mixing ratio for all data points within a pressure bin of 10 hPa is calculated. The uncertainty of the mixing ratio is given by the standard deviation, for the pressure simply the width of the pressure bin is used.

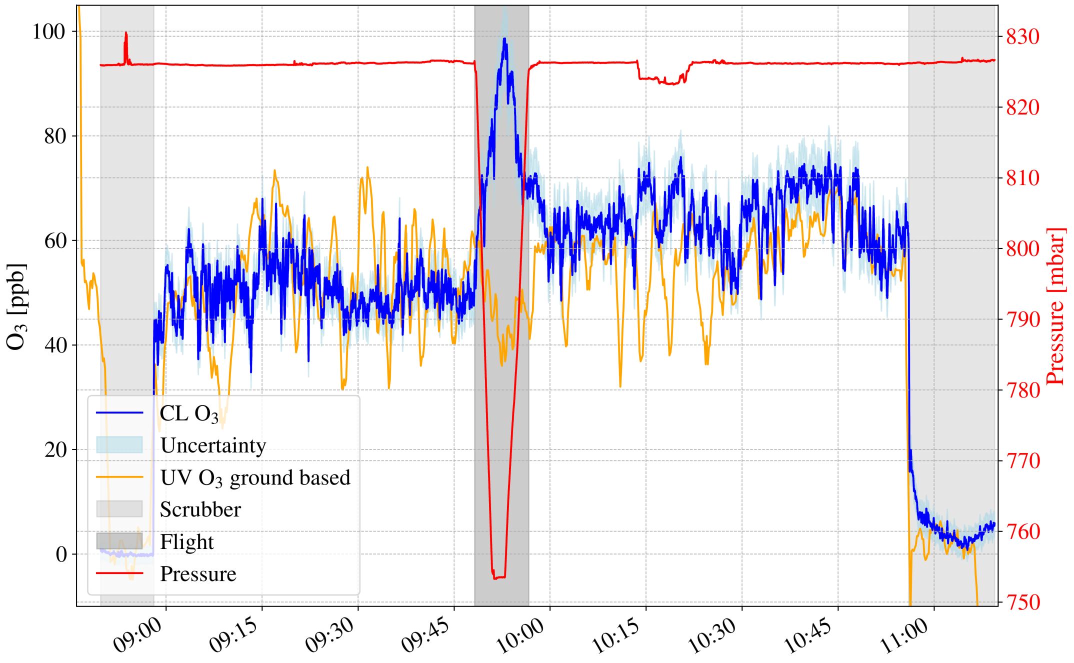

(a) Entire time series.

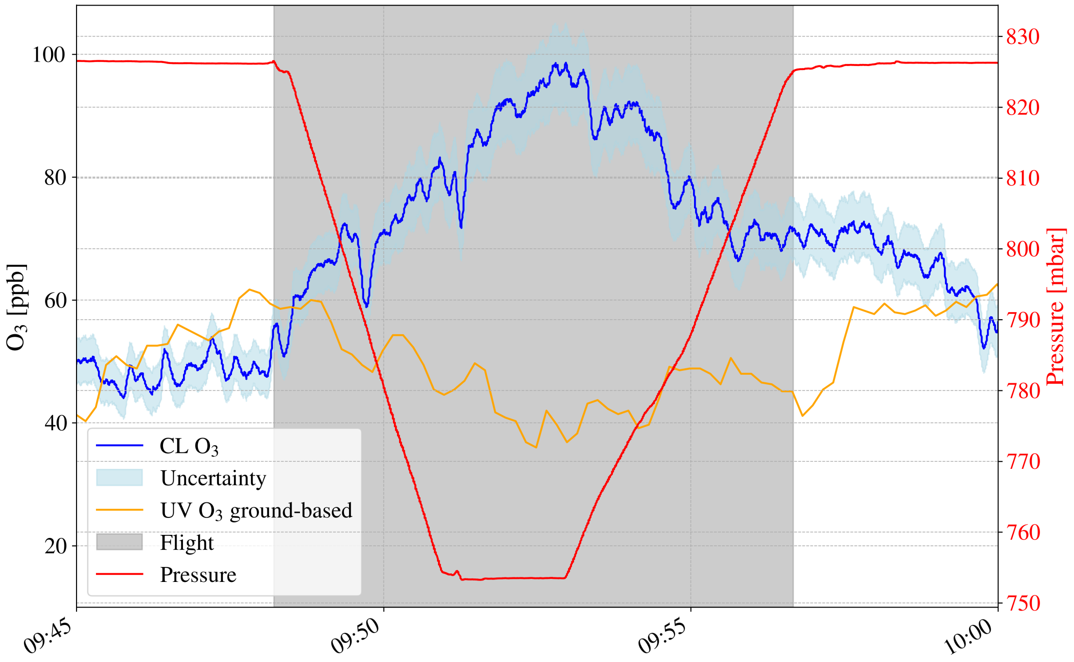

(b) Zoom into period of the flight.

Figure 34: Time series of the drone based CL O_3 measurement at Piano Vetore, the time series recorded with the CL monitor is shown in blue. For comparison O_3 with the POM, an UV absorption monitor, is measured (orange). Additionally, ambient pressure (red) is shown, indicating the flight with the corresponding height. For increasing height also the O_3 mixing ratio increases. In this case, the measurements from the CL and UV O_3 monitor do not correspond well. During this measurement most likely the UV monitor did not produce reliable results and showed strong variations. This becomes obvious during the scrubber measurement at the beginning and the end of the measurement.

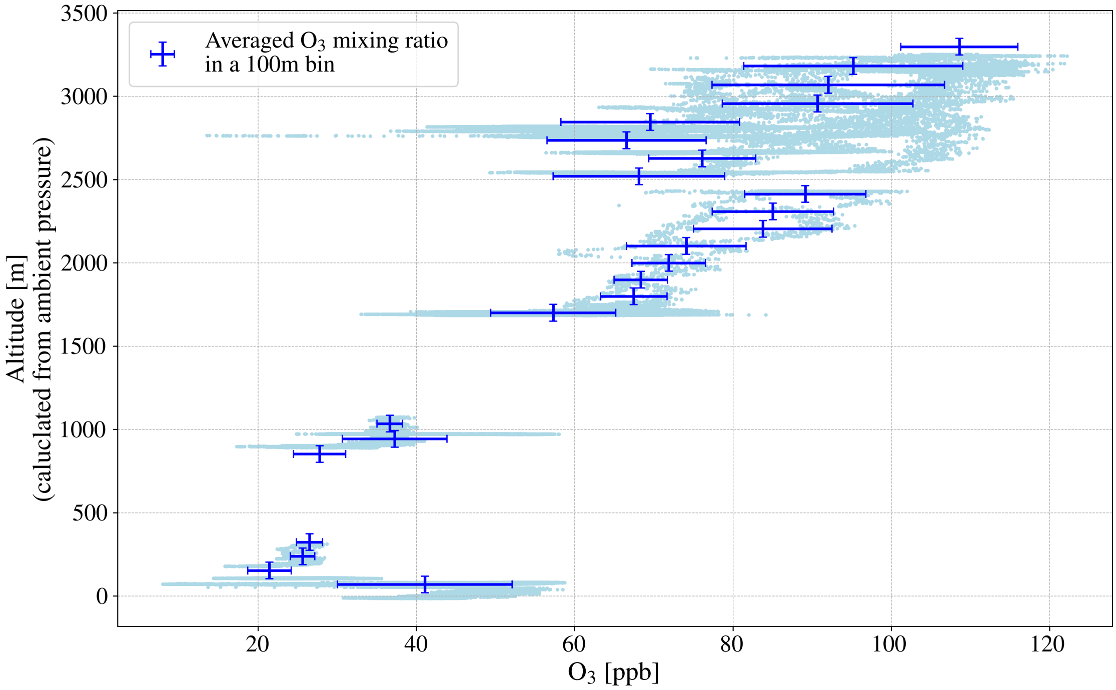

Figure 35: Vertical O_3 profile compiled from several measurements. The data points (and uncertainties) are determined by averaging the O_3 mixing ratio for all data points within a pressure bin of 10 hPa. It can be seen that the O_3 mixing ratio increases with height (increases with decreasing ambient pressure).

8. Field measurements at Etna

In this section the drone based plume measurements at Etna are presented. Before that, a short description of Etna, as well as of the used instruments is given.

8.1. Location and conditions

Etna is situated along the eastern coastline of Sicily and is renowned as one of the largest and most active volcanoes worldwide (Bobrowski and Platt, 2007; Bobrowski et al., 2007). Its volcanic activity has been documented since Greek colonization (700 BC), although its history dates back even further, starting approximately 0.6 million years ago (Branca et al., 2004).

Over time, structural and morphological changes have shaped the summit area of the volcano, with significant evolution observed during the twentieth century. Currently, Etna has four active summit craters: Bocca Nuova (BN, 1968), Voragine (VOR, 1968), Southeast (SEC, 1978), and Northeast crater (NEC, 1911) (Branca and Del Carlo, 2004; Bobrowski and Platt, 2007). The summit of Etna reaches a height of 3300 m above sea level (Bobrowski and Platt, 2007).

Prior to these formations, the summit area consisted of a single crater known as the central crater (CC) (Branca and Del Carlo, 2004). The NEC first emerged as a pit on the northern flank of the CC in 1911. Subsequently, in 1968, a new pit crater named BN formed on the western flank of the CC. The formation of BN caused significant changes to the CC, resulting in its renaming as Voragine. In 1971, another pit crater formed to the south-east of BN, and in 1978, it gave rise to a new cinder cone known as SEC (Branca and Del Carlo, 2004). Refer to Fig. 36 for a map depicting the summit of Etna.

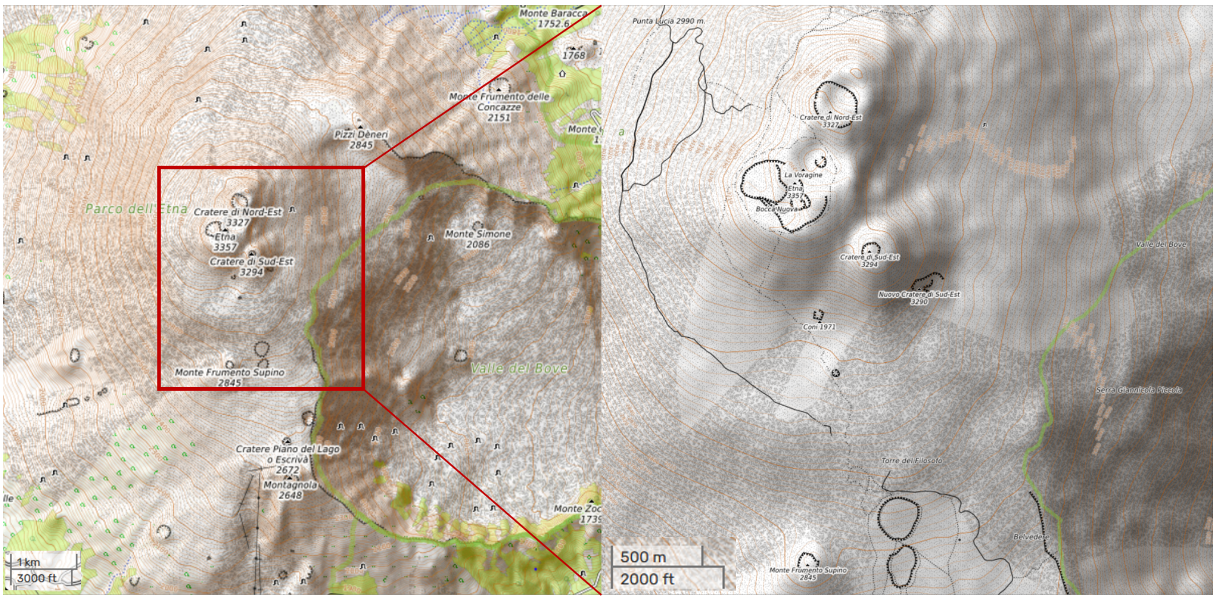

Figure 36: Map depicting the summit area of Etna. On the right side a zoom into the summit area marked with the red square is shown. Map data: © OpenStreetMap contributors, SRTM | Map display: © OpenTopoMap (CC-BY-SA).

The measurement campaign took place from 05.06.2023 to 18.06.2023. Throughout the campaign, Etna's activity was characterized by continuous outgassing at BN and SEC, as documented by INGV National Institute of Geophysics and Volcanology (2023a,b). The observed SO_2 fluxes ranged from medium to medium-low, the CO_2 levels consistently ranged between medium and high values. The elevated CO_2 flux started at the beginning of May, peaking towards the end of May and early June. Throughout the campaign, the CO_2 fluxes remained high, albeit with a marginal decline observed compared to the weeks before. For both weeks of observation, the volcanic tremor amplitude remained at a moderate level, accompanied by a minimal fracture seismic activity.

8.2. Instrumentation and data evaluation

The following instruments have been used during the campaign:

- CL O_3 monitor → VOLCANO$_3$
- UV absorption O_3 monitor → POM, 2B Technologies 2B Technologies (2020)
- SO_2/CO_2 sensor → little-RAVEN (Karbach et al., 2022)
- Drone → Matrice 300 RTK, DJI, https://enterprise.dji.com/de/matrice-300/specs

The CL O_3 monitor is described previously (refer to Sec. 4.1).
The POM is a compact and portable UV O_3 monitor (for a description of the operation principle see Sec. 3.1), measuring just 10 x 8 x 3 cm and weighing approximately 350 g. In order to keep the monitor small but keep up measurement accuracy it features a u-shaped measurement cell with mirrors in its corners, giving a light path of 15 cm. Its also very energy-efficient and requires only about 3 W of power. Beyond recording O_3 mixing ratios, the device also logs cell temperature and pressure, which are needed to calculate the O_3 mixing ratio from the measured intensities. Additionally, it logs GPS data, including latitude, longitude, altitude, and signal quality. For an in-depth overview of the instrument, refer to its operation manual (2B Technologies, 2020).

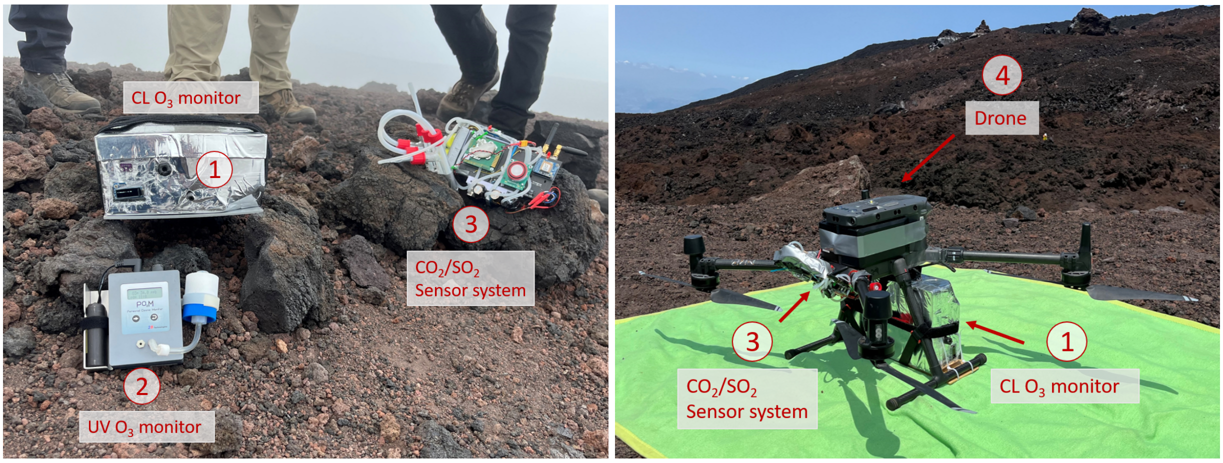

(a) CL O_3 monitor (1), POM (2), and sensors system (3) during a ground based measurement.

(b) CL O_3 monitor (1) and sensor system (3) mounted on the drone (4).

Figure 37: Measurement set up at Etna.

The CO_2/SO_2 sensor system little-RAVEN is built around an ESP microcontroller, managing a variety of sensors. These include an electrochemical SO_2 sensor (Alphasense SO2-B4 paired with its corresponding Individual Sensor Board (ISB)), an S300 CO_2 sensor (ELT Sensors), a BME280 for measuring temperature, humidity, and pressure, a GPS module, as well as a RFD868 module.
With a sampling rate of 0.5 Hz, the system logs all data onto the microcontroller's internal flash memory before transmitting it to the ground station through the RFD868 module. The gas sensors' response times have been experimentally determined: 40 s for the CO_2 sensor and 8 s for the SO_2 sensor. The total weight of little-RAVEN is 1.23 kg. Unfortunately the SO_2 sensor can only measure up to a maximum value of 15 ppm SO_2. A comprehensive description of the sensor system can be found in Karbach et al. (2022).

The Matrice 300 RTK is a commercial drone and has the dimensions of 810 x 670 x 430 mm (unfolded, without propellers). It weighs approximately 3.6 kg without batteries and around 6.3 kg with two batteries installed. The maximum payload capacity is 2.7 kg. Under optimal conditions, the drone achieves a flight duration of 55 min. Given the payload (CL O_3 monitor and CO_2/SO_2 sensor system) as well as possibly windy measurement conditions, the operational time decreases. We operate the drone only approximately 20 min, providing a buffer for unforeseen circumstances. The total weight of the drone, including additional equipment like spare batteries (potentially a third set) and remote control, is approximately 10 kg.

In order to use the CL monitor in the field additional equipment is needed. This includes a spare C_2H_4 Minican, a wrench for the C_2H_4 bottle valve, and scrubbers to calibrate zero signal for both O_3 monitors. Everything used for the measurements, including all three instruments (with transport cases), the drone as well as the additional equipment, weighs in total sim15 kg.

The CL monitor together with the CO_2/SO_2 sensor system were mounted onto the drone, whereas the POM monitored ambient levels at ground level, offering a reference for the CL O_3 measurements when the monitor was stationary. The CO_2/SO_2 sensor system is crucial to locate the plume during flights and later confirms when the plume gases were being measured. A picture of the used instruments and the set up in the field can be seen in Fig. 37.

Given the distinct characteristics of the various monitors and sensors, post-processing of data is crucial to account for the differences listed below. One such discrepancy arises due to the different timekeeping methods of the instruments. Both the SO_2/CO_2 sensor system and the CL O_3 monitor utilize GPS time. The POM, on the other hand, requires to manually set the time which is generally less precise. To synchronize the time axis between the POM and the CL O_3 monitor, distinct features in the O_3 time series that are observable in both monitors are used. Specifically, step changes in the O_3 mixing ratio, produced by attaching or detaching scrubbers simultaneously to the monitors, are used for this purpose. This also introduces uncertainty, the precision reached with this method is however satisfactory for the purpose.
Another difference in the instruments is their respective response times. To accommodate this, a response correction algorithm is implemented (Karbach et al., 2022). This is particularly important for the CO_2 sensor, which has a response time of 40 s, and the SO_2 sensor with a response time of 8 s. This ensures the comparability of these measurements with the O_3 readings from the CL O_3 monitor.
The response correction algorithm is based on the mathematical representation of a first-

order step response function. It requires only the slope of the measured function ($\frac{dc}{dt}$) and the sensor's response time τ (for a more detailed description see Karbach et al. (2022)),

$$c_{\text{corrected}} = c_{\text{measured}} + \frac{dc}{dt} \cdot \tau. \tag{104}$$

8.3. Volcanic plume measurements and results

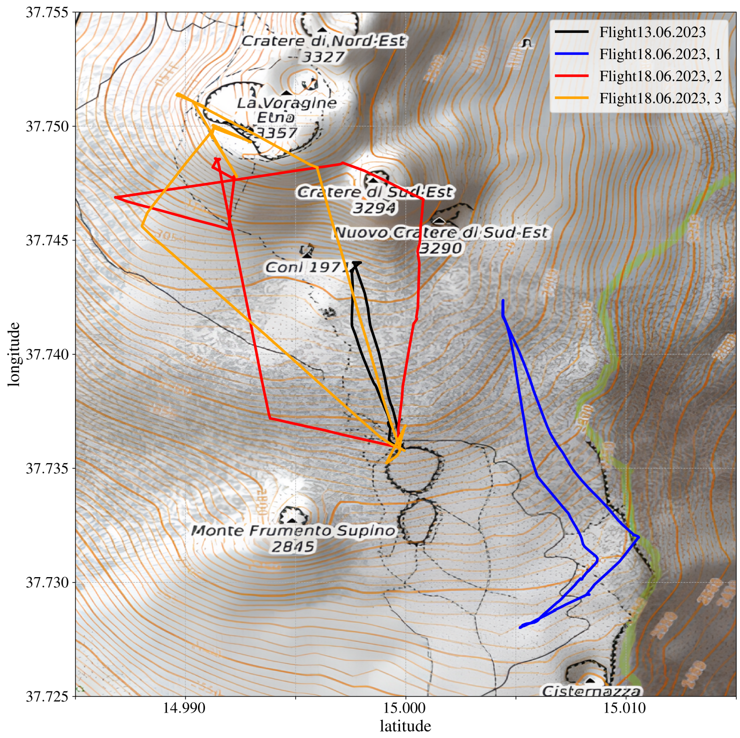

Figure 38: Map of the summit area of Etna with the flight paths for the four plume measurements. The measurement on 13.06., as well as 18.06, 3, sampled the BN plume. The first flight on 18.06, 1, manoeuvred trough the SEC plume and the second flight on 18.06, 2, first sampled the SEC plume before measuring the BN plume. Map data: © OpenStreetMap contributors, SRTM | Map display: © OpenTopoMap (CC-BY-SA)

During the campaign, a total of four plume flights were conducted. The flight paths of all four plume measurements are shown in Fig. 38.

On June 13th, the drone sampled the BN plume (black flight path in Fig. 38). The drone started at the Barbagallo craters (the upper pyroclastic cone from the 2002 eruption), south westerly of the SEC (see Fig. 39c). The meteorological conditions were sunny with some clouds and with wind blowing mainly from North with low wind speeds. Due to the low wind speeds the plume rose before drifting to the south.

Fig. 39 shows the data obtained from this flight. It has to be noted that the SO_2 data (and GPS data) from this measurement is only the result of a provisional evaluation. In Fig. 39a the time series of O_3 and SO_2 are shown, zooming into the period when plume gases were sampled as well as the full time series. The full time series includes the ambient O_3 measurement at ground level at the volcano, highlighting the natural variations in O_3 levels. The data points from the CL O_3 monitor are colour-coded according to the ambient pressure, indicating the altitude of the measurement. During the measurement, ambient O_3 values of around 100 ppb have been recorded. Inside the plume, SO_2 values of up to ~17 ppm have been measured. Here, a peak value of SO_2 is reached that should not be detectable with the SO_2 sensor, since it usually exhibits a maximum value of 15 ppb. This is due to the evaluation of the data for this specific measurement being only provisional at the moment. For high SO_2 values, the O_3 values dropped to around 80 ppm, a decrease of 20 ppb, indicating an anti correlation of O_3 and SO_2. This is a more significant variation that what can be seen in the ambient O_3 levels, where variations are around 10 ppb. Fig. 39b shows the correlation plots between O_3 and SO_2, with a correlation coefficients of -0.45. While O_3 is inherently variable, a slight correlation is still visible in the plot. The trajectory of the flight with the corresponding SO_2 values (indicating where the plume is) is depicted in Fig. 39c.

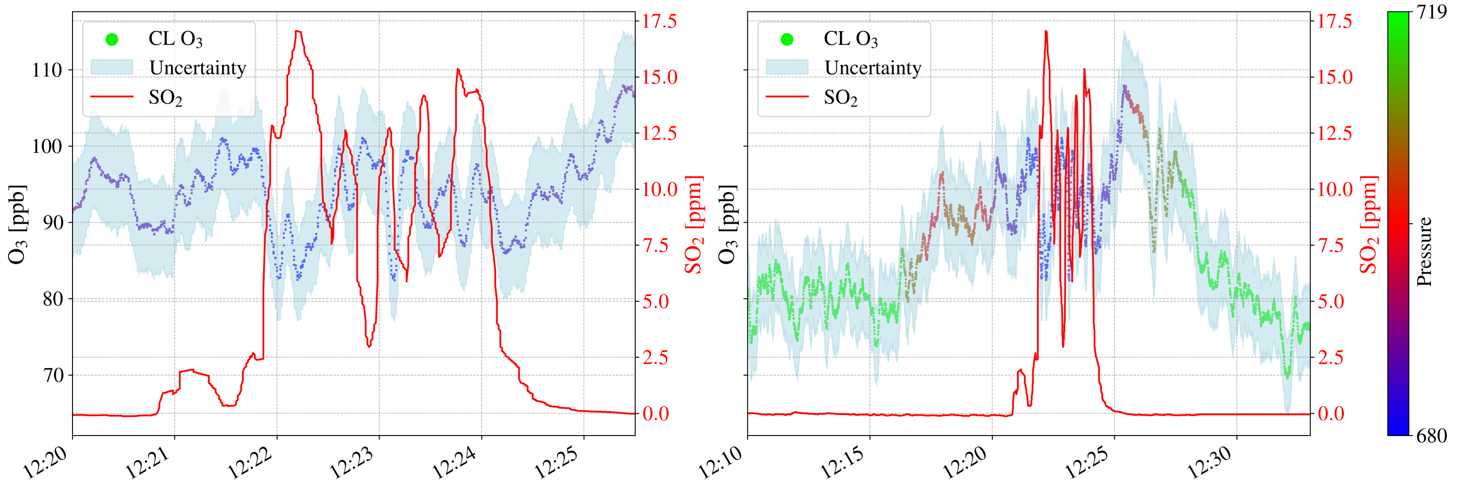

(a) Time series of O_3 and SO_2, just showing the period of the flight and a longer part, including ambient measurements at the ground.

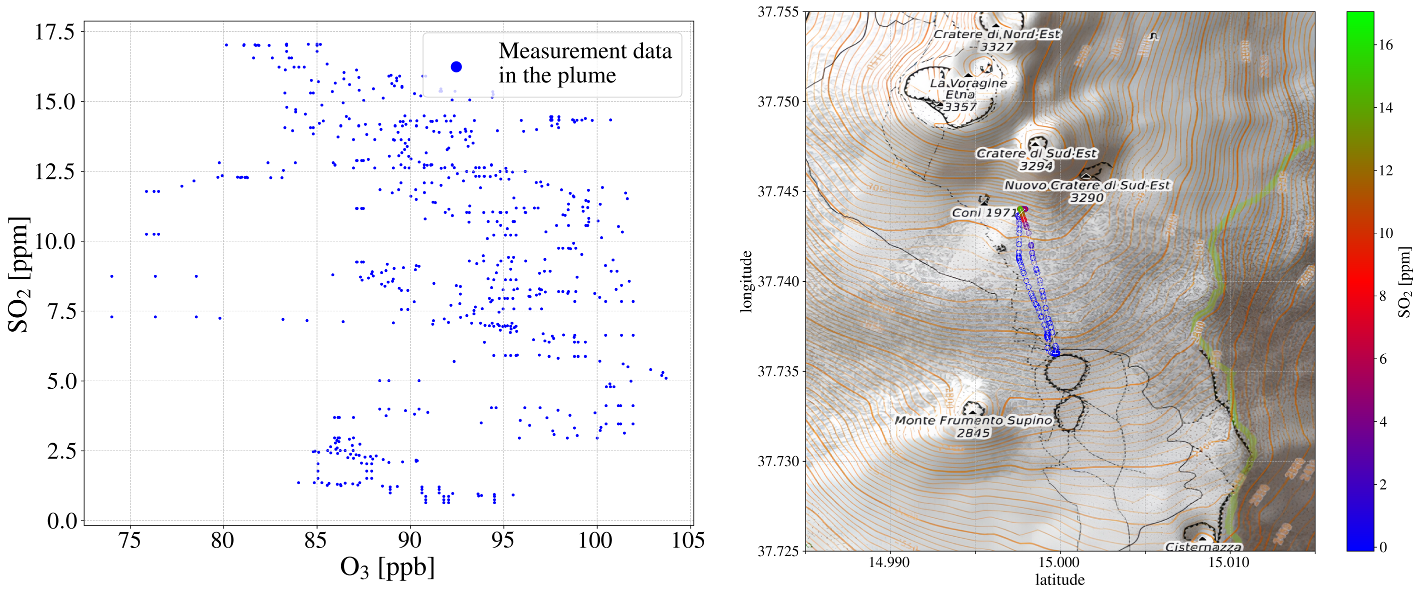

(b) Correlation plot for O_3 and SO_2, from the period of the flight. The correlation coefficient is -0.45.

(c) Map plot showing the flight route as well as the corresponding SO_2 values, indicating where the plume is. Map data: © OpenStreetMap contributors, SRTM | Map display: © OpenTopoMap (CC-BY-SA).

Figure 39: Plume measurement on 13.06.2023, sampling the BN plume with starting point at Torre del Filosofo.

On June 18th, three more flights were carried out. The first started south-southeast of the Barbagallo craters, north-northwest of the Cisternazza and Piano del Lago crater and navigated through the SEC plume, the measurement is depicted in Fig. 40. The subsequent flight first sampled the SEC plume before measuring inside the BN plume. This measurement is shown in Fig. 41. The final flight focused solely on sampling the BN plume, which can be seen in Fig. 42. These two latter flights started from the northern rim of the Barbagallo crater. The weather was sunny, and only little wind, mainly from the north, this meant that the plume basically ascended and was not pushed down too much.

In all of these measurements an anti-correlation of O_3 and SO_2 levels is visible. The ambient O_3 fluctuations are in the range of 5 ppb, whereas within the plume variations of up to 60 ppb are observed. Unfortunately, the SO_2 sensor is only able to measure SO_2 mixing ratios of up to 15 ppm, leading to higher values being cut of. This obscures part of the correlation. In the third measurement, the SO_2 sensor frequently reaches its maximum value within the plume, at 15 ppm SO_2. This effect is evident in the correlation plot, where data points are densely clustered at high SO_2 mixing ratios.

The main findings of the four plume measurements are summarised in Tab. 2.

Date 2023	**Mean ambient O_3 at ground [ppb]**	**Mean ambient O_3 at height of plume [ppb]**	**Mean O_3 in the plume [ppb]**	**Mean O_3 depletion [%]**	**Minimum O_3 in plume [ppb]**	**Maximum O_3 depletion [%]**	**Mean SO_2 [ppm]**	**Maximum SO_2 [ppm]**	**Correlation coefficient**
13.06	80 ± 4	97 ± 6	93 ± 5	4%	82	15%	7.4 ± 5.2	17	-0.45
18.06, 1	66 ± 4	101 ± 4	91 ± 13	10%	52	49%	3.4 ± 2.5	9.7	-0.69
18.06, 2	62 ± 4	111 ± 4	97 ± 14	13%	60	46%	5.2 ± 3.9	13.9	-0.75
18.06, 3	64 ± 3	109 ± 3	91 ± 13	16%	45	59%	8.5 ± 5.4	15.0	-0.67

Table 2: Summary of the plume measurement results. Mean ambient O_3 levels at the ground and at the height of the plume are determined by averaging over the the respective periods determined by the ambient pressure (and excluding data points with SO_2 mixing ratios larger than 0.5 ppb). The mean O_3 inside the plume is obtained by averaging over periods for which $x_{SO_2} > 0.5$ ppb. The mean O_3 depletion is determined by comparing the mean O_3 inside the plume with the mean ambient O_3 at height of the plume. The maximum O_3 depletion is calculated using the minimum O_3 value inside the plume and comparing it to the ambient O_3 at height of the plume.

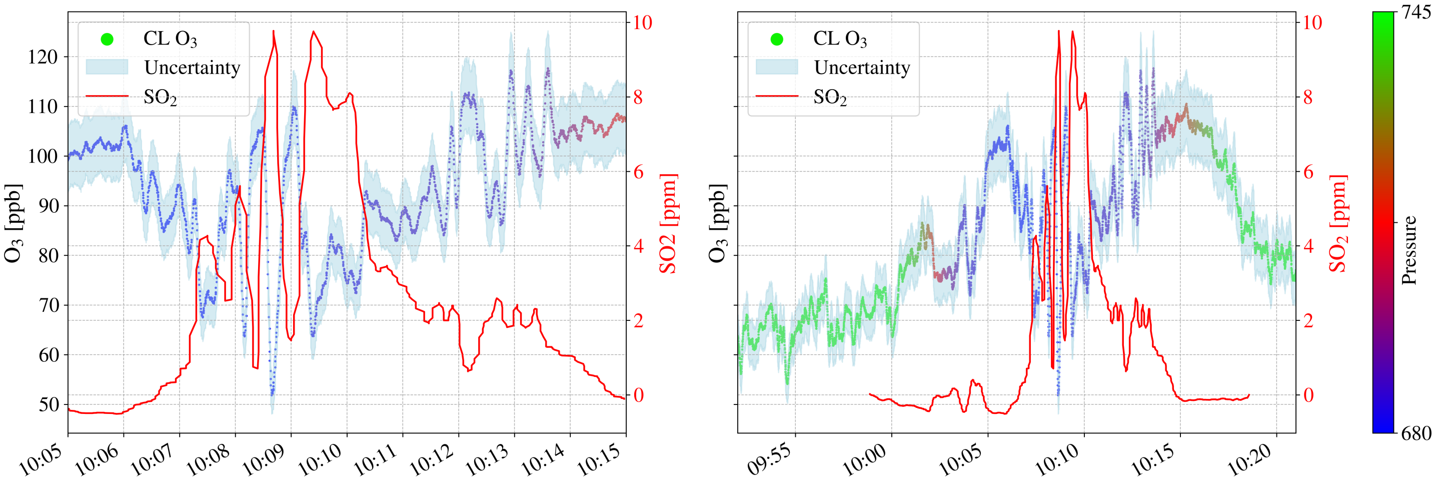

(a) Time series of O_3 and SO_2, just showing the period of the flight and a longer part, including ambient measurements at the ground.

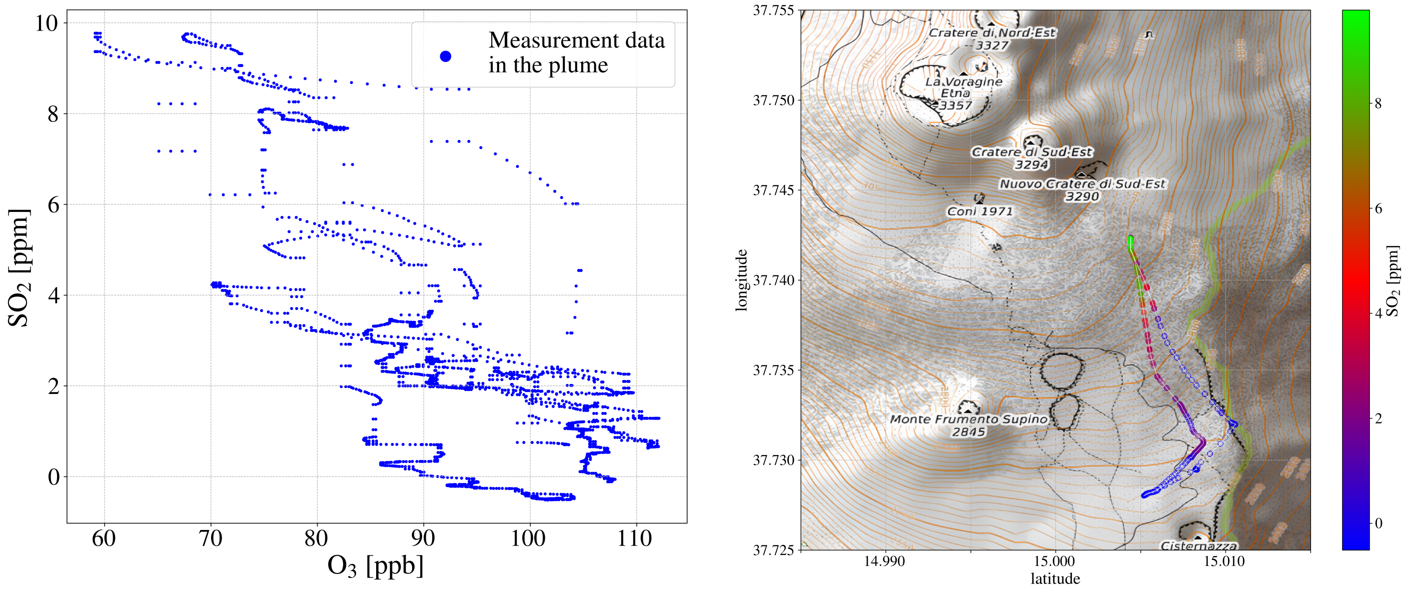

(b) Correlation plot for O_3 and SO_2, from the period of the flight. The correlation coefficient is -0.69.

(c) Map plot showing the flight route as well as the corresponding SO_2 values, indicating where the plume is. Map data: © OpenStreetMap contributors, SRTM | Map display: © OpenTopoMap (CC-BY-SA).

Figure 40: Plume measurement on 18.06.2023, sampling the SEC plume.

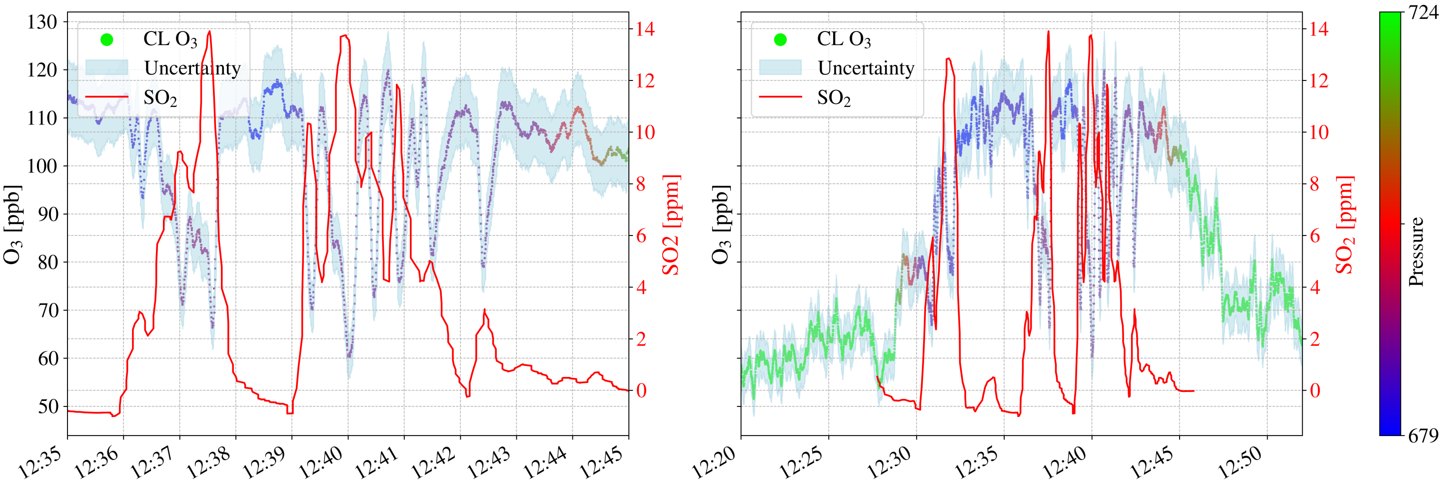

(a) Time series of O_3 and SO_2, just showing the period of the flight and a longer part, including ambient measurements at the ground.

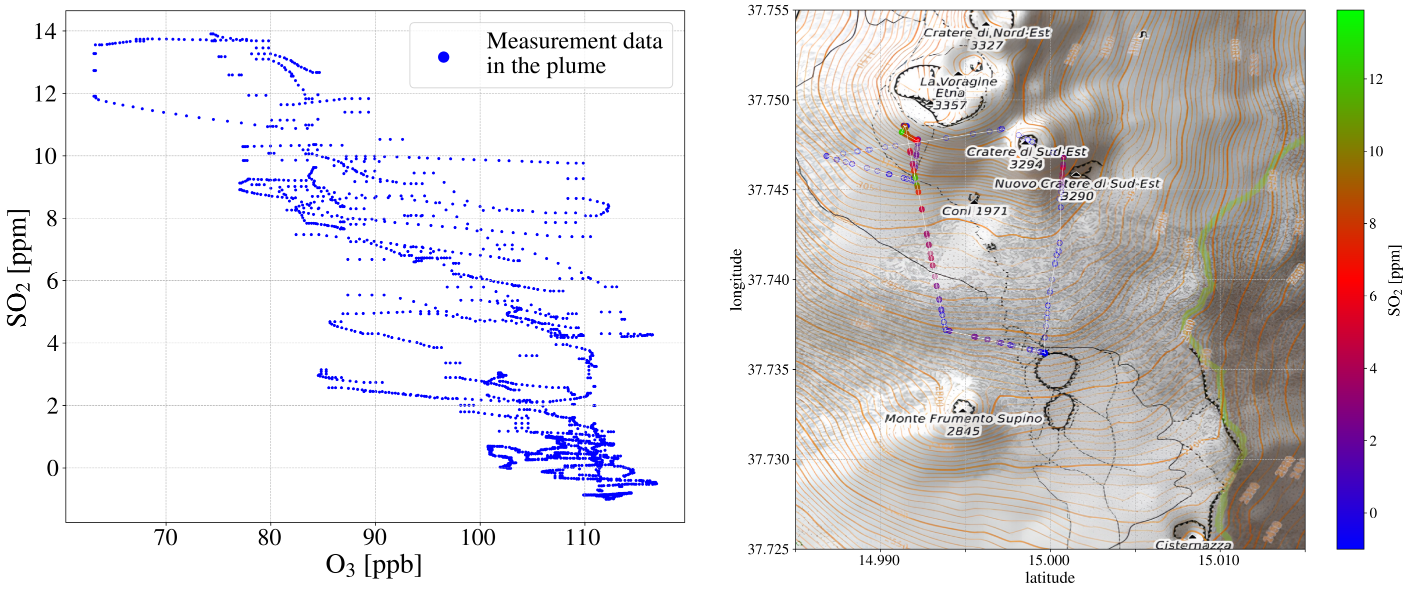

(b) Correlation plot for O_3 and SO_2, from the period of the flight. The correlation coefficient is -0.75.

(c) Map plot showing the flight route as well as the corresponding SO_2 values, indicating the location of the plume. Map data: © OpenStreetMap contributors, SRTM | Map display: © OpenTopoMap (CC-BY-SA)

Figure 41: Plume measurement on 18.06.2023, sampling the SEC and BN plume with starting point at Torre del Filosofo.

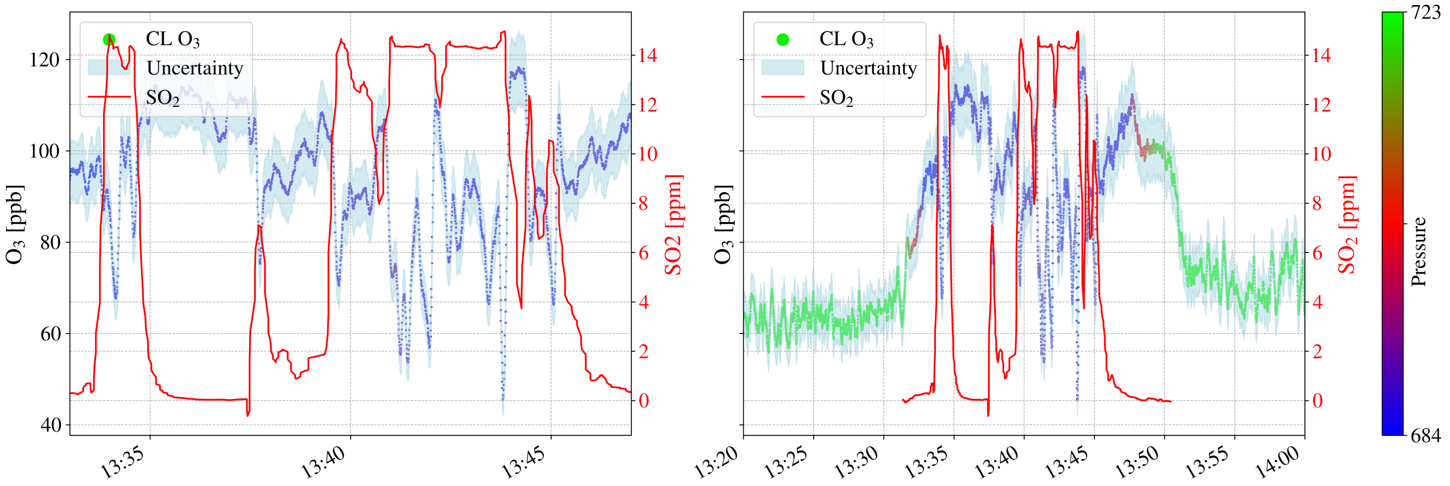

(a) Time series of O_3 and SO_2, just showing the period of the flight and a longer part, including ambient measurements at the ground.

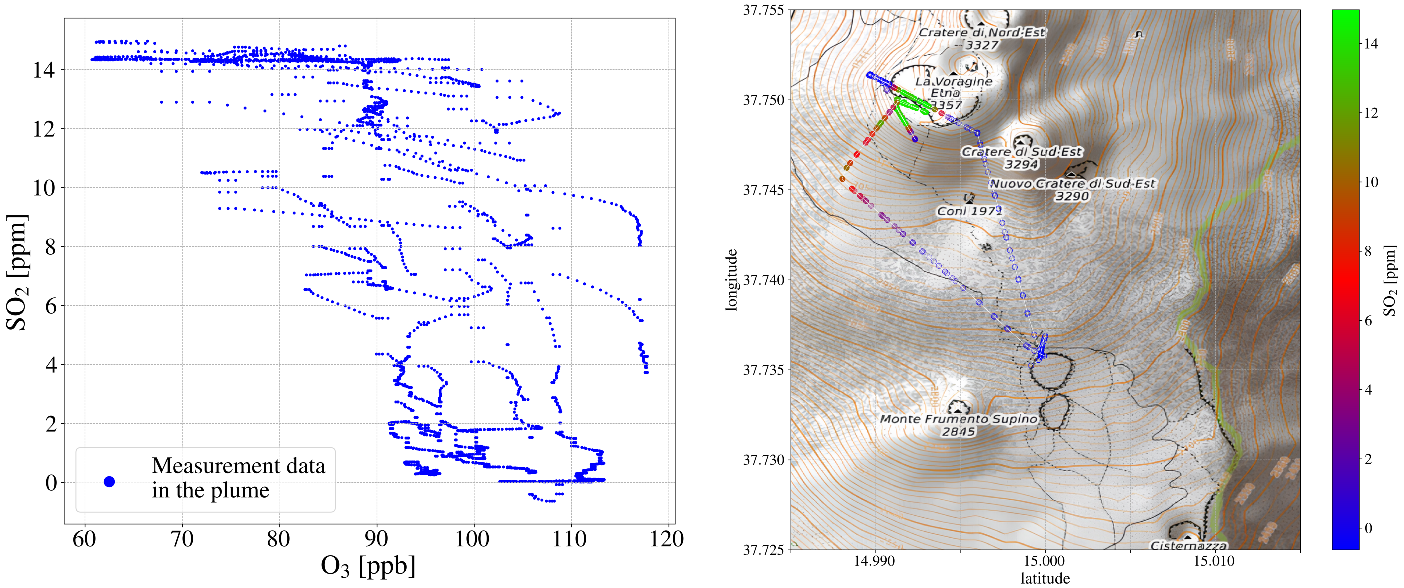

(b) Correlation plot for O_3 and SO_2, from the period of the flight. The correlation coefficient is -0.67.

(c) Map plot showing the flight route as well as the corresponding SO_2 values, indicating where the plume is. Map data: © OpenStreetMap contributors, SRTM | Map display: © OpenTopoMap (CC-BY-SA)

Figure 42: Plume measurement on 18.06.2023, sampling the BN plume with starting point at Torre del Filosofo.

9. Calculation: Ozone depletion in volcanic plumes

This section revisits the rough calculation presented in Rüth (2021), which shows that when considering the commonly used reactions to explain the O_3 depletion, a decrease in O_3 levels of only 1% compared to ambient levels should occur. Here, in particular the needed alterations to the assumption are presented to explain an O_3 depletion of around 40%. Firstly, however, a short recap of the existing calculation and its assumptions is shown.

The basic idea of the calculation is to compare the O_3 destruction R caused by reactive bromine chemistry inside volcanic plumes with the flux of ambient O_3 into the plume F. For this exercise the following assumptions are made:

- Parametrisation of the plume with a simple two box model,

$$A = 2\pi \cdot \left(r - \frac{\Delta r}{2}\right) \cdot \Delta s, \qquad (105)$$

$$V = \pi \cdot (r - \Delta r)^2 \cdot \Delta s., \qquad (106)$$

  where A is the surface area of the plume trough which the influx takes place, V is the volume of the inner plume, Δr is the width of the outer plume, r is the total radius of the plume, Δs is the width of the plume.

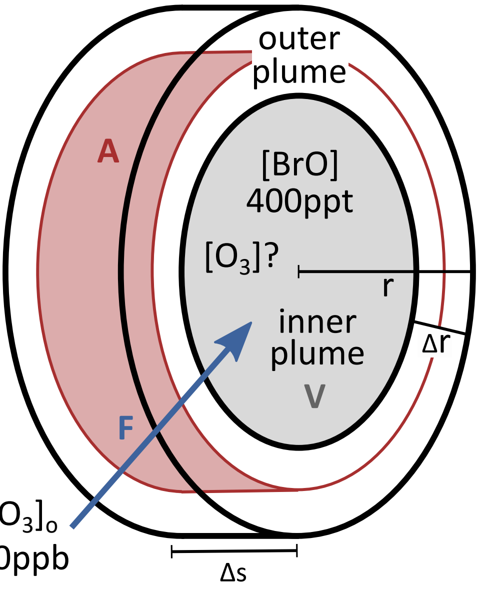

- Young plume (Plume age ≈ 2 min), with the following parameters:

$$r = 50\,\mathrm{m}$$
$$\Delta r = 20\,\mathrm{m}$$
$$\Delta s = 10\,\mathrm{m}$$

- O_3 depletion is only due to bromine species.
  ⇒ Destruction rate can be estimated with the BrO self reaction, as this is the rate limiting reaction in the reaction cycle (see Sec. 2, Reac. 1 to Reac. 10),

$$\frac{d[O_3]}{dt} = k_{O_3+Br} \cdot [O_3] \cdot [Br] \approx 2 \cdot k_{BrO+BrO} \cdot [BrO]^2 \qquad (107)$$

$$\Rightarrow \text{Rate of } O_3 \text{ destruction } R = \frac{d[O_3]}{dt} \cdot V \text{ [molec/s]}. \qquad (108)$$

- Influx of O_3 into the plume is determined by turbulent diffusion.
  ⇒ Ficks first law with turbulent diffusion constant is used as parametrisation,

$$O_3 \text{ flux: } j = K_t \cdot \frac{\Delta c_{O_3}}{\Delta r} \qquad (109)$$

$$\Rightarrow O_3 \text{ flow: } F = j \cdot A, \qquad (110)$$

where K_t is the turbulent diffusion constant, Δc_{O_3} is the concentration difference of O_3 between the inner plume and the surrounding atmosphere, $\frac{\Delta c_{O_3}}{\Delta r}$ is therefore the concentration gradient of O_3 in the outer plume and A is again the surface area of the plume through which the influx of O_3 takes place.

- Typical mixing ratios x_i, concentrations c_i (conversion from the mixing ratio to concentration using the ideal gas law) and weather conditions at Etna, summit elevation ~3300 m:

$$\begin{aligned} x_{O_3} = 80\,\text{ppb} \Rightarrow c_{O_3} &= [O_3] = 1.93 \times 10^{22}\,\tfrac{1}{\text{cm}^3}, \\ x_{\text{BrO}} = 400\,\text{ppt} \Rightarrow c_{\text{BrO}} &= [\text{BrO}] = 9.65 \times 10^{9}\,\tfrac{1}{\text{cm}^3} \\ \text{wind velocity: } v_p &= 10\,\tfrac{\text{m}}{\text{s}} \\ \text{turbulent diffusion constant: } K_t &= 10\,\tfrac{\text{m}^2}{\text{s}} \end{aligned}$$

- Steady state is assumed, meaning that the concentrations remain constant throughout the considered period.

For a local, stable O_3 depletion in the plume, the O_3 flow into the plume F cannot exceed the bromine-catalysed O_3 destruction R, otherwise the depletion would immediately be counterbalanced. From the destruction therefore the maximal flow of O_3 into the plume can be estimated, which is directly dependent on the O_3 concentration gradient inside the outer plume slice. From the flow then the O_3 concentration difference can be inferred. In the following the ideas are formulated in forms of equations:

$$F \overset{!}{=} R \tag{111}$$

$$K_t \cdot \frac{\Delta c_{O_3}}{\Delta r} \cdot A = 2 \cdot k_{\text{BrO+BrO}} \cdot [\text{BrO}]^2 \cdot V \tag{112}$$

$$\Rightarrow \Delta c_{O_3} = \frac{R \cdot \Delta r}{K_t \cdot A} = \frac{1.6 \times 10^{19}\,\frac{1}{\text{s}} \cdot 20\,\text{m}}{10\,\text{m}^2\text{s}^{-1} \cdot 2.5 \times 10^{7}\,\text{cm}^2} \tag{113}$$

$$\approx 1.3 \times 10^{10}\,\frac{1}{\text{cm}^3} \tag{114}$$

$$\Rightarrow \frac{\Delta c_{O_3}}{[O_3]} = \frac{1.3 \times 10^{10}\,\frac{1}{\text{cm}^3}}{1 \times 10^{12}\,\frac{1}{\text{cm}^3}} = 1.3\% \tag{115}$$

This is obviously a contradiction to the measurements presented in the previous section, Sec. 8.3. The measurements we presented there show an O_3 depletion of up to 60%. This raises the question which assumptions or part of the calculation is not a good description of reality. Possible ideas are:

- The turbulent diffusion is slower than anticipated or the parametrisation of it is not applicable in this case.
- The parametrisation of the plume is not representative of reality.
- Significantly more BrO is inside the plume leading to a stronger O_3 depletion.
- Other reaction mechanisms are responsible for the observed O_3 depletion (e.g. other halogen reaction cycles).

Lets first consider the question how slow the flow of O_3 into the plume has to be, or how much lower the turbulent diffusion constant must be, in order to explain an O_3 depletion of 40% while not changing the assumption about the destruction inside the plume. For this we will reformulate Eqn. 112,

$$K_{t,\text{required}} = 2 \cdot k_{\text{BrO+BrO}} \cdot [\text{BrO}]^2 \cdot V \cdot \frac{\Delta r}{\Delta c} \cdot \frac{1}{A} \approx 0.22\,\tfrac{\text{m}^2}{\text{s}} \tag{116}$$

$$\Rightarrow \frac{K_{t,\text{required}}}{K_{t,\text{assumed}}} = 0.022 \tag{117}$$

The required turbulent diffusion constant is only 2% of the turbulent diffusion constant which is commonly assumed in such scenarios. However, comparing this to the molecular diffusion constant $D \approx 0.19\,\frac{\text{cm}^2}{\text{s}} = 0.19 \times 10^{-4}\,\frac{\text{m}^2}{\text{s}}$ (for 20 °C of air) (Roedel and Wagner, 2017), we see that the required K_t is still 4 orders of magnitude larger.

Now lets consider the required BrO concentration to explain the observed O_3 depletion of 40%. From Eqn. 112, we can solve for the required BrO concentration,

$$[\text{BrO}]_{\text{required}} = \sqrt{\frac{K_t \cdot \frac{\Delta c}{\Delta r} \cdot A}{2k_{\text{BrO+BrO}} \cdot V}} \approx 6.55 \times 10^{10}\,\tfrac{1}{\text{cm}^3} \tag{118}$$

$$\Rightarrow x_{\text{BrO,required}} = 2.71\,\text{ppb} \tag{119}$$

$$\Rightarrow \frac{x_{\text{BrO,required}}}{x_{\text{BrO,measured}}} = 6.8 \tag{120}$$

This shows that the required BrO level must be significantly larger than measured. Since the BrO values are however determined using multi-axis differential optical absorption spectroscopy (MAX-DOAS) these values represent only mean BrO values as the measured quantity is the total amount of BrO in the considered column (see e.g. Bobrowski et al., 2003). By assuming a uniform distribution of BrO in the plume, the typical values of $x_{\text{BrO}} = 400\,\text{ppt}$ are obtained. However, a non-homogeneous distribution of BrO in the plume is very likely. This assumption allows for the existence of high BrO levels in smaller part of the plume in which the mixing ratio might reach the required values for an O_3 depletion to occur.
Furthermore, in particular in the young plume (plume age $< 4\,\text{min}$), mean BrO values of up to $(1.35 \pm 0.45)\,\text{ppb}$ have been found (Gliß et al., 2015). Compared to these values the required BrO values are not unrealistically high.

Another approach of explaining the observed O_3 depletion is considering further halogens, which is plausible. There have been measurements of IO (Schönhardt et al., 2017) and also ClO and OClO (Bobrowski et al., 2007; Gliß et al., 2015) in volcanic plumes. The relevant reactions for an O_3 depletion including iodine and chlorine are the following (see Platt and Janssen, 1995; Schmitt, 2016; Burkholder et al., 2019):

Destruction:

$$Br + O_3 \longrightarrow BrO + O_2 \qquad k_{O_3+BrO} = 1.2 \times 10^{-12}\,\frac{cm^3}{s} \tag{121}$$

$$I + O_3 \longrightarrow IO + O_2 \qquad k_{O_3+IO} = 1.2 \times 10^{-12}\,\frac{cm^3}{s} \tag{122}$$

$$Cl + O_3 \longrightarrow ClO + O_2 \qquad k_{O_3+ClO} = 1.2 \times 10^{-11}\,\frac{cm^3}{s} \tag{123}$$

Recycling:

$$BrO + BrO \longrightarrow products \qquad k_{BrO+BrO} = 3.2 \times 10^{-12}\,\frac{cm^3}{s} \tag{124}$$

$$\longrightarrow 2\,Br + O_2 \qquad k_{BrO+BrO,1} = 2.7 \times 10^{-12}\,\frac{cm^3}{s} \tag{125}$$

$$\longrightarrow Br_2 + O_2 \qquad k_{BrO+BrO,2} = 4.8 \times 10^{-13}\,\frac{cm^3}{s} \tag{126}$$

$$BrO + IO \longrightarrow products \qquad k_{BrO+IO} = 6.9 \times 10^{-11}\,\frac{cm^3}{s} \tag{127}$$

$$IO + IO \longrightarrow products \qquad k_{IO+IO} = 8 \times 10^{-11}\,\frac{cm^3}{s} \tag{128}$$

$$\longrightarrow I + OIO(\sim 40\%) \tag{129}$$

$$\longrightarrow I_2O_2(46\%) \tag{130}$$

$$BrO + ClO \longrightarrow Br + OClO \qquad k_{BrO+ClO,1} = 6.0 \times 10^{-12}\,\frac{cm^3}{s} \tag{131}$$

$$\longrightarrow Br + ClOO \qquad k_{BrO+ClO,2} = 5.5 \times 10^{-12}\,\frac{cm^3}{s} \tag{132}$$

$$\longrightarrow BrCl + O_2 \qquad k_{BrO+ClO,3} = 1.1 \times 10^{-12}\,\frac{cm^3}{s} \tag{133}$$

$$IO + ClO \longrightarrow products \qquad k_{IO+ClO} = 1.3 \times 10^{-11}\,\frac{cm^3}{s} \tag{134}$$

In this analysis, the self-reaction of ClO is not considered due to its relatively slow rate ($k_{ClO+ClO} \approx 1 \times 10^{-14}\,\frac{cm^3}{s}$) and the fact that it does not immediately produce atomic Cl and therefore does not immediately contribute to the O_3 depletion.

For the sake of simplicity, we assume that each recycling reaction generates two halogen radicals capable of destroying one O_3 molecule each.
This assumption is particularly tenuous for the IO self-reaction, as the further reactions of the resulting I_2O_2 are uncertain. However, there is the possibility that photolysis yields I_2 and O_2, thereby by further photolysis producing two I radicals. Additionally, we assume prompt production of Cl radicals from rapid thermal decay of ClOO, though this is not strictly accurate. These simplifications are only some of the several others made in this model, and there are significant uncertainties regarding the entire reaction mechanism as the reactions involving IO, ClO, and BrO are not yet fully studied. The calculation here should not be seen as an accurate representation of reality but rather serve to establish a lower bound for the concentration of reactive halogen species required to account for an O_3 depletion of approximately 40%.

For iodine and chlorine the rate-limiting steps are, similarly to bromine, also the recycling reactions, even if the their recycling reactions take place much faster. The determining variable is not the speed of the individual reactions but the turnover rate. Given that O_3 is present in much higher concentrations than the reactive halogen species, the destruction reaction has a much higher turnover rate compared to the recycling reactions. Therefore the destruction of O_3 by all halogens in the plume can be approximated by the turnover rates of the recycling reaction,

$$\begin{aligned}\frac{d[\mathrm{O_3}]}{dt} &\approx 2 \cdot k_{\mathrm{BrO+BrO}} \cdot [\mathrm{BrO}]^2 + 2 \cdot k_{\mathrm{IO+IO}} \cdot [\mathrm{IO}]^2 + 2 \cdot k_{\mathrm{BrO+IO}} \cdot [\mathrm{BrO}][\mathrm{IO}] \\ &\quad + 2 \cdot k_{\mathrm{BrO+ClO}} \cdot [\mathrm{BrO}][\mathrm{ClO}] + 2 \cdot k_{\mathrm{IO+ClO}} \cdot [\mathrm{IO}][\mathrm{ClO}] \qquad (135)\end{aligned}$$

only IO and BrO:

$$\frac{d[\mathrm{O_3}]}{dt} \approx 2k_{\mathrm{BrO+BrO}}[\mathrm{BrO}]^2 + 2k_{\mathrm{IO+IO}}[\mathrm{IO}]^2 + 2k_{\mathrm{BrO+IO}}[\mathrm{BrO}][\mathrm{IO}] \qquad (136)$$

$$\Rightarrow [\mathrm{IO}] = \frac{k_{\mathrm{BrO+IO}}[\mathrm{BrO}]}{2k_{\mathrm{IO+IO}}} + \left\{ \left(\frac{k_{\mathrm{BrO+BrO}}[\mathrm{BrO}]}{2k_{\mathrm{IO+IO}}} \right)^2 - \frac{k_{\mathrm{BrO+BrO}}[\mathrm{BrO}]^2}{k_{\mathrm{IO+IO}}} \right. \qquad (137)$$

$$\left. + \frac{1}{2k_{\mathrm{IO+IO}}} \cdot \frac{d[\mathrm{O_3}]}{dt} \right\}^{1/2} \qquad (138)$$

$$= 1.4 \times 10^{10} \, \frac{1}{\mathrm{cm^3}}$$

$$\Rightarrow x_{\mathrm{IO}} = 0.58\,\mathrm{ppt} \qquad (139)$$

only ClO and BrO: assume $k_{\mathrm{BrO+ClO}} = k_{\mathrm{BrO+ClO,1}} + k_{\mathrm{BrO+ClO,3}}$

$$\frac{d[\mathrm{O_3}]}{dt} \approx 2 \cdot k_{\mathrm{BrO+BrO}} \cdot [\mathrm{BrO}]^2 + 2 \cdot k_{\mathrm{BrO+ClO}} \cdot [\mathrm{BrO}][\mathrm{ClO}] \qquad (140)$$

$$\Rightarrow [\mathrm{ClO}] = \left(\frac{d[\mathrm{O_3}]}{dt} - 2 \cdot k_{\mathrm{BrO+BrO}} \cdot [\mathrm{BrO}]^2 \right) \cdot \frac{1}{2 \cdot k_{\mathrm{BrO+ClO}} \cdot [\mathrm{BrO}]} \qquad (141)$$

$$= 9.6 \times 10^{10} \, \frac{1}{\mathrm{cm^3}}$$

$$\Rightarrow x_{\mathrm{ClO}} = 4.0\,\mathrm{ppt} \qquad (142)$$

using: $$\frac{d[\mathrm{O_3}]}{dt} = \frac{F}{V} = \frac{K_t \cdot \frac{\Delta c}{\Delta r} \cdot A}{V} \qquad (143)$$

Here, the required IO as well as the required ClO is determined by just looking at the contributions involving IO and ClO, respectively.

Rüdiger et al. (2021) analysed the ratios of total iodine (I) and chlorine (Cl) to total sulphur (S) in the plume of Masaya volcano, Nicaragua. I/S and Cl/S ratios were approximately ∼6×10^{-5} and ∼0.7, respectively. Assuming the total sulphur equal to the measured SO_2 (4 ppm using a Multi-GAS instrument), total iodine and chlorine are estimated at 0.24 ppt and 2.8 ppm. While the required ClO is less than total Cl, the necessary IO is twice the total iodine. However, higher SO_2 mixing ratios (up to tens of ppm) have been found in volcanic plumes. If twice as much SO_2 in the plume is assumed, a total of 8 ppm, the total iodine matches the required IO mixing ratio. Complete conversion of total iodine to IO is unlikely, but this comparison shows that the magnitude of IO is plausible.

With the assumptions and calculations presented an O_3 depletion can be explained. Some of these assumptions are more or less plausible. However, it is unlikely that a single factor is solely responsible; rather, a combination of the discussed mechanisms might contribute to the depletion. Additionally, since the explanations provided are not exhaustive, other mechanisms could also play a role in the local O_3 depletion.

10. Conclusions and Discussion

In the framework of this thesis, a new version of the CL O_3 monitor was constructed. This new monitor is both, smaller and lighter than the previous one, weighing only 1500 g and with dimensions of 38 x 20 x 11cm (compared to 10 kg and dimensions of 40 x 30 x 18.7cm). This corresponds to a reduction in weight of 85% and in volume of around 60%. These improvements can be largely attributed to (1) the use of a modern PMT with build-in high-voltage generation and divider, which is significantly lighter and smaller and has simpler readout electronics, and (2) a lightweight foam housing, compared to an aluminium base plate in the first version. Additionally, a significant reduction in power consumption was achieved, by nearly a factor of 10, from ∼30 W to 3 W. This can be mainly attributed to the fact that the modern PMT is operated without temperature stabilisation.

Calibration and ambient measurements in Heidelberg, as well as measurements in the field, showed the monitor's capability to measure O_3. While signal corrections are imperative for deducing the O_3 mixing ratio, a detection limit of around 1.5 ppb and a measurement accuracy of around 7% for 40 ppb O_3 ($\approx$ 2.8 ppb) were accomplished, with a response time of $\tau_{\mathrm{exp},1/e} = 2.00 \pm 0.04 \pm 0.04\,\mathrm{s}$.

Signal post-processing is needed since (1) the temperature dependent dark current has to be corrected for, and (2) to correct the measured O_3 signal for changes in the ambient parameters. These include the ambient pressure, ambient temperature and C_2H_4 pressure. In this thesis we showed that a dark current correction is possible (Sec. 5.1). However, this correction is challenging. Here we have seen that a hysteresis effect exists, and fast changes in the ambient temperature can also lead to sudden changes in the dark current, which cannot be corrected fully since the temperature measured at the PMT housing does not show this fast change. Therefore, post-correcting the dark current introduces an uncertainty of only $\sim 0.5\,\mathrm{mV} \hat{\approx} 1\,\mathrm{ppb}$ into the measurement.
The second reason for post-processing is due to the signals further dependencies. The signal strength can change by about 50% - in either direction - when ambient parameters are changed in a range that is observed in the measurements (see Sec. 3.2.3). During a single measurement significant changes in ambient parameters are usually not observed, however C_2H_4 pressure changes significantly even during a single measurement. Additionally, during drone-based measurements also ambient pressure changes significantly. In between different measurements even more severe changes in the ambient parameters are seen, comparing measurements conducted at Etna at an elevation of 3000 m with measurements done in Heidelberg is only possible with this post-processing. During the calibration procedure it became particularly apparent that the conversion factor is needed. The difference between converted signal and measured signal is well visible in the calibration plots. No generally valid calibration factor can be determined without the conversion. The conversion factor used results from the theoretical description of the O_3-C_2H_4 reaction. In a comparison between theory and experiment we have found that the theoretical description can describe the experiential observations sufficiently well. Deviations mainly arise from the 'airglow' signal which is not accounted for in the theory.

This 'airglow' phenomenon is the signal that can be observed when no C_2H_4 is admitted to the measurement cell. This is unexpected since, in theory, there shouldn't be any signal without the injection of C_2H_4 (after correcting the dark current). From a series of experiments conducted to characterise the phenomenon the following conclusions can be drawn:

- The signal is (somewhat) correlated with O_3 levels (during the day).
- The signal is also observable during night.
- The decrease in the signal within the room takes place with similar decay times to that of O_3. For both signals, 'airglow' and O_3, a 28 min decay time have been measured.
- The decrease of the 'airglow' signal within the measurement cell shows a decay time of around 18 s. For O_3 the decay time is 6 s. The O_3 decay time is most likely reduced as C_2H_4 is further available, even when the pumps is switched off, leading to a faster destruction of O_3 compared to the 'airglow'.
- Measurements using an O_3 generator were performed, during these measurements we saw that the 'airglow' signal is proportional to the generated O_3 mixing ratio. The 'airglow' signal ranges from only ~7% up to ~80% with a mean of 15% of the measured O_3 mixing ratio (determined from the fit for the 'airglow' calibration) .
- Rough calculations suggest that the signal cannot be observed with the naked eye, even during night.

The main uncertainty contributions to the signal are due to the inherent noise of the signal, contributing with a relative uncertainty of ~ 5%, the uncertainty of the conversion factor, with a relative uncertainty of ~ 4%, and the uncertainty associated with the dark current, ~ 5% relative uncertainty for a signal resulting from roughly 40 ppb. In particular the quantification of the uncertainty arising from the conversion factor proved to be difficult. Here we decided, to quantify the uncertainty as a relative uncertainty, that is derived from the comparison of the theoretical to the experimental signal (see Sec. 5.3). The uncertainty arising from the 'airglow' signal is not included explicitly. However, its contribution is included in the contribution from the conversion factor.
The derived accuracy and characteristics of the monitor are sufficient to measure O_3 under nearly all imaginable conditions. During the ground based measurements in Heidelberg as well as drone-based O_3 measurements, the measured O_3 mixing ratio with the CL O_3 monitor did correspond well to comparative measurements from a series of different monitors, showing deviations to the comparative measurements within 2σ. The achieved accuracy is also sufficient to make statements about the O_3 levels inside volcanic plumes. During field measurements at Etna in June 2023, the monitor was mounted on a drone and flown through the volcanic plume. O_3 depletions inside the plume of up to 60% loss compared to ambient levels were measured. The simultaneous use of a MultiGAS instrument made it possible to distinguish plume gases from ambient air without volcanic gases. The measurements show an anti-correlation between SO_2 and O_3, in line with results from other studies. The correlation coefficients are between -0.45 to -0.75.

However, we faced some challenges, during drone-based measurements, particularly concerning the monitor's aerodynamic properties when mounted on a drone. Notably, one rotor overheated even during brief flights. This might be related to the weight distribution of the monitor, however it is much more likely that this problem is related to the area under the rotor that is occupied by the monitor. With this the rotor under which most of the monitor is placed has to work harder in order to generate the same uplift leading to overheating. This emphasises the need to further minimise the size, in particular adapt the surface area, and weight of the monitor to improve stability during flights.

An interesting challenge, of scientific nature, is explaining the drop in O_3 levels inside the volcanic plume. The existing approximating calculation for which the destruction of O_3

inside the plume is compared to the influx of O_3 into the plume fails to account for this O_3 depletion. To match the findings of O_3 depletion of around 40%, this calculation is revisited. One possible adjustment factor is the mixing dynamics. The O_3 influx into the plume must be significantly smaller than anticipated, with a turbulent diffusion constant of roughly $0.22\,\frac{\mathrm{m}^2}{\mathrm{s}}$. The other possible explanation is that O_3 destruction rates are larger than assumed. When assuming BrO levels of about $x_{\mathrm{BrO}} = 2.71\,\mathrm{ppb}$ an O_3 depletion of 50% can be explained. This value is comparatively high, however during MAX-DOAS at Etna Gliß et al. (2015) found mean BrO values of up to $(1.35 \pm 0.45)\,\mathrm{ppb}$. Further assuming inhomogeneities in the BrO levels, the required bro mixing ratio is plausible.
Another possibility for the observed depletion is the presence of other halogens. Assuming additionally to bromine species either iodine or chlorine species, we have seen that around $x_{\mathrm{IO}} = 0.6\,\mathrm{ppt}$ or $x_{\mathrm{ClO}} = 4\,\mathrm{ppt}$ are needed. While these are relatively high values, the order of magnitude is plausible.

11. Outlook

As became clear in the thesis and the discussion, there is still room for further refinements of the monitor.
Improvements of the CL O_3 monitor should focus on further reducing size and weight, in particular improving the aerodynamic properties and the weight distribution. This need became apparent during the drone measurements. The largest components are the PMT, the teflon aerosol filter and the C_2H_4 Minican. Using a smaller aerosol filter would reduce weight and size significantly. The Minican itself is voluminous but quite lightweight, however the Minican adapter is particularly heavy. A custom made adapter might solve this problem.
Another idea is to explore different gases, which might lead to a better photon yield of the luminescence and may also present an opportunity to further compact the design. For this trimethylethylene and tetramethylethylene might be used, which show an increased emission intensity compared to that of the C_2H_4-O_3 reaction by a factor of 50 (Pitts Jr et al., 1971). Tetramethylethylene (C_6H_{12}) is a liquid at room temperature and has a vapour pressure of around 185 mbar (ChemSpider, 2023). Storing the reactant in the liquid phase would significantly reduce the volume of the monitor without reducing the amount of reactant available. With the vapour pressure of 185 mbar, C_6H_{12} is available with a mixing ratio of $\frac{185}{1013} \approx 18\%$. If the C_6H_{12} flow is set to around 10% of the total flow, C_6H_{12} could also be supplied to the measurement cell with a mixing ratio of $\sim 2\%$ (this is the mean mixing ratio of C_2H_4 in the current setup).

Incorporating a printed circuit board (PCB) would make the monitor more robust and reduce the chances of connection issues. But there's a trade-off: while a PCB makes the device more reliable, it also makes it less flexible to changes. Altering a PCB-integrated design would necessitate printing an entirely new board, making it a good choice only if subsequent adjustments are considered unlikely.

To fully answer the question on O_3 distributions in volcanic plumes, a more comprehensive measurement campaign is essential. For this firstly more measurements at Etna should be conducted. In a more long-term goal, it would be worthwhile to study other volcanoes to get a more complete picture. It would be interesting to examine further high halogen emitting volcanos (additionally to Etna), such as Soufriere Hills and Ambrym as well as rather low halogen emitting volcanos, including the Hawaiian volcanoes (such as Kilauea and Mauna Loa), or Copahue. With this a more comprehensive understanding on halogen plume chemistry could be reached.

Additionally, the ‘airglow’ signal has to be further quantified. The cause of the signal is still unclear, and so it remains an unsolved challenge to explain it. Possible experiments include the use of artificial air in combination with an O_3 generator. Using this approach, the possible reactants can be narrowed down. Another idea is to use a scrubber which is more selective to O_3. For this purpose Manganese dioxide/copper oxide catalyst could be used. If the ‘airglow’ signal is (or is not) observable using these scrubbers might provide further insights into the relevant reactions.
Additionally, measuring the spectrum of the ‘airglow’ might prove beneficial. To minimise the influence of unwanted light sources the measurement should be conducted during a new moon night in an area with only little light pollution. From the spectrum further insights into the possible reactants might be gained.

References

2B Technologies: Operation manual Model POM, URL `https://www.google.com/url?sa=t&rct=j&q=&esrc=s&source=web&cd=&ved=2ahUKEwj-ytKClv3sAhWInaQKHQceDSAQFjAAegQIBRAC&url=https%3A%2F%2Ftwobtech.com%2Fdocs%2Fmanuals%2Fmodel_POM_revC.pdf&usg=AOvVaw139xnrxUS9hme7gd2yQL2u`, 2B Technologies, 2020.

Aletter, D.: Bedienungsanleitung in Kurzform; Immissions Ozonmonitor für Messungen in Vulkan Rauchfahnen (Prototyp 1), mLW Messtechnik für Luft und Wasserreinhaltung, 2020.

Atkinson, R., Baulch, D. L., Cox, R. A., Crowley, J. N., Hampson, R. F., Hynes, R. G., Jenkin, M. E., Rossi, M. J., Troe, J., and Subcommittee, I.: Evaluated kinetic and photochemical data for atmospheric chemistry: Volume II, gas phase reactions of organic species, Atmospheric Chemistry and Physics, 6, 3625–4055, https://doi.org/10.5194/acp-6-3625-2006, URL `https://acp.copernicus.org/articles/6/3625/2006/`, 2006.

Baicker, J. A.: Dark Current in Photomultipliers, IRE Transactions on Nuclear Science, 7, 74–80, https://doi.org/10.1109/TNS2.1960.4315741, 1960.

Barnes, I. and McGrath, W.: The chemiluminescent reaction of ozone with ketene, Journal of Photochemistry, 33, 137 – 143, https://doi.org/https://doi.org/10.1016/0047-2670(86)87028-9, URL `http://www.sciencedirect.com/science/article/pii/0047267086870289`, 1986.

Barrie, L. and Platt, U.: Arctic tropospheric chemistry: an overview, Tellus B: Chemical and Physical Meteorology, 49, 450–454, https://doi.org/10.3402/tellusb.v49i5.15984, URL `https://doi.org/10.3402/tellusb.v49i5.15984`, 1997.

Bobrowski, N. and Platt, U.: SO2/BrO ratios studied in five volcanic plumes, Journal of Volcanology and Geothermal Research, 166, 147 – 160, https://doi.org/https://doi.org/10.1016/j.jvolgeores.2007.07.003, URL `http://www.sciencedirect.com/science/article/pii/S037702730700220X`, 2007.

Bobrowski, N., Hönninger, G., Galle, B., and Platt, U.: Detection of bromine monoxide in a volcanic plume, Nature, 423, 273 – 276, https://doi.org/https://doi.org/10.1038/nature01625, 2003.

Bobrowski, N., von Glasow, R., Aiuppa, A., Inguaggiato, S., Louban, I., Ibrahim, O. W., and Platt, U.: Reactive halogen chemistry in volcanic plumes, Journal of Geophysical Research: Atmospheres, 112, https://doi.org/https://doi.org/10.1029/2006JD007206, URL `https://agupubs.onlinelibrary.wiley.com/doi/abs/10.1029/2006JD007206`, 2007.

Bobrowski, N., Held, A., Platt, U., Rüdiger, J., Schmitt, S., Wittmer, J., Bednorz, A., and Einhorn, A.: Final report for Research Project Reaktive Halogene in einer simulierten Vulkanfahne, 2020.

Branca, S. and Del Carlo, P.: Eruptions of Mt. Etna During the Past 3,200 Years: a Revised Compilation Integrating the Historical and Stratigraphic Records, pp. 1–27, American Geophysical Union (AGU), https://doi.org/https://doi.org/10.1029/143GM02, URL `https://agupubs.onlinelibrary.wiley.com/doi/abs/10.1029/143GM02`, 2004.

Branca, S., Coltelli, M., and Groppelli, G.: Geological Evolution of Etna Volcano, pp. 49–63, American Geophysical Union (AGU), https://doi.org/https://doi.org/10.1029/143GM04, URL `https://agupubs.onlinelibrary.wiley.com/doi/abs/10.1029/143GM04`, 2004.

Bräutigam, E.: Construction of an Airborne Chemiluminescence Ozone Monitor for Volcanic Plumes, https://doi.org/10.11588/heidok.00032085, 2022.

Burkholder, J. B., Sander, S. P., Abbatt, J., Barker, J. R., Cappa, C., Crounse, J. D., Dibble, T. S., Huie, R. E., Kolb, C. E., Kurylo, M. J., Orkin, V. L., Percival, C. J., Wilmouth, D. M., and Wine, P. H.: Chemical Kinetics and Photochemical Data for Use in Atmospheric Studies, Evaluation No. 19, JPL Publication 19-5, URL http://jpldataeval.jpl.nasa.gov, 2019.

Calabrese, S., Aiuppa, A., Allard, P., Bagnato, E., Bellomo, S., Brusca, L., DAlessandro, W., and Parello, F.: Atmospheric sources and sinks of volcanogenic elements in a basaltic volcano (Etna, Italy), Geochimica et Cosmochimica Acta, 75, 7401–7425, https://doi.org/10.1016/j.gca.2011.09.040, URL https://linkinghub.elsevier.com/retrieve/pii/S0016703711005618, 2011.

Carn, S. A., Froyd, K. D., Anderson, B. E., Wennberg, P., Crounse, J., Spencer, K., Dibb, J. E., Krotkov, N. A., Browell, E. V., Hair, J. W., Diskin, G., Sachse, G., and Vay, S. A.: In situ measurements of tropospheric volcanic plumes in Ecuador and Colombia during TC4, Journal of Geophysical Research: Atmospheres, 116, https://doi.org/https://doi.org/10.1029/2010JD014718, URL https://agupubs.onlinelibrary.wiley.com/doi/abs/10.1029/2010JD014718, 2011.

Carn, S. A., Fioletov, V. E., McLinden, C. A., Li, C., and Krotkov, N. A.: A decade of global volcanic SO2 emissions measured from space, Scientific Reports, 7, 44 095, https://doi.org/10.1038/srep44095, URL https://www.nature.com/articles/srep44095, 2017.

ChemSpider: Tetramethylethylene, ChemSpider ID: 10776, URL http://www.chemspider.com/Chemical-Structure.10776.html, molecular Formula: C_6H_{12}. Average mass: 84.160 Da. Monoisotopic mass: 84.093903 Da., 2023.

Delmelle, P.: Environmental impacts of tropospheric volcanic gas plumes, Geological Society, London, Special Publications, 213, 381–399, https://doi.org/10.1144/GSL.SP.2003.213.01.23, URL https://www.lyellcollection.org/doi/10.1144/GSL.SP.2003.213.01.23, 2003.

Deutscher Wetterdient (DWD): Open Data, URL https://opendata.dwd.de/climate_environment/CDC/observations_germany/climate/hourly/, accessed: 2023-04-09, 2023.

Finlayson, B. J., Pitts, J. N., and Atkinson, R.: Low-pressure gas-phase ozone-olefin reactions. Chemiluminescence, kinetics, and mechanisms, Journal of the American Chemical Society, 96, 5356–5367, https://doi.org/10.1021/ja00824a009, URL https://doi.org/10.1021/ja00824a009, 1974.

General, S., Bobrowski, N., Pöhler, D., Weber, K., Fischer, C., and Platt, U.: Airborne I-DOAS measurements at Mt. Etna: BrO and OClO evolution in the plume, Journal of Volcanology and Geothermal Research, 300, 175–186, https://doi.org/10.1016/j.jvolgeores.2014.05.012, URL https://linkinghub.elsevier.com/retrieve/pii/S0377027314001541, 2015.

Gliß, J., Bobrowski, N., Vogel, L., Pöhler, D., and Platt, U.: OClO and BrO observations in the volcanic plume of Mt. Etna implications on the chemistry of chlorine and bromine species in volcanic plumes, Atmospheric Chemistry and Physics, 15, 5659–5681, https://doi.org/10.5194/acp-15-5659-2015, URL https://acp.copernicus.org/articles/15/5659/2015/, 2015.

Gold, V., ed.: The IUPAC Compendium of Chemical Terminology: The Gold Book, International Union of Pure and Applied Chemistry (IUPAC), Research Triangle Park, NC, 4 edn., https://doi.org/10.1351/goldbook, URL https://goldbook.iupac.org/, 2019.

Hergert, E.: Photomultiplier tubes count photons, Laser Focus World, 33, 129–135, URL https://api.semanticscholar.org/CorpusID:115060071, 1997.

Hessisches Landesamt für Naturschutz, Umwelt und Geologie (HLNUG): Messdatenportal, URL https://www.hlnug.de/messwerte/datenportal/messstelle/2/1/0675/15, accessed: 2023-04-09, 2023.

Hobbs, P. V., Tuell, J. P., Hegg, D. A., Radke, L. F., and Eltgroth, M. W.: Particles and gases in the emissions from the 19801981 volcanic eruptions of Mt. St. Helens, Journal of Geophysical Research: Oceans, 87, 11 062–11 086, https://doi.org/https://doi.org/10.1029/JC087iC13p11062, URL https://agupubs.onlinelibrary.wiley.com/doi/abs/10.1029/JC087iC13p11062, 1982.

INGV National Institute of Geophysics and Volcanology: Bollettino Settimanale sul monitoraggio multiparametrico del vulcano Vulcano del 13/06/2023, URL https://www.ct.ingv.it/index.php/monitoraggio-e-sorveglianza/prodotti-del-monitoraggio/bollettini-settimanali-multidisciplinari/787-bollettino-Settimanale-sul-monitoraggio-vulcanico-geochimico-e-sismico-del-vulcano-Et file, 2023a.

INGV National Institute of Geophysics and Volcanology: Bollettino Settimanale sul monitoraggio multiparametrico del vulcano Vulcano del 20/06/2023, URL https://www.ct.ingv.it/index.php/monitoraggio-e-sorveglianza/prodotti-del-monitoraggio/bollettini-settimanali-multidisciplinari/790-bollettino-Settimanale-sul-monitoraggio-vulcanico-geochimico-e-sismico-del-vulcano-Et file, 2023b.

Jourdain, L., Roberts, T. J., Pirre, M., and Josse, B.: Modeling the reactive halogen plume from Ambrym and its impact on the troposphere with the CCATT-BRAMS mesoscale model, Atmospheric Chemistry and Physics, 16, 12 099–12 125, https://doi.org/10.5194/acp-16-12099-2016, URL https://acp.copernicus.org/articles/16/12099/2016/, 2016.

Karbach, N., Bobrowski, N., and Hoffmann, T.: Observing volcanoes with drones: studies of volcanic plume chemistry with ultralight sensor systems, Scientific Reports, 12, 17 890, https://doi.org/10.1038/s41598-022-21935-5, URL https://www.nature.com/articles/s41598-022-21935-5, 2022.

Kelly, P. J., Kern, C., Roberts, T. J., Lopez, T., Werner, C., and Aiuppa, A.: Rapid chemical evolution of tropospheric volcanic emissions from Redoubt Volcano, Alaska, based on observations of ozone and halogen-containing gases, Journal of Volcanology and Geothermal Research, 259, 317 – 333, https://doi.org/https://doi.org/10.1016/j.jvolgeores.2012.04.023, URL http://www.sciencedirect.com/science/article/pii/S0377027312001230, the 2009 Eruption of Redoubt Volcano, Alaska, 2013.

Kern, C., Sihler, H., Vogel, L., Rivera, C., Herrera, M., and Platt, U.: Halogen oxide measurements at Masaya Volcano, Nicaragua using active long path differential optical absorption spectroscopy, Bulletin of Volcanology, 71, 659–670, https://doi.org/10.1007/s00445-008-0252-8, 2009.

Kissick, D. J., Muir, R. D., and Simpson, G. J.: Statistical Treatment of Photon/Electron Counting: Extending the Linear Dynamic Range from the Dark Count Rate to Saturation, Analytical Chemistry, 82, 10 129–10 134, https://doi.org/10.1021/ac102219c, URL https://doi.org/10.1021/ac102219c, 2010.

Kleindienst, T. E., Hudgens, E. E., Smith, D. F., McElroy, F. F., and Bufalini, J. J.: Comparison of Chemiluminescence and Ultraviolet Ozone Monitor Responses in the Presence of Humidity and Photochemical Pollutants, Air & Waste, 43, 213–222, https://doi.org/10.1080/1073161X.1993.10467128, URL https://doi.org/10.1080/1073161X.1993.10467128, 1993.

Kleinschmitt, C., Boucher, O., and Platt, U.: Sensitivity of the radiative forcing by stratospheric sulfur geoengineering to the amount and strategy of the SO<sub>2</sub>injection studied with the LMDZ-S3A model, Atmospheric Chemistry and Physics, 18, 2769–2786, https://doi.org/10.5194/acp-18-2769-2018, URL https://acp.copernicus.org/articles/18/2769/2018/, 2018.

Kuhn, J., Bobrowski, N., and Platt, U.: The Interface Between Magma and Earth's Atmosphere, Geochemistry, Geophysics, Geosystems, 23, e2022GC010 671, https://doi.org/10.1029/2022GC010671, URL https://agupubs.onlinelibrary.wiley.com/doi/10.1029/2022GC010671, 2022.

Leston, A. R., Ollison, W. M., Spicer, C. W., and Satola, J.: Potential Interference Bias in Ozone Standard Compliance Monitoring, Journal of the Air & Waste Management Association, 55, 1464–1472, https://doi.org/10.1080/10473289.2005.10464749, URL https://doi.org/10.1080/10473289.2005.10464749, pMID: 28086057, 2005.

LUBW Landesanstalt für Umwelt Baden-Württemberg: Umweltinformationssystem (UIS), Daten- und Kartendienst, URL https://udo.lubw.baden-wuerttemberg.de/public/pages/home/index.xhtml, accessed: 2023-04-09, 2023.

Nederbragt, G. W., Van Der Horst, A., and Van Duijn, J.: Rapid Ozone Determination Near an Accelerator, Nature, 206, 87–87, https://doi.org/10.1038/206087a0, URL https://www.nature.com/articles/206087a0, 1965.

Olzmann, M., Kraka, E., Cremer, D., Gutbrod, R., and Andersson, S.: Energetics, Kinetics, and Product Distributions of the Reactions of Ozone with Ethene and 2,3-Dimethyl-2-butene, The Journal of Physical Chemistry A, 101, 9421–9429, https://doi.org/10.1021/jp971663e, URL https://doi.org/10.1021/jp971663e, 1997.

O'Neal, H. E. and Blumstein, C.: A new mechanism for gas phase ozoneolefin reactions, International Journal of Chemical Kinetics, 5, 397–413, https://doi.org/https://doi.org/10.1002/kin.550050310, URL https://onlinelibrary.wiley.com/doi/abs/10.1002/kin.550050310, 1973.

Photonis: Photomultiplier tube basics, URL https://psec.uchicago.edu/library/photomultipliers/Photonis_PMT_basics.pdf, n.d.

Pitts Jr, J., Kummer, W., and Steer, R.: Chemiluminescent reactions of ozone with olefins and sulfides, Environmental Science & Technology, 5, 1045–1047, 1971.

Platt, U. and Bobrowski, N.: Quantification of volcanic reactive halogen emissions, p. 115132, Cambridge University Press, https://doi.org/10.1017/CBO9781107415683.011, 2015.

Platt, U. and Janssen, C.: Observation and role of the free radicals NO3, ClO, BrO and IO in the troposphere, Faraday Discussions, 100, 175, https://doi.org/10.1039/fd9950000175, URL http://xlink.rsc.org/?DOI=fd9950000175, 1995.

Pryor, S. and Steyn, D.: Hebdomadal and diurnal cycles in ozone time series from the Lower Fraser Valley, B.C., Atmospheric Environment, 29, 1007–1019, https://doi.org/https://doi.org/10.1016/1352-2310(94)00365-R, URL https://www.sciencedirect.com/science/article/pii/135223109400365R, 1995.

Rüdiger, J., Gutmann, A., Bobrowski, N., Liotta, M., De Moor, J. M., Sander, R., Dinger, F., Tirpitz, J.-L., Ibarra, M., Saballos, A., Martínez, M., Mendoza, E., Ferrufino, A., Stix, J., Valdés, J., Castro, J. M., and Hoffmann, T.: Halogen activation in the plume of Masaya volcano: field observations and box model investigations, Atmospheric Chemistry and Physics, 21, 3371–3393, https://doi.org/10.5194/acp-21-3371-2021, URL https://acp.copernicus.org/articles/21/3371/2021/, 2021.

Roberts, T. J.: Ozone Depletion in Tropospheric Volcanic Plumes: From Halogen-Poor to Halogen-Rich Emissions, Geosciences, 8, https://doi.org/10.3390/geosciences8020068, URL https://www.mdpi.com/2076-3263/8/2/68, 2018.

Robock, A.: Volcanic eruptions and climate, Reviews of Geophysics, 38, 191–219, https://doi.org/https://doi.org/10.1029/1998RG000054, URL https://agupubs.onlinelibrary.wiley.com/doi/abs/10.1029/1998RG000054, 2000.

Roedel, W. and Wagner, T.: Physik unserer Umwelt: Die Atmosphäre, Springer Spektrum, Berlin, Heidelberg, https://doi.org/https://doi.org/10.1007/978-3-662-54258-3, 2017.

Rüth, M.: Characterisation of a chemiluminescence ozone monitor for volcanic applications, https://doi.org/10.11588/heidok.00029947, 2021.

Schmincke, H.-U.: Vulkanismus, WBG (Wiss. Buchges.), Darmstadt, 4., unveränd. aufl edn., 2013.

Schmitt, S.: The Dynamics of Reactive Halogen Species at the Dead Sea Valley, https://doi.org/10.11588/heidok.00020245, URL https://archiv.ub.uni-heidelberg.de/volltextserver/20245/1/Diss_SSchmitt_20160104_toRefereesTitleCorr_compressed.pdf, 2016.

Schönhardt, A., Richter, A., Theys, N., and Burrows, J. P.: Space-based observation of volcanic iodine monoxide, Atmospheric Chemistry and Physics, 17, 4857–4870, https://doi.org/10.5194/acp-17-4857-2017, URL https://acp.copernicus.org/articles/17/4857/2017/, 2017.

Surl, L., Donohoue, D., Aiuppa, A., Bobrowski, N., and von Glasow, R.: Quantification of the depletion of ozone in the plume of Mount Etna, Atmospheric Chemistry and Physics, 15, 2613–2628, https://doi.org/10.5194/acp-15-2613-2015, URL https://acp.copernicus.org/articles/15/2613/2015/, 2015.

Textor, C., Graf, H.-F., Timmreck, C., and Robock, A.: Emissions from volcanoes, in: Emissions of Atmospheric Trace Compounds, edited by Granier, C., Artaxo, P., and Reeves, C. E., pp. 269–303, Springer Netherlands, Dordrecht, 2004.

Vance, A., McGonigle, A. J. S., Aiuppa, A., Stith, J. L., Turnbull, K., and von Glasow, R.: Ozone depletion in tropospheric volcanic plumes, Geophysical Research Letters, 37, https://doi.org/https://doi.org/10.1029/2010GL044997, URL https://agupubs.onlinelibrary.wiley.com/doi/abs/10.1029/2010GL044997, 2010.

von Glasow, R.: Atmospheric chemistry in volcanic plumes, Proceedings of the National Academy of Sciences, 107, 6594–6599, https://doi.org/10.1073/pnas.0913164107, URL https://www.pnas.org/content/107/15/6594, 2010.

von Glasow, R., Bobrowski, N., and Kern, C.: The effects of volcanic eruptions on atmospheric chemistry, Chemical Geology, 263, 131 – 142, https://doi.org/https://doi.org/10.1016/j.chemgeo.2008.08.020, URL http://www.sciencedirect.com/science/article/pii/S0009254108003756, halogens in Volcanic Systems and Their Environmental Impacts, 2009.

Warnach, S.: Bromine monoxide in volcanic plumes - A global survey of volcanic plume composition and chemistry derived from Sentinel-5 Precursor/TROPOMI data, https://doi.org/10.11588/heidok.00031910, URL http://www.ub.uni-heidelberg.de/archiv/31910, 2022.

Warren, G. J. and Babcock, G.: Portable Ethylene Chemiluminescence Ozone Monitor, Review of Scientific Instruments, 41, 280–282, 1970.

Wennberg, P.: Atmospheric chemistry: Bromine explosion, Nature, 397, 299–301, 1999.

Williams, E. J., Fehsenfeld, F. C., Jobson, B. T., Kuster, W. C., Goldan, P. D., Stutz, J., and McClenny, W. A.: Comparison of Ultraviolet Absorbance, Chemiluminescence, and DOAS Instruments for Ambient Ozone Monitoring, Environmental Science & Technology, 40, 5755–5762, https://doi.org/10.1021/es0523542, URL https://doi.org/10.1021/es0523542, pMID: 17007137, 2006.

Wißdorf, W., Müller, D., Brachthäuser, Y., Langner, M., Derpmann, V., Klopotowski, S., Polaczek, C., Kersten, H., Brockmann, K., and Benter, T.: Gas Flow Dynamics in Inlet Capillaries: Evidence for non Laminar Conditions, Journal of the American Society for Mass Spectrometry, 27, 1550–1563, https://doi.org/10.1007/s13361-016-1415-z, URL https://pubs.acs.org/doi/10.1007/s13361-016-1415-z, 2016.

Zahn, A., Weppner, J., Widmann, H., Schlote-Holubek, K., Burger, B., Kühner, T., and Franke, H.: A fast and precise chemiluminescence ozone detector for eddy flux and airborne application, Atmospheric Measurement Techniques, 5, 363–375, https://doi.org/10.5194/amt-5-363-2012, URL https://amt.copernicus.org/articles/5/363/2012/, 2012.

Appendices

A. Additional information on the characterisation

A.1. Additional calibration plots

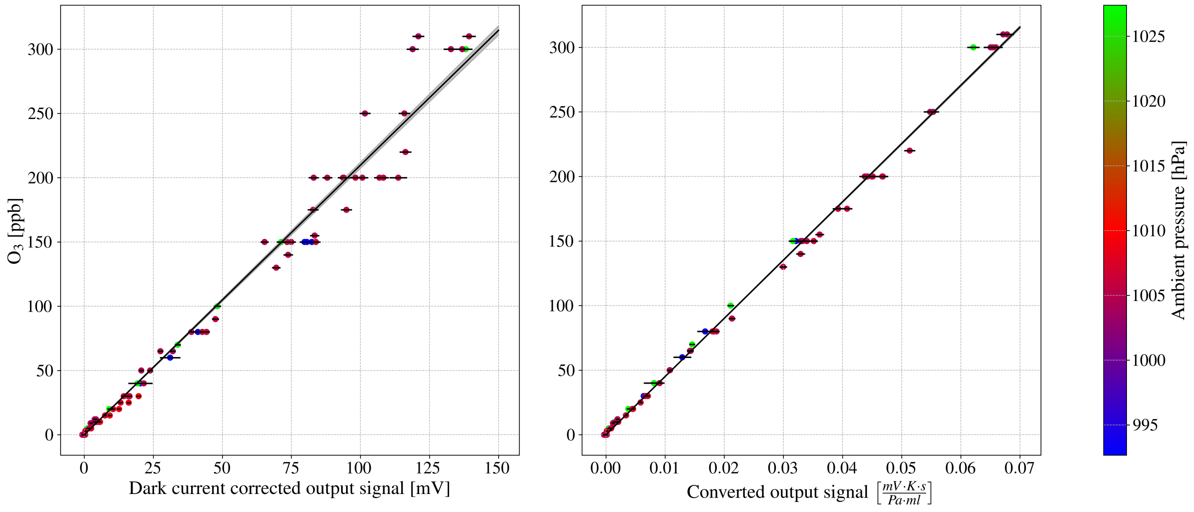

(a) The data points are colour coded according to ambient pressure p.

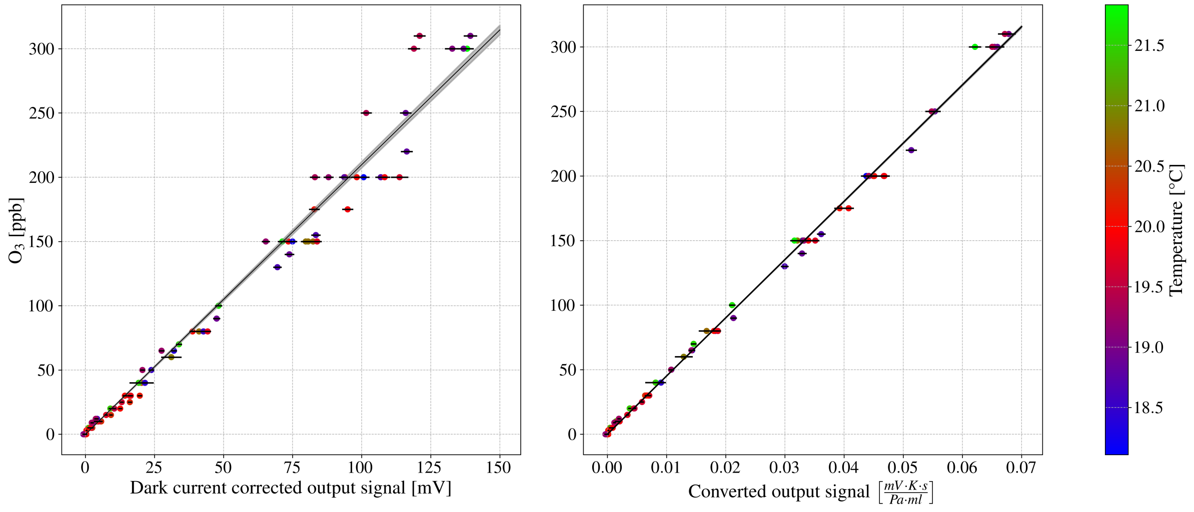

(b) The data points are colour coded according to ambient temperature T.

Figure 43: Calibration plot of the CL O$_3$ monitor. To obtain the data points, the signal is averaged over the periods of constant O$_3$ mixing ratios, the uncertainty is given by the standard deviation. The colour of the data points indicates the respective ambient pressure p (a), or temperature T (b). On the right side, the calibration plot with the dark current corrected signal is shown. Strong deviations from the calibration fit can be seen in the data points. After the conversion, on the left side, the calibration curve fits the data points significantly better. It can be seen that these two parameters have a significantly smaller influence on the signal compared to $p_{C_2H_4}$.

A.2. Varying ambient pressure

Here, the additional measurements studying the effect of varying ambient pressure on the signal are shown. These measurements are conducted while diving up and down the flanks of Etna, with the O_3 generator is powered trough the car battery. Applying the conversion factor decreases the influence of ambient pressure, the calculated O_3 mixing ratio does show less change during the course of the measurement compared to the PMT signal. However, in particular in Fig. 44b the O_3 mixing ratio shows still deviations of around 10 ppb during the measurement. This is however, most likely not cause by changes in the ambient pressure, since the simultaneous pressure measurement does not show similar characteristic at that time. It is more likely caused by the O_3 generator not producing reliable O_3 mixing ratios in the car.

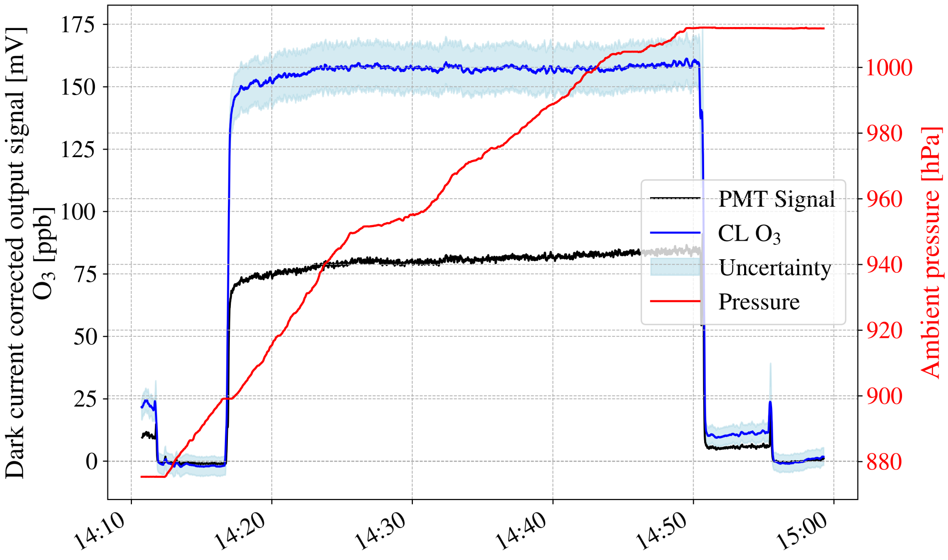

(a)

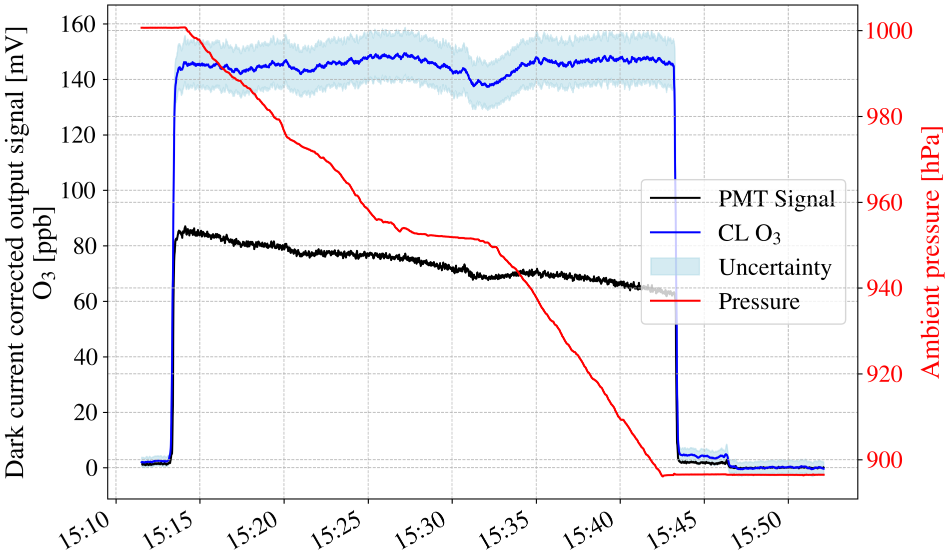

(b)

Figure 44: Influence of changing ambient pressure on the signal. Once the PMT signal as it is recorded is shown as well as the calculated O_3 mixing ratio. This shows that the signal indeed changes with the ambient pressure, applying the calibration reduced this dependence.

B. Additional O_3 measurements

Here, additional drone based measurements are depicted.
The Measurement in Heidelberg, Germany (Fig. 45a) is conducted in the Handschuhsheimer Feld, an agricultural area close to the University Heidelberg on 23.05.2023. The high uncertainty in the beginning of the measurement is obtained as during this time the C_2H_4 Minican is not opened, and therefore the calculation of the uncertainty breaks down.
The second measurement is a drone-based measurement conducted at the north-eastern flank of Etna, at Piano Provenzana at a starting altitude of ~1810 m on 07.06.2023.

During both measurements the O_3 mixing ratio increases with height, as it is expected. The higher O_3 mixing ratio at Piano Provenzana can likely be mainly attributed to the higher starting altitude. However, the change in location as well the local weather conditions can also play a role.

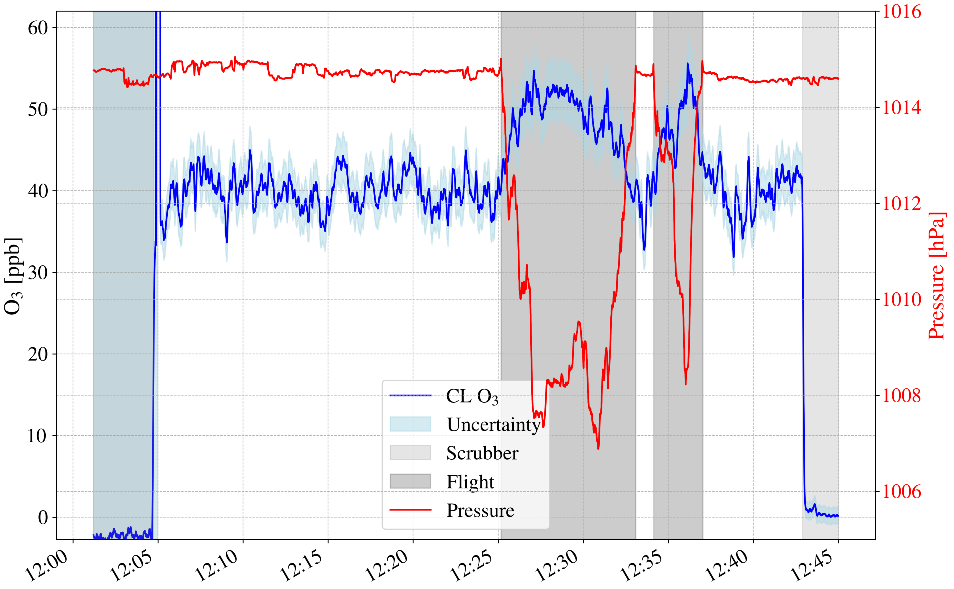

(a) Measurement in the Handschuhsheimer Feld, Heidelberg, Germany on 23.05.2023.

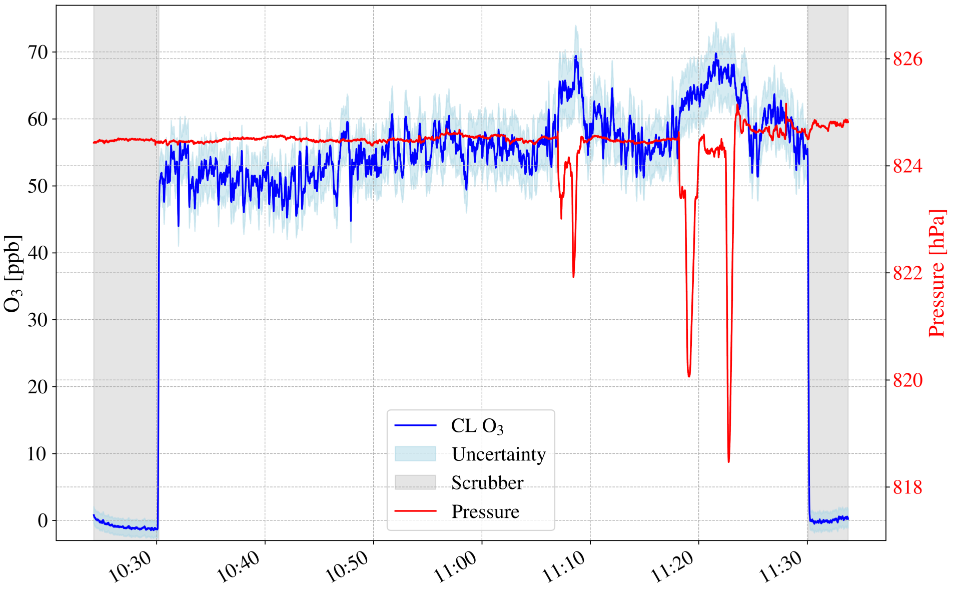

(b) Measurement at Piano Provenzana, Etna, Italy on 07.06.2023.

Figure 45: Additional drone based measurements.

C. Additional technical information

C.1. Circuit board and wiring diagrams

In this section the circuit board which is used in the monitor is shown and the components labelled. The data sheets of the coponents can be found in the nest section, Appendix. C.2. Additionally the wiring diagram is shown.

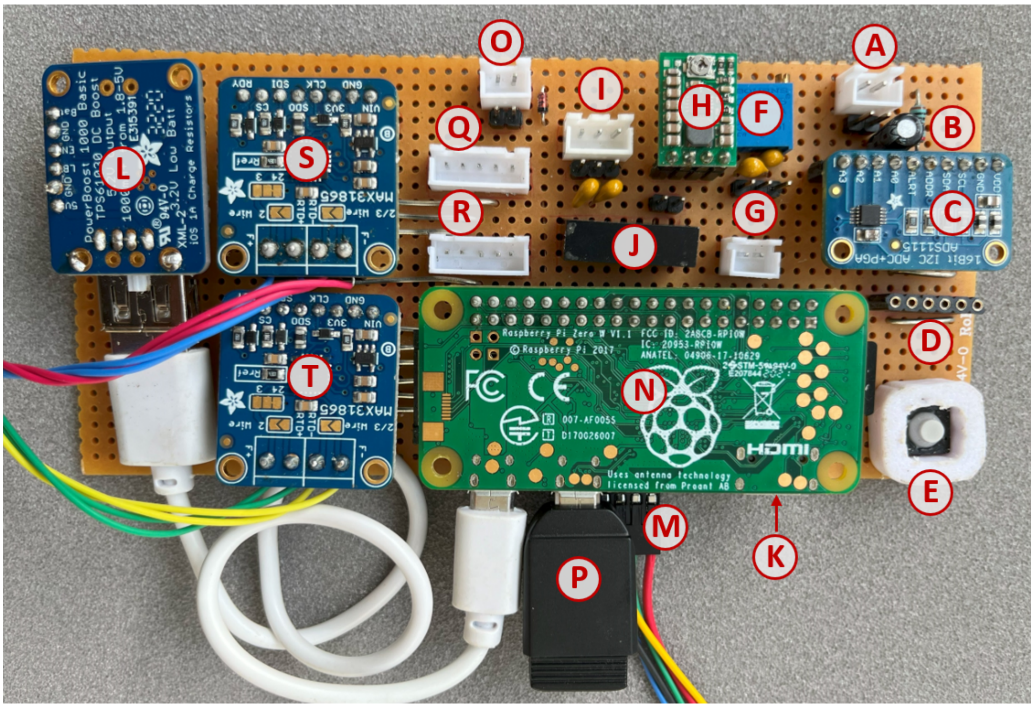

A	Plug-in connection PMT output
B	Integrator
C	ADC
D	Plug-in connection ambient sensor
E	Power-off button
F	Potentiometer
G	Control voltage PMT
H	Step down converter pump
I	Plug-in connection PMT power supply
J	DC power supply PMT
K	Plug-in connection GPS
L	Powerboost
M	Plug-in connection display
N	Raspberry Pi Zero computer
O	Plug-in connection pump
P	USB Stick
Q	Pressure sensor before capillary
R	Pressure sensor Minican
S	PT1000 temperature sensor PMT
T	PT1000 temperature sensor pump

Figure 46: Circuit board with the individual components.

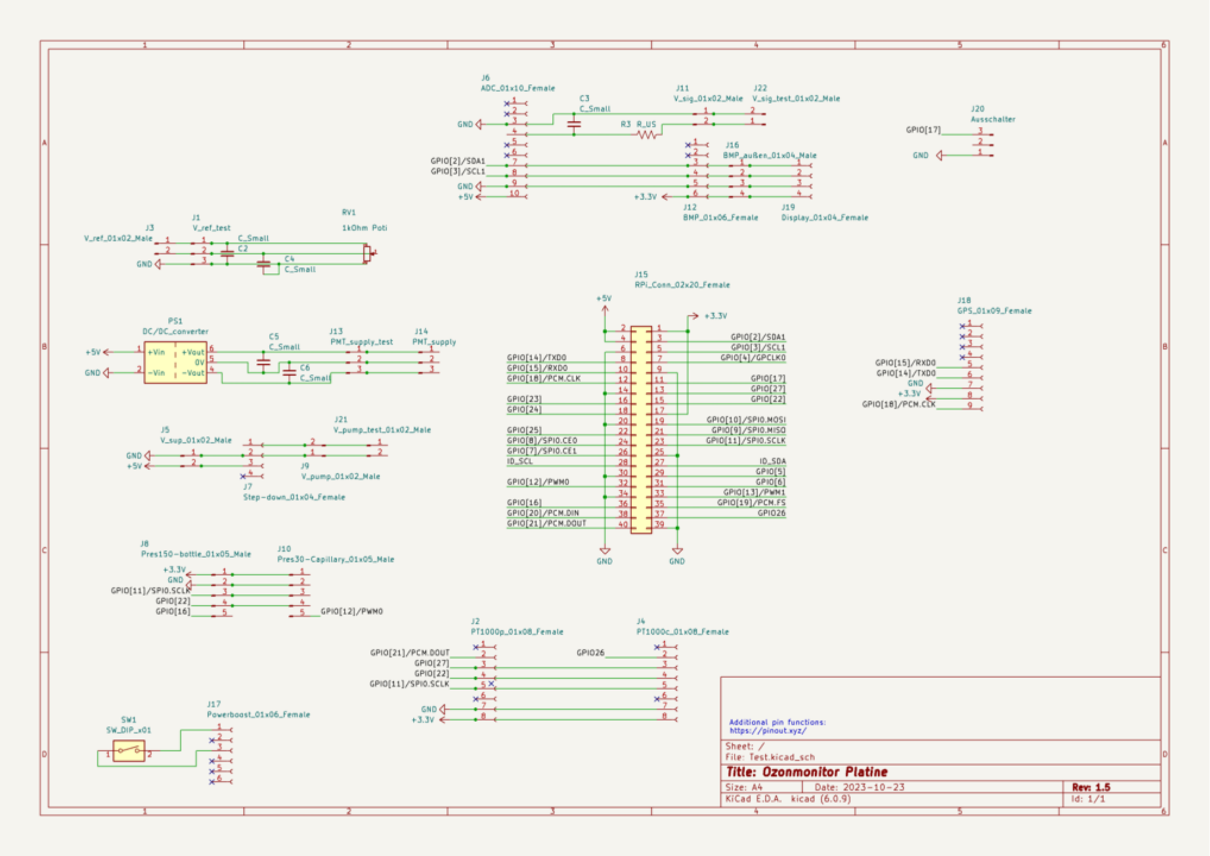

Figure 47: Wiring diagram of the circuit diagram.

C.2. Construction elements with data sheets

(visited on 2023-09-29)

Photosensor Module H10493-001 from Hamamatsu Photonics GmbH
http://www.hamamatsu.com/content/dam/hamamatsu-photonics/sites/documents/99_SALES_LIBRARY/etd/m-h10493e.pdf

Rotary vane pump model G 6/01-K-LC 1 from Thomas by Gardner Denver
http://www.usathomas.com/assets/images/Rotary_vane_mini_pumps-2.pdf(page 3)

Mini pressure regulator model 638.42 from filcom and HUG-technik
https://www.filcom-technik.de/media/catalog/download/de/wartungsgeraete/Technische_Daten_Mini_Druckregler_00045278_0.pdf

Raspberry Pi Zero
https://www.raspberrypi.com/documentation/computers/raspberry-pi.html

Adafruit PiOLED display - 128x32 Mini OLED for Raspberry Pi
https://learn.adafruit.com/adafruit-pioled-128x32-mini-oled-for-raspberry-pi

Pressure sensor ABPDANV150PGSA3 and ABPDANV030PGSA3 from Honeywell
https://prod-edam.honeywell.com/content/dam/honeywell-edam/sps/siot/en-us/products/sensors/pressure-sensors/board-mount-pressure-sensors/basic-abp-series/documents/sps-siot-basic-board-mount-pressure-abp-series-datasheet-32305128-ciid-155789.pdf

Analog-to-digital-converter from Adafruit
https://learn.adafruit.com/adafruit-4-channel-adc-breakouts

PT1000 temperature sensor amplifier MAX31865 from Adafruit
https://learn.adafruit.com/adafruit-max31865-rtd-pt100-amplifier

Bosch BMP280 ambient pressure and temperature sensor, from Berrybase
https://www.berrybase.de/Pixelpdfdata/Articlepdf/id/6008/onumber/GY-BMP280

PowerBoost 1000 basic from Adafruit
https://learn.adafruit.com/adafruit-powerboost-1000-basic

Step-down converter (for pump) from Pololu
https://ecksteinimg.de/Datasheet/Pololu/PO2118.pdf

DC/DC-converter TMA 0515D (for PMT) from TracoPower
https://asset.conrad.com/media10/add/160267/c1/-/en/000154158DS02/datenblatt-154158-tracopower
pdf

Ultimate GPS module from Adafruit
https://learn.adafruit.com/adafruit-ultimate-gps/overview

Li-ion Battery ICR18650 4400mAh 3.7V
https://ecksteinimg.de/Datasheet/ZB07011/Datasheet.pdf

PE-Foam from Wulfmeyer
https://www.wulfmeyer.com/de/produkte/pe-pvdf-schaeume
https://www.wulfmeyer.com/fileadmin/downloads/publicfiles/MP15FR.pdf

PVC hardfoam plates Protex from Bauhaus
https://www.bauhaus.info/aluplatten-kunststoffplatten/hartschaumplatte-protex/p/14217624

C.3. Data logging software

As described in the text a Raspberry Pi is used to control and read out the different sensors. In the following the data logging software that is started on boot of the Raspberry Pi is shown.

```
## IMPORT NECESSERY LIBRARYS
# for reading out the the system time and date
import time
from datetime import datetime
# for writing directly csv-files (comma-seperated value)
import csv
# for acessing the serial interfaces of the RPi (SPI, I2C)
import board
# for the BMP280 ambient temperature and pressure sensor
from bmp280 import BMP280
try:
    from smbus2 import SMBus
except ImportError:
    from smbus import SMBus
#for the PT1000 (MAX31865)
import adafruit_max31865
import digitalio
#for the ADC (PMT read out) (ADS1115)
import busio
i2c = busio.I2C(board.SCL, board.SDA)
import adafruit_ads1x15.ads1115 as ADS
from adafruit_ads1x15.analog_in import AnalogIn
#for i2c display
import subprocess
from PIL import Image, ImageDraw, ImageFont
import adafruit_ssd1306
#for the Honeywell pressure sensors
import spidev #general purpuse SPI library
import RPi.GPIO as gpio #access to the GPIO pins (general purpos input output)

## INITIALSE THE SENSORS
# Initialise the BMP280
bus = SMBus(1)
bmp280 = BMP280(i2c_dev=bus)

# Initialise PT1000
spi = board.SPI()
# Choose which pin (PIN 21) is the Chip Select for the MAX31865 board.
cs = digitalio.DigitalInOut(board.D21)
cs2 = digitalio.DigitalInOut(board.D26)
# pass the set-up parameters of the PT1000
PT1000p = adafruit_max31865.MAX31865(spi, cs, wires=4, rtd_nominal=1000.0,
    ref_resistor=4300.0)
PT1000c = adafruit_max31865.MAX31865(spi, cs2, wires=4, rtd_nominal=1000.0,
    ref_resistor=4300.0)

# Initialise ADC
ads = ADS.ADS1115(i2c)
ads.gain = 16 # =1,2,4,8,16; specify gain for the programable gain amplifier
# define the channel in differential mode (with input pins 0 and 1)
chan_dif = AnalogIn(ads, ADS.P0, ADS.P1)
# additional channel in single mode, reading out the PMT signal wire directly
chan_ana = AnalogIn(ads, ADS.P0)

#Initialise i2c Display
# Create the SSD1306 OLED class, first two parameters are the pixel width and
    height
disp = adafruit_ssd1306.SSD1306_I2C(128, 32, i2c)
disp.fill(0)
disp.show()
width = disp.width # define the width as the width of the display
height = disp.height # define the height as the height of the display
image = Image.new('1', (width, height)) # create blank image
draw = ImageDraw.Draw(image) # get drawing object to draw on image
font = ImageFont.load_default() # load the font
padding = -2
top = padding
bottom = height - padding
x = 0

# Initialise pressure sensors
# The RPi has only 2 pins directly dedicated as chip selects for SPI, so the
# chip select (CS) pins for the pressure sensor are turned on and off manually
pin30 = 12 # CS-pin for 30psi pressure sensor
pin150 = 16 # CS-pin for 150psi pressure sensor
gpio.setup(pin30, gpio.OUT)
```

```
gpio.setup(pin150, gpio.OUT)
gpio.output(pin30, gpio.HIGH) # set the CS pins initally to high
gpio.output(pin150, gpio.HIGH)

P_spi=spidev.SpiDev() # initialize SPI bus for the pressure sensors
P_spi.open(0,0)       # SPI connection with bus 0 and CS-pin CE0 (= GPIO 8, pin
   24); this CS-pin is turned on and off, but no slave is connected there
P_spi.max_speed_hz = 15200

out_min = 1638
out_max = 14746
P_min = 0
# Define the funcions needed to read out the pressure sensors
def get_pressure(pin, P_max, correction = 0):
  gpio.output(pin, gpio.LOW) # set CS-pin low -> associated slave is adressed
  high, low = P_spi.xfer2([0,0]) # raw read out from the pressure sensor
  gpio.output(pin, gpio.HIGH) # set CS-pin high again -> stop adressing slave
  count = high*2**8+low # convert read out to number (between 0 and 2^14)
  # formula to convert output number to pressure (see chapter 3.4 M N)
  pressure = (count-out_min)*(P_max-P_min)/(out_max-out_min)+P_min-correction
  return pressure
def getP30():
  Pmax30 = 2068.43 #mbar, = 30 psi
    corr30 = 0
  pressure = get_pressure(pin30, Pmax30, corr30)
  return pressure
def getP150():
  Pmax150 = 10.3421 #bar, = 150 psi
    corr150 = 0
  pressure = get_pressure(pin150, Pmax150, corr150)
  return pressure

# open the file on the USB stick
# "a" - Append - Opens file for appending, creates the file if not existing
with open("/media/usbstick/ozon-daten.txt", "a", newline=’’) as f:
  # initialize the csv writer (with tabs between values)
  writer = csv.writer(f, delimiter=’\t’)
  writer.writerow([’datetime’, ’T_bmp’, ’P_bmp’, ’PT1000c’,’PT1000p’ ’V_dif’, ’
   V_A0’, ’P_30’, ’P_150’]) # write header line
  i = 0 # define counter and set it to 0
  #repeat as fast as possible until the program is interupted: read out all the
   sensors and write it into the file
  while (True):
    writer.writerow([datetime.now(),    # ISO-timestamp
      f’{bmp280.get_temperature():.3f}’,  # degree Celsius (ambient temperature)
      f’{bmp280.get_pressure():.3f}’,   # mbar (ambient pressure)
      f’{PT1000c.temperature:.2f}’,     # degree Celsius (temperature of PMT)
      f’{PT1000p.temperature:.2f}’,   # degree Celsius (temperature of pump)
      f’{chan_dif.voltage*1000:.2f}’,   # mV (readout of PMT, difference mode)
      f’{chan_ana.voltage*1000:.2f}’,   # mV (readout of PMT, single mode)
      f’{getP30():.1f}’,      # mbar (pressure in front of capillary)
      f’{getP150():.4f}’])      # bar (pressure in the minican)
    f.flush() # update file, otherwise data gets lost when program is interupted

    i = i+1
    # update display at every 18th run (roughly every 3s), wirting data to
   display is comparatively slow,
    # doing it only sporadically allows to keep the intervals between reading
   out the sensors as short as possible
    if i % 18 == 0:
      image = Image.new(’1’, (width,height)) # create new image onto which to
   write data
      draw = ImageDraw.Draw(image)
      # write data to image
      draw.text((x,top+0), ’ O3=’ + f’{chan_dif.voltage*1000:.2f}’,font = font,
   fill = 255) # O3 value [mV]
      draw.text((x,top+8), ’ P bottle =’ + f’{getP150():.2f}’,font = font, fill
   = 255) # pressure of ethen bottle [bar]
      draw.text((x,top+16), ’ P cap =’ + f’{getP30():.1f}’,font = font, fill =
   255) # pressur before capillary [mbar]
      draw.text((x,top+25), ’T c/p =’ + f’{PT1000c.temperature:.2f}/’+f’{PT1000p
   .temperature:.2f}’,font = font, fill = 255)
      # Temperature at the PMT/measurement cell (c) and the pump (p) [řC]

      # display the image
      disp.image(image)
      disp.show()
```

C.4. PMT output

In this section the PMT output is looked at in more detail. The measurements conducted with the oscilloscope are read in using Python to further analyse the data. With a spike counting algorithm the the spikes in the PMT output signal are counted in every $\frac{1}{3}$s period. In Fig. 48a the output voltage of the PMT and the RC integrator output is shown for a measurement with a total duration of 7 s. Additionally, the detected spikes are marked. Since the spikes are spaced so closely together, in Fig. 48b a zoom into a period of 15 ms is shown, in which the spikes can be distinguished from each other.

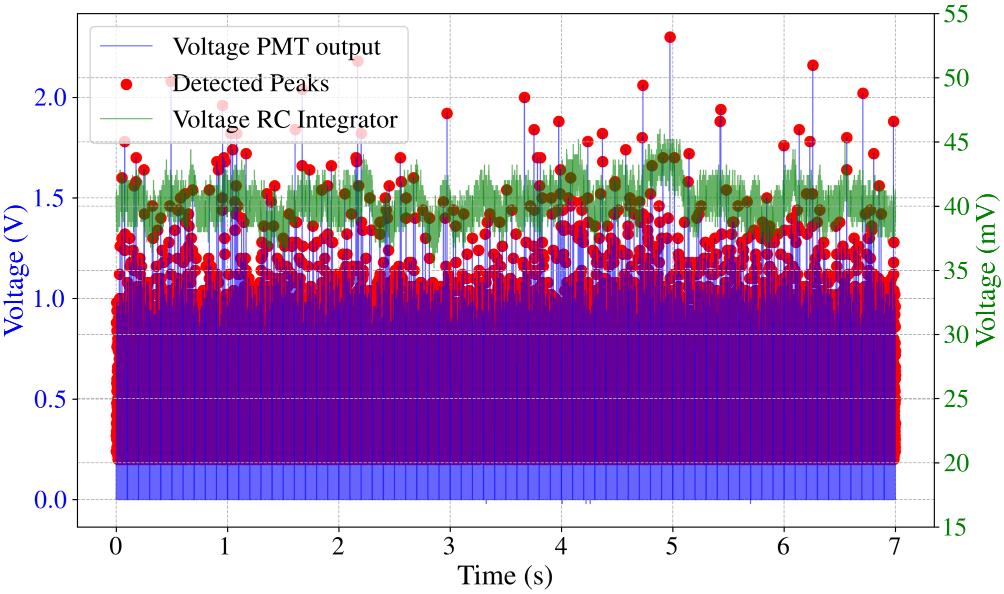

(a) Measurement of the PMT output over a total duration of 7 s. A total of 79,820 peaks are counted.

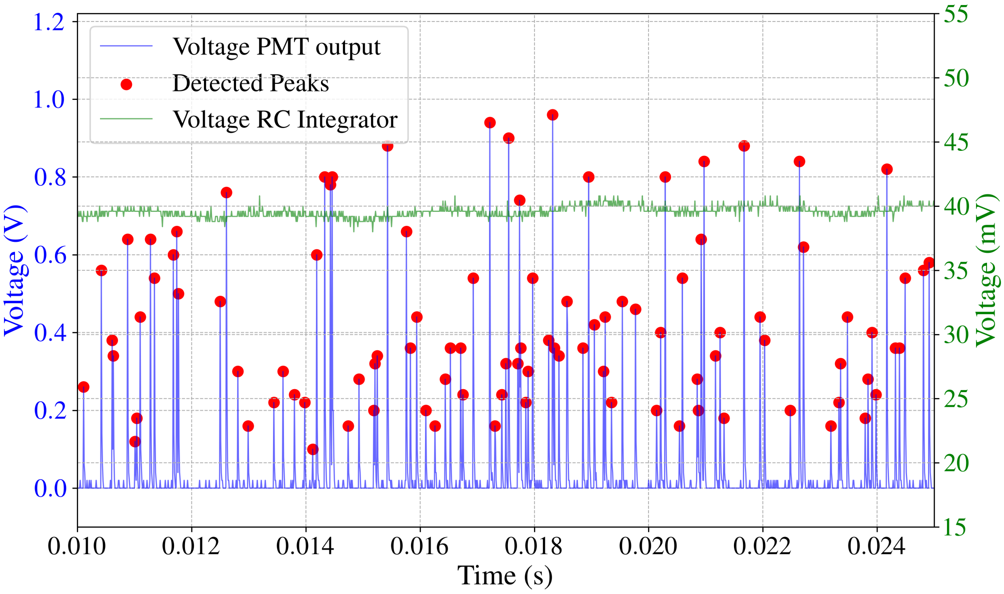

(b) Zoom into a smaller part of the measurement, showing a duration of ∼15 ms. It can be seen that the majority of peaks is reliably counted.

Figure 48: PMT output (blue) with the counted voltage peaks marked (red dots). Simultaneously the output voltage of the RC integrator is shown (green). The data is recorded using an oscilloscope and then analysed using a python.

From Fig. 48b we can see that the majority of spikes is detected reliably.

Additionally, a histogram of the spike heights is generated (see Fig. 49). One histogram shows the distribution of all spikes, Fig. 49a, whereas in the other the height distribution for the different light and O_3 conditions during the measurements are shown separately Fig. 49b. Here the different histograms are labelled according to the mean output voltage of the RC integrator. The higher the RC output voltage is the more photons hit the PMT.

The full distribution shows that most spikes have a height of around 0.3 V. Until a spike height of about 1 V, the number of spikes decreases steeply in an almost linear fashion. From a spike height of about 1 V the decrease in the number of spikes is strongly diminished and the distribution gradually tapers off at 1.75 V.

The separate histograms also show a similar characteristic. However, it becomes obvious that indeed not only the absolute number of spikes increases when more photons are measured but also the number of higher spikes increases. This might be related to several photons reaching the photo cathode simultaneously and therefore generating spikes of higher amplitude. If this is however, the only reason for the flattening of the curve when comparing the RC integrator output with the peak count (see Fig. 12a) is not possible to say with certainty.

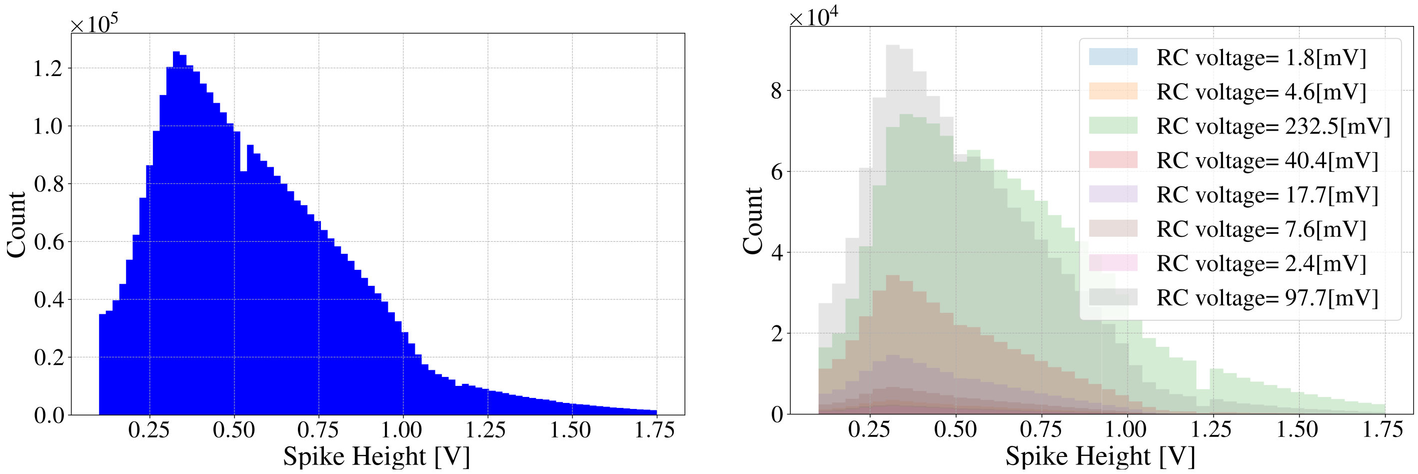

(a) Full histogram of spike heights of the PMT output.

(b) Histogram of spike heights of the PMT output in which the different light conditions are shown in different colours.

Figure 49: Histograms of the spike heights.

C.5. Characterisation of the integrator

In the setup of the monitor a passive RC integrator circuit is used to smooth the PMT signal before reading it out with the ADC and Raspberry Pi, as described in Sec. 4.2. The used RC integrator is characterised in the following.

For the resistor, R = 1 kΩ, and for the capacitance, C = 100 µF are chosen. With this the integrator circuit has a time constant of $\tau = \mathrm{R} \cdot \mathrm{C} = 1 \times 10^{3}\,\Omega \cdot 1 \times 10^{-4}\,\mathrm{F} = 1 \times 10^{-1}\,\mathrm{s}$. This is a reasonable choice since the flushing time of the reaction chamber, which limits the time resolution of the O_3 measurement, is 1 s (for more details on the response time of the monitor see Sec. 5.5) and 0.1 s is long compared to the duration of a spike (20 µs).

Fig. 50 shows the integrator circuit's response to voltage step functions. Both the voltage signal, produced by a function generator, and the integrator circuit's response are recorded using an oscilloscope. For an input signal with a frequency of 1 Hz, the integrator smooths the signal, but still retains noticeable features of the original signal. As the frequency of the input signal increases, the amplitude of the output signal consistently decreases until the signal essentially becomes flat.

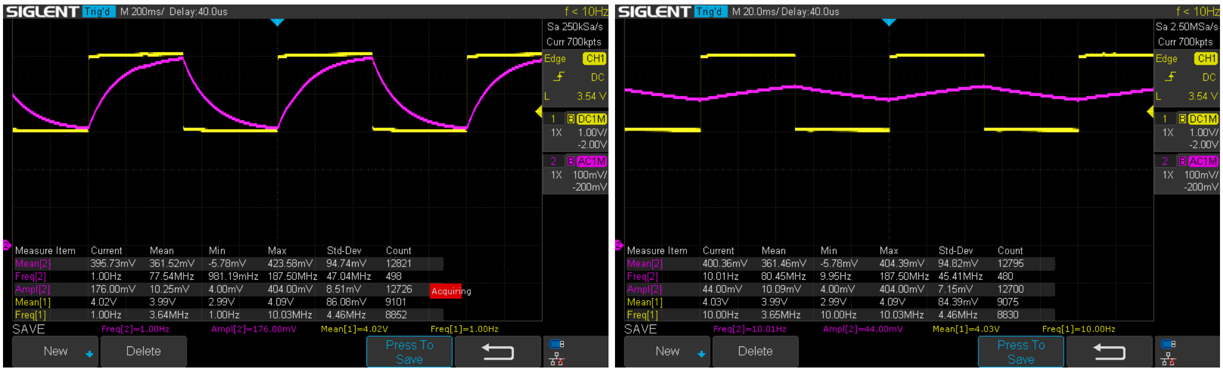

Measure Item	Current	Mean	Min	Max	Std-Dev	Count
Mean[2]	395.73mV	361.52mV	-5.78mV	423.58mV	94.74mV	12821
Freq[2]	1.00Hz	77.54MHz	981.19mHz	187.50MHz	47.04MHz	498
Ampl[2]	176.00mV	10.25mV	4.00mV	404.00mV	8.51mV	12726
Mean[1]	4.02V	3.99V	2.99V	4.09V	86.08mV	9101
Freq[1]	1.00Hz	3.64MHz	1.00Hz	10.03MHz	4.46MHz	8852

Freq[2]=1.00Hz Ampl[2]=176.00mV Mean[1]=4.02V Freq[1]=1.00Hz

Measure Item	Current	Mean	Min	Max	Std-Dev	Count
Mean[2]	400.36mV	361.46mV	-5.78mV	404.39mV	94.82mV	12795
Freq[2]	10.01Hz	80.45MHz	9.95Hz	187.50MHz	45.41MHz	480
Ampl[2]	44.00mV	10.09mV	4.00mV	404.00mV	7.15mV	12700
Mean[1]	4.03V	3.99V	2.99V	4.09V	84.39mV	9075
Freq[1]	10.00Hz	3.65MHz	10.00Hz	10.03MHz	4.46MHz	8830

Freq[2]=10.01Hz Ampl[2]=44.00mV Mean[1]=4.03V Freq[1]=10.00Hz

(a) Frequency of 1 Hz.

(b) Frequency of 10 Hz.

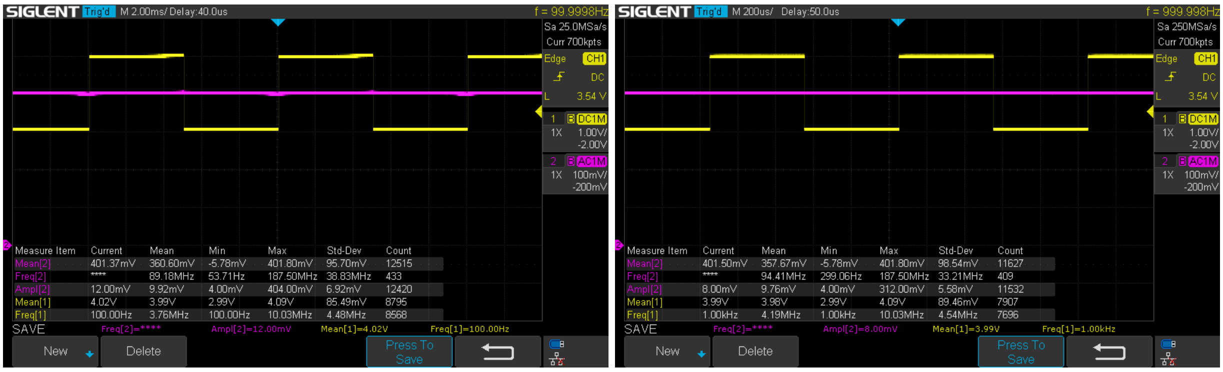

Measure Item	Current	Mean	Min	Max	Std-Dev	Count
Mean[2]	401.37mV	360.60mV	-5.78mV	401.80mV	95.70mV	12515
Freq[2]	****	89.18MHz	53.71Hz	187.50MHz	38.83MHz	433
Ampl[2]	12.00mV	9.92mV	4.00mV	404.00mV	6.92mV	12420
Mean[1]	4.02V	3.99V	2.99V	4.09V	85.49mV	8795
Freq[1]	100.00Hz	3.76MHz	100.00Hz	10.03MHz	4.48MHz	8568

Freq[2]=**** Ampl[2]=12.00mV Mean[1]=4.02V Freq[1]=100.00Hz

Measure Item	Current	Mean	Min	Max	Std-Dev	Count
Mean[2]	401.50mV	357.67mV	-5.78mV	401.80mV	98.54mV	11627
Freq[2]	****	94.41MHz	299.06Hz	187.50MHz	33.21MHz	409
Ampl[2]	8.00mV	9.76mV	4.00mV	312.00mV	5.58mV	11532
Mean[1]	3.99V	3.98V	2.99V	4.09V	89.46mV	7907
Freq[1]	1.00kHz	4.19MHz	1.00kHz	10.03MHz	4.54MHz	7696

Freq[2]=**** Ampl[2]=8.00mV Mean[1]=3.99V Freq[1]=1.00kHz

(c) Frequency of 100 Hz.

(d) Frequency of 1 kHz.

Figure 50: Input voltage (yellow), generated using a function generator, and output voltage of the RC integrator (pink) measured using an oscilloscope. It can be seen that the signal is smoothed, this smoothing process is more pronounced the higher the input frequency of the voltage signal into the RC integrator is.

C.6. Ethylene flow and Reynolds number

Here, the considerations about the C_2H_4 flow trough the capillary are expanded. In particular, the nature of the flow by looking at the Reynolds number is considered.

The Reynolds number is a dimensionless quantity and is a measure of the nature of the flow of a fluid. It is given by the ratio of inertial forces to viscous forces (Roedel and Wagner, 2017),

$$\mathrm{Re} = \frac{uL}{\nu} = \frac{\rho u L}{\eta}, \tag{144}$$

where u is the velocity of the fluid, ρ the density, η the dynamic viscosity and L the length scale of the considered system. The following regimes are defined (Wißdorf et al., 2016):

- laminar flow: $\mathrm{Re} < 2000$
- transition regime: $2000 < \mathrm{Re} < 4000$
- turbulent flow: $\mathrm{Re} > 4000$

In the case of a capillary, L is given by the radius of the capillary r. Here we look at the flow of a compressible gas, which means that the density of the gas changes with pressure. As the pressure changes inside the capillary, the density of the gas also changes inside the capillary. The velocity of the gas is determined by dividing the volume flow f by the cross-section of the capillary A. As only the volume flow at the end of the capillary can be measured, also the pressure at the end of the capillary is used to calculated the Reynolds number at the end of the capillary,

$$\rho_{\text{end}} = \frac{m}{V} = \frac{p_{\text{end}} M_{\text{mol}}}{RT} \tag{145}$$

$$u_{\text{end}} = \frac{f}{A} = \frac{f}{\pi r^2} \tag{146}$$

$$\Rightarrow \mathrm{Re}_{\text{end}} = \frac{p_{\text{end}} M_{\text{mol}} f r}{RT\pi r^2 \eta} \approx 166, \tag{147}$$

when inserting the following values, $M_{\text{mol}} = 25.08\,\mathrm{g/mol}$, $p_{\text{end}} = p_0 \approx 1000 \times 10^2\,\mathrm{Pa}$, $f = 0.4\,\frac{\mathrm{mL}}{\mathrm{s}}$ (see the flow calibration measurements in Fig. 15), $r = 0.075\,\mathrm{mm}$, $\eta = 10.28\,\mathrm{Pa\,s}$ and $T = 300\,\mathrm{K}$. The calculated Reynolds number is not only valid for the end of the capillary, but throughout the capillary. Due to continuity the following equation holds true,

$$f_1 \cdot p_1 = f_2 \cdot p_2. \tag{148}$$

Calculating the Reynolds number from this we arrive at,

$$\mathrm{Re}_2 = \frac{p_2 M_{\text{mol}} f_2 r}{RT\pi r^2 \eta} = \frac{p_2 M_{\text{mol}} \frac{p_1}{p_2} f_1 r}{RT\pi r^2 \eta} = \frac{p_1 M_{\text{mol}} f_1 r}{RT\pi r^2 \eta} = \mathrm{Re}_1 \tag{149}$$

It is assumed that the viscosity η is independent of pressure. This assumption is reasonable, since the assumption of an ideal gas and thus a pressure dependency of viscosity, only breaks down for high pressures, not reached in our CL monitor setup. For high pressure regimes η even increases with p, and therefore the Reynolds number would decrease. The flow is therefore considered to be laminar.

C.7. Additionally used instruments

Here, the other instruments used in this thesis are listed:

POM O_3 monitor 2B Technologies
https://www.twobtech.com/docs/brochures/model_306.pdf

little-RAVEN CO_2/SO_2 sensor system
https://doi.org/10.1038/s41598-022-21935-5

Ozone Calibration Source Model 306 2B Technologies
https://www.twobtech.com/docs/brochures/model_306.pdf

SYCOS KT-O_3/SO_2 test gas generator ANYSCO
https://www.yumpu.com/de/document/read/1891132/tragbarer-ozon-prufg

Drone Matrice 300 RTK, DJI,
https://enterprise.dji.com/de/matrice-300/specs

D. Tools

Here is a list of tools used in this thesis:

- The data logging code (see Appendix C.3) was written in Python, making heavy use of code examples from the Adafruit Learning System for the different modules.
- The code to analyse the data was written in Python.
- Large Language Models (GPT) were used to write and comment part of the Code as well a proof-read parts of the thesis.

Acknowledgements

I wish to warmly thank my supervisor Professor Ulrich Platt for guiding me throughout my master thesis. The enlightening discussions during our group meetings, coupled with his extensive knowledge spanning various physics domains, provided invaluable insights and directions that shaped this work. His unwavering optimism and confidence in the project's success were crucial for this project.

I am deeply thankful to Nicole Bobrowski for sharing her expertise not only in atmospheric and plume chemistry but also in volcanology, especially concerning Etna. Her insights, suggestions, and fresh perspectives have been invaluable. Nicole's vast experience, especially during our field campaign at Etna, ensured we were always on the right path. Special thanks to her and Thorsten Hoffmann for managing the drone operations and handling the associated pressures.

Ellen Bräutigam deserves special mention for initiating the construction of the CL O_3 monitor and orienting me to the project. Her consistent guidance and in-depth feedback were instrumental in my progression.

I owe a great debt of gratitude to Ralph Kleinschek. His technical expertise, innovative solutions, and readiness to assist were crucial for the successful development of the monitor, especially during the development of the housing of the instrument.

I also want to thank Jonas Kuhn for helping during initial stages of this thesis. Be it theoretical challenges, scientific or technical hurdles, his inputs were consistently helpful.

Alexander Nies provided essential assistance in the preparation for the Etna campaign and engaging discussions about the theoretical backgrounds of this work. Simon Warnach and Jaro Heimann deserve thanks for their revisions and proofreading.

Lastly, heartfelt appreciation goes to Moritz Sturm, who was not only a stronghold of encouragement but also contributed with his proofreading and suggestions. I'd also like to extend my gratitude to Joshua Marks who also helped to improve this thesis with his proofreading.

Erklärung:

Ich versichere, dass ich diese Arbeit selbstständig verfasst habe und keine anderen als die angegebenen Quellen und Hilfsmittel benutzt habe.

M. Rütt

Heidelberg, den 01.12.2023 ....